

IMPROVED CONTRAST IN RADIATION THERAPY IMAGING USING
LOW-Z TARGETS AND AMORPHOUS SILICON PORTAL IMAGERS

by

Elizabeth J. Orton

Submitted in partial fulfillment of the requirements
for the degree of Master of Science

at

Dalhousie University
Halifax, Nova Scotia
August 2008

© Copyright by Elizabeth J. Orton, 2008



Library and
Archives Canada

Bibliothèque et
Archives Canada

Published Heritage
Branch

Direction du
Patrimoine de l'édition

395 Wellington Street
Ottawa ON K1A 0N4
Canada

395, rue Wellington
Ottawa ON K1A 0N4
Canada

Your file Votre référence

ISBN: 978-0-494-44013-1

Our file Notre référence

ISBN: 978-0-494-44013-1

NOTICE:

The author has granted a non-exclusive license allowing Library and Archives Canada to reproduce, publish, archive, preserve, conserve, communicate to the public by telecommunication or on the Internet, loan, distribute and sell theses worldwide, for commercial or non-commercial purposes, in microform, paper, electronic and/or any other formats.

The author retains copyright ownership and moral rights in this thesis. Neither the thesis nor substantial extracts from it may be printed or otherwise reproduced without the author's permission.

AVIS:

L'auteur a accordé une licence non exclusive permettant à la Bibliothèque et Archives Canada de reproduire, publier, archiver, sauvegarder, conserver, transmettre au public par télécommunication ou par l'Internet, prêter, distribuer et vendre des thèses partout dans le monde, à des fins commerciales ou autres, sur support microforme, papier, électronique et/ou autres formats.

L'auteur conserve la propriété du droit d'auteur et des droits moraux qui protègent cette thèse. Ni la thèse ni des extraits substantiels de celle-ci ne doivent être imprimés ou autrement reproduits sans son autorisation.

In compliance with the Canadian Privacy Act some supporting forms may have been removed from this thesis.

Conformément à la loi canadienne sur la protection de la vie privée, quelques formulaires secondaires ont été enlevés de cette thèse.

While these forms may be included in the document page count, their removal does not represent any loss of content from the thesis.

Bien que ces formulaires aient inclus dans la pagination, il n'y aura aucun contenu manquant.

DALHOUSIE UNIVERSITY

To comply with the Canadian Privacy Act the National Library of Canada has requested that the following pages be removed from this copy of the thesis:

Preliminary Pages

Examiners Signature Page (pii)

Dalhousie Library Copyright Agreement (piii)

Appendices

Copyright Releases (if applicable)

TABLE OF CONTENTS

List of Tables.....	ix
List of Figures.....	x
Abstract	xiii
List Of Abbreviations Used.....	xiv
Acknowledgements.....	xvi
CHAPTER 1 Introduction.....	1
1.1 Megavoltage Imaging Applications.....	2
1.2 Megavoltage Image Quality	4
1.3 Candidate Target Materials	7
1.4 X-Ray Detection Systems.....	8
1.4.1 Screen Thickness	10
1.5 Previous Imaging with Low Atomic Number (Z) Targets.....	12
1.6 Factors Shown To Affect Energy Spectrum and Contrast.....	12
1.6.1 Target Thickness.....	12
1.6.2 Electron Energy.....	13
1.6.3 Scatter and Attenuation	13
1.7 Research Goals.....	15
CHAPTER 2 Radiological Physics	16
2.1 Charged Particle Interactions.....	16
2.1.1 Soft Collisions.....	17
2.1.2 Hard Collisions	18

2.1.2.1	Atomic Relaxation.....	18
2.1.3	Coulomb-force Interactions with the External Nuclear Field	19
2.1.4	In-flight Annihilation.....	19
2.1.5	Mass Stopping Power.....	20
2.2	Photon Production.....	22
2.3	Photon Interactions.....	23
2.3.1	Photoelectric Effect.....	24
2.3.2	Compton Interactions	27
2.3.3	Pair Production	30
2.3.4	Triplet Production.....	31
2.4	Photon Beam Measurements and Characteristics.....	32
2.5	Radiographical Imaging	35
2.6	Monte Carlo Radiation Transport.....	36
2.6.1	Probability Distributions and Random Sampling.....	36
2.6.2	EGSnrc.....	37
CHAPTER 3	Materials and Methods	39
3.1	6 MV and Experimental Low-Z Beams	39
3.1.1	Clinical Linear Accelerators.....	39
3.1.2	Experimental Low-Z Target Beam.....	42
3.1.3	Low-Z Target Position	43
3.1.4	Linac Head Modeling in Beamnrc	43
3.1.5	Component Modules	44
3.1.6	Source Parameters.....	44
3.1.7	Parameters for Increasing Efficiency.....	44

3.1.8	PEGS4	47
3.1.9	Phase Spaces.....	48
3.1.10	6 MV Beam Model	48
3.1.11	Experimental Beam Models.....	50
3.1.12	BEAMdp.....	51
3.1.13	Egswin.....	53
3.2	6 MV Beam Validation	55
3.2.1	Dose to Water with Ion Chamber Measurements.....	55
3.2.2	Dose to Water with Dosxyznrc.....	57
3.2.3	Phase Space Recycling.....	57
3.2.4	Geometry and Scoring Dose	58
3.2.5	Analysis of Scored Dose	58
3.2.6	MC Dose to Water.....	58
3.3	aS500 Detector Model Validation	59
3.3.1	aS500 Detector	59
3.3.2	6 MV Open Field Imaging	59
3.3.3	Detector Calibration	60
3.3.4	Solid Water.....	61
3.3.5	Film Measurements	61
3.3.6	aS500 Model.....	62
3.3.7	Latent Phase Space Variance	63
3.3.8	Validation.....	64
3.4	Quantifying and Validating Contrast.....	64
3.4.1	Simple 6 MV Contrast Evaluation.....	64

3.4.2	QC3 MV Imaging Phantom	64
3.4.3	QC3 Contrast Model in DOSXYZnrc	66
3.4.4	Effect of Field Size on Contrast.....	67
3.5	The Effect of Further Image System Alterations on Contrast	68
3.5.1	Incident Electron Energy	68
3.5.2	Copper Buildup Layer of Detector	68
3.5.3	Target Atomic Number.....	68
3.6	The Effect of Separation on Contrast.....	68
CHAPTER 4	Results and Discussion	70
4.1	6 MV and Experimental Low-Z Beams	70
4.2	6 MV Beam Validation	72
4.3	aS500 Detector Model Validation	74
4.4	Quantifying and Validating Contrast.....	77
4.4.1	Simple 6 MV Contrast Evaluation.....	77
4.4.2	Effect of Field Size on Contrast.....	78
4.4.3	6 MV and 6 MeV/Al Contrast Validation	79
4.5	The Effect of Further Image System Alterations on Contrast	81
4.6	The Effect of Separation on Contrast.....	82
CHAPTER 5	Conclusion	85
5.1	Monte Carlo Modeling	85
5.2	Contrast in Low-Z-Target MV Imaging: Summary of Results.....	85
5.3	Future Work: Further Optimizations.....	86
5.3.1	Screen thickness	86
5.3.2	Target Location	86

5.3.3 Necessary Level of Contrast	86
5.3.4 Imaging Dose.....	87
5.3.5 Cone Beam CT	87
5.4 Application.....	87
Bibliography	88
Appendix A Component Modules for Linac Modeling.....	91
Appendix B MATLAB Code for Reading and Adding 3ddose Files	92
Appendix C PVC PEGS Input File.....	95

List of Tables

Table 1.1 Summary of important properties for various target materials. Data from (Attix 2004) and (Emsley 1995).....	8
Table 2.1 Photon interactions important in radiological physics and their corresponding important and dominant energy ranges.....	23
Table 2.2 Effective atomic number and electron density for bone and tissue. Data from (Johns and Cunningham 1983)	35
Table 2.3 Comparison of the ratio of attenuation in bone versus tissue for both photoelectric and Compton interactions.	36
Table 3.1 Target thickness and composition along with the incident electron energy for all beams modeled by Monte Carlo (MC). The first two beams were also produced experimentally to compare with their MC models.	53

List of Figures

Figure 1.1 Comparison of kV (a) and MV (b) image quality with portal images from a head and neck patient. The dark dots in the MV image are made by a graticule used to aid alignment of patient anatomy.	5
Figure 1.2 Ratio of the mass attenuation coefficient for bone versus muscle as a function of energy with the kV imaging energy range shaded and the spectrum from a 6 MV therapy beam superimposed.....	6
Figure 1.3 Diagram demonstrating direct versus indirect detection systems, and MV indirect detection using a buildup layer. Film based systems are shown alongside a-Si EPID systems and the physical function of each layer is labeled. Standard kV diagnostic systems use the indirect detection configuration with a reduced screen thickness compared to MV systems.....	9
Figure 1.4 The effect of object-to-detector distance on scatter reaching the detector. The scattered photon is detected at object-to-detector distance d_1 but not at d_2	14
Figure 2.1 Demonstration of the increase in cross sectional area of medium available for soft interactions ($b \gg a$) versus hard interactions ($b \approx a$). Assuming a uniform distribution of atoms in the medium, more atoms will reside in the outer ring than the inner rings, meaning more are available for soft interactions.	18
Figure 2.2 Relative contribution of photoelectric (τ), Compton (σ) and pair production (κ) to the total attenuation cross section as a function of photon energy and atomic number (Z) of the medium. Figure from (Attix 2004).....	24
Figure 2.3 Photoelectric interaction of a photon $h\nu$ with an atomic electron. Energy and momentum are shown for all particles involved. Figure from (Attix 2004).....	25
Figure 2.4 Compton interaction of a photon $h\nu$ with electron, assumed unbound and stationary. Energy and momentum are shown for all particles involved. Figure from (Attix 2004).....	28
Figure 2.5 Pair production interaction of a photon $h\nu$ with the field of an atomic nucleus, producing an electron e^- and a positron, e^+ . Any photon energy, in addition to the rest mass energy of the charged pair created, goes into kinetic energy of charged particle, scattering them at angles $\neq 180^\circ$ relative to one another. Figure from (Attix 2004).	30
Figure 2.6 Photon beam characteristic curves. (a) PDD, (b) beam horns and (c) shoulder in radial profiles.	35
Figure 2.7 The basic chain of steps for radiation transport. The light blue boxes signify where stochastic events take place, requiring random probability distribution sampling in Monte Carlo simulation.	38

Figure 3.1 Diagram of the linac, contrast phantom and image detector. Part 1: major components of the linear accelerator head in both standard 6 MV mode (target above primary collimation, flattening filter aligned with beam in carousel) and in the experimental aluminum configuration (electron mode, aluminum target aligned with beam in carousel and electron filter in upper wedge mount). Part 2: QC3 phantom, surface located at approximately 99.1 cm SSD. Part 3: aS500 EPID with an expanded view of the main functional layers.	41
Figure 3.2 Low-Z targets. a) inserting low-Z custom target into linac carousel, b) the custom targets in their original and elevated style collars	42
Figure 3.3 The main inputs for the first step of 6 MV beam simulation.	49
Figure 3.4 Monte Carlo calculated electron fluence versus radial position for three planes corresponding to the downstream surface of the Be vacuum window, the improved target position (0.9 cm air gap), and the old target position (2.47 cm air gap). FWHM = full width half maximum.....	52
Figure 3.5 The egswin output for a Varian high energy linac model without (a) and with (b) particle history tracks. Photon tracks are shown in yellow, and electrons, in blue.	54
Figure 3.6 The initial components of the 6 MV (a) and 6 MeV/Al (b) linac heads, as output by EGS_windows. The target for the 6 MV beam is not shown, but is part of the first layer of primary collimation. The location of the incident electron beam is shown by the small yellow star at the entrance to the primary collimation.....	54
Figure 3.7 Location of the reference ion chamber relative to smallest field and principle in-plane and cross-plane axes, during water tank setup.....	56
Figure 3.8 AM Maintenance imaging parameters for 6 MV.	60
Figure 3.9 The QC3 MV imaging phantom with labels indicating contrast region composition.....	65
Figure 3.10 AM Maintenance imaging parameters for 6 MeV/Al.	66
Figure 3.11 Measured (a) and calculated (b) images of the QC3 contrast phantom using the aS500 detector. Images have been leveled at the mean of the 1.5 cm Al region, and window width selected to encompass the full range of both images.	67
Figure 3.12 Experimental setup for measuring contrast versus separation. Symmetric layers of Solid Water were added to increase separation, while the contrast layer was held at a constant distance from the source and from the detector.	69

Figure 4.1	Calculated photon spectra for a standard 6 MV therapy beam, 6 MeV/Al, 4 MeV/Al, 6 MeV/Be and 4 MeV/Be beams. Spectra are captured as they exit the accelerator head, for experimental beams this is below the 0.9 cm thick polystyrene electron filter. Each spectral distribution was normalized by its own area.	71
Figure 4.2	Calculated radial fluence profiles for the 6 MeV/Al and 6 MV beams, in air at 100 cm downstream of the electron source. The dotted lines mark -3.0 cm and -3.5 cm off axis, and the corresponding relative fluence, 0.92 and 0.89 respectively.	72
Figure 4.3	Depth dose and radial profiles for 5 x 5 cm ² and 20 x 20 cm ² fields for the 6 MV beam, comparing ion chamber (Measured) with Monte Carlo (Calculated). Radial profiles are taken at 10 cm depth.....	74
Figure 4.4	Relative dose versus radial distance along the in-plane axis (parallel to the linac waveguide), comparing calculated versus measured profiles for 6 MV images from the aS500 EPID at 130 cm SID for field sizes 5 x 5 cm ² to 15 x 15 cm ²	76
Figure 4.5	Absolute contrast versus contrast region for the QC3 phantom, comparing measured versus calculated results as a function of field size for the 6 MeV/Al beam. Solid lines denote measured contrast and circles, Monte Carlo calculated contrast.....	79
Figure 4.6	Absolute contrast versus contrast region for calculated and measured images with the standard 6 MV beam and 6 MeV/Al beam. Error bars show the standard error about the mean pixel value of each sampled region, propagated through the contrast calculation.	80
Figure 4.7	Absolute contrast versus contrast region, comparing QC3 calculated contrast on a standard aS500 EPID for 6 MeV and 4 MeV incident electron energies on 1.0 cm and 0.67 cm aluminum (blue) targets, respectively, and 6 MeV and 4 MeV incident electron energies on 1.5 cm and 1.0 cm beryllium (red) targets respectively. Contrast generated on a copper-less imager (No Cu) is shown, (denoted with circles).....	82
Figure 4.8	Bone to water contrast versus total separation, comparing measured 6 MV and 6 MeV/Al beams.....	83

Abstract

Prior to or during external beam radiation therapy, a megavoltage (MV) treatment beam may be used to image patient anatomy and to verify patient position. MV projection images, however, offer poor contrast, leading to possible uncertainty in patient positioning.

Low atomic number (Z) targets have been shown to alter the MV beam spectrum and to improve contrast in megavoltage images when using film-screen detection systems. Film-screen detection systems are no longer used in daily radiation therapy imaging, having been replaced by amorphous silicon electronic portal image detectors (a-Si EPID).

This research aims to quantify the effect of low- Z targets on MV image contrast using an amorphous silicon electronic portal image detector (a-Si EPID) through both experimental measurement and Monte Carlo (MC) simulation. Experimental beams were produced with a clinical linear accelerator operated in the 6 MeV electron mode with a 1.0 cm-thick aluminum ($Z = 13$) target, (6MeV/Al) and contrast quantified using a standard MV imaging phantom. A MC model of the full imaging system was developed, including beam generation, a contrast phantom and the a-Si detector. The model is shown to accurately reproduce contrast measurements to within 2.5% for both the standard 6 MV therapy beam and the 6 MeV/Al beam. Using the 6 MeV/Al beam instead of the 6 MV beam, imaging contrast increases by a factor of 1.57 to 2.81. The MC model was then extended to predict the effect on contrast of decreasing incident electron energy to 4 MeV and of removing the copper build-up layer in the detector. Both of these changes produced further increases in image contrast. Further decreasing the target Z to beryllium (Be, $Z = 4$) showed slight improvement over Al at 4 MeV and 6 MeV. Experimentally, the contrast advantage of 6 MeV/Al over 6 MV was found to decrease with increasing separation, but at head and neck separations of approximately 15 cm of water, a factor increase in contrast of 1.7 remains.

This study thus presents rationale for an improved method of beam-generation for MV imaging in radiation therapy using an a-Si EPID. The approach should be readily applicable to either planar or cone-beam imaging for image-guided radiation therapy (IGRT) techniques.

List Of Abbreviations Used

AEIT	approximate efficiency improving technique
Al	aluminum
a-Si	amorphous silicon
Be	beryllium
C	carbon
CAX	central axis
CBCT	cone-beam computed tomography
CHT	condensed history technique
CM	component module
CNR	contrast to noise ratio
Cu	copper
DBS	directional bremsstrahlung splitting
DGRT	dose guided radiation therapy
DNA	deoxyribonucleic acid
EGS	Electron Gamma Shower
EPIDs	electronic portal imaging devices
FWHM	full width half maximum
Gd ₂ O ₂ S: Tb	gadolinium oxysulfide doped with terbium
IGRT	image guided radiation therapy
IMRT	intensity modulated radiation therapy
IRS	Ionizing Radiation Standards
kV	kilovoltage
LUT	look-up-table
MC	Monte Carlo
MU	monitor units
MV	megavoltage
NRC	National Research Council
Pb	lead

PDD	percent depth dose
PEGS	Preprocessor for EGS
PVC	polyvinyl chloride
QA	quality assurance
RR	russian roulette
SBS	selective bremsstrahlung splitting
SID	source-to-imager distance
SLAC	Stanford Linear Accelerator Center
SSD	source-to-surface distance
UBS	uniform bremsstrahlung splitting
VRT	variance reduction technique
W	tungsten
Z	atomic number

Acknowledgements

I would like to thank my supervisor, Dr. James Robar for all of the opportunities he has encouraged me to experience over the last two years, most were difficult but worth the effort at the end. I know I still have a long way to go to catch you up but you set a great level for me to aim at.

Thank you to all of the medical physics staff at the Nova Scotia Cancer Center for guidance, technical expertise, and distraction when necessary – thanks to my running buddy Kiran for helping me burn off steam and Dr. Cupido Daniels for helping me choose my next academic steps.

Finally, but definitely not least importantly, thank you to my parents and sisters, and friends far away, for putting up with my calls and keeping me in touch with the outside world over the last few months.

Thank you to Roger for believing I can do it, keeping me company, feeding me and telling me not to stop... at least for a little while.

CHAPTER 1 Introduction

The 2008 report on Canadian Cancer Statistics indicates that, based on current incidence rates, almost 40% of the Canadian female population and 45% of the Canadian male population can expect to develop some type of cancer within their lifetime. Both incidence and mortality rates in Atlantic Canada are higher than the national average (Marrett, Dryer et al. 2008). The most common methods for cancer treatment are surgery, chemotherapy, hormonal therapy and radiation therapy (Saint-Jacques, Dewar et al. 2006). More than 50% of cancer patients in Nova Scotia receive radiation therapy as some part of their treatment plan (Saint-Jacques, Dewar et al. 2006).

External beam radiation therapy employs high energy charged particles and x-rays generated by clinical linear accelerators (linacs). The practical method for generating high energy x-ray beams is by allowing an accelerated electron beam to strike a metallic target. Collimation is used downstream to define the aperture for treatment and a range of beam angles used to approach the treatment volume from multiple directions. The energy range used for photons in radiation therapy is 4 MeV to 20 MeV, providing sufficient quality to penetrate to deep seated disease (Johns and Cunningham 1983).

Radiation targets the deoxyribonucleic acid (DNA) of cells, producing breaks in the molecular chain. Coincident breaks in opposing strands of DNA can result in incorrect rejoining of chromosomes and chromosomal aberrations that prove lethal during subsequent mitosis, induce apoptosis (programmed cell death) or can themselves result in carcinogenesis in normal cells. Uncontrolled cell proliferation was the earliest concept linked to cancer cells, seen on a macroscopic scale as rapid tumor growth (Hall and Giaccia 2006). Malignant cells are undifferentiated, indicating that their repair pathways are less mature than those of normal cells. Although the DNA of normal cells is also damaged by radiation, if sufficient time is allowed, normal cells can fix DNA damage and recover at a higher fraction than cancerous cells. Where possible, radiation delivery is designed according to the principles above to selectively target cancerous cells: the total radiation dose prescribed to the tumor is divided up and delivered in multiple fractions, usually daily or bi-daily, over the course of 5 to 7 weeks which allows recovery time for normal tissues (Hall and Giaccia 2006).

The primary aim of radiation therapy is to deliver adequate dose to diseased tissue, while minimizing peripheral dose to normal structures. To achieve this, a conformal treatment plan is the first requirement, and the second is the ability to correctly align and verify the anatomy of the patient, relative to the radiation delivered at treatment time.

Active research in conformal planning has produced techniques such as intensity modulated radiation therapy (IMRT) (Ling, Leibel et al. 2003), where a pattern of small apertures is used at each beam orientation, delivering a modulated fluence, such that the summed dose distribution can conform highly to even concave structures. Plans generated by IMRT have the ability to not only conform high dose to tumor volumes but also to aid in reducing dose to particularly sensitive surrounding tissue, dubbed organs at risk. However, in the event of geographic miss, IMRT can actually be more detrimental than less conformal methods due to high dose gradients.

In addition to the growing importance of correct alignment, the shape and size of internal anatomy can be affected over the course of fractionated treatment by factors such as tumor shrinkage, weight loss and edema. These concerns highlight the need for correct visualization of the anatomy prior to and during treatment. Image guided radiation therapy (IGRT) involves tracking these changes and triggering plan adaptations in the event of compromising discrepancies between critical structure locations at planning versus delivery (Morin, Gillis et al. 2006). The next aim in radiation therapy is dose guided radiation therapy (DGRT): the ability to calculate the cumulative dose actually delivered to each structure using imaging prior to or during therapy and compare to the planned dose, with the ability to adjust the treatment plan to compensate for change (Morin, Gillis et al. 2006). Dose is defined as the energy absorbed by the medium per unit mass and is expressed in gray (Gy) where $1 \text{ J/kg} = 1 \text{ Gy}$.

1.1 Megavoltage Imaging Applications

Acquiring megavoltage (MV) portal images with the therapy beam has been the standard method for checking alignment of internal patient anatomy with its location in planning images. Simply using two orthogonal projection images can check position in three dimensions; however, projection image quality suffers from superposition of all over and underlying anatomy onto the plane of interest, the result of capturing a two dimensional

transmission image of a three dimensional object. In response to this, multiple manufacturers have introduced cone-beam computed tomography (CBCT). MV CBCT uses the portal imaging system mounted on the linac to acquire multiple projection images throughout a rotation about the patient and then uses a back-projection algorithm to reconstruct individual planes making up the full three dimensional volume (Pouliot, Bani-Hashemi et al. 2005). Morin *et al* have investigated the use of MV CBCT for patient alignment and have highlighted some of its other potential usages. They report that MV CBCT produces sufficient image contrast to not only identify bony anatomy but soft-tissue structures like the prostate as well (Morin, Gillis et al. 2006). In kilovoltage (kV) CT images, high atomic number (Z) objects, such as prosthesis, cause streaking artifacts where accentuated photoelectric absorption in these objects blocks out information from all other structures along ray lines intersecting the high Z object. This can make contouring the tumor volume from kV CT images difficult, for example in cases such as prostate patients with hip replacements. Aubin *et al* have shown that MV CBCT, which relies on the less Z-dependent Compton interaction to produce image contrast, can eliminate the artifact and provide sufficient contrast for contouring (Aubin, Morin et al. 2006). Another potential usage for MV CBCT is dose reconstruction for DGRT. By imaging during therapy, using the treatment beam, the transmission images capture information about the actual dose distribution delivered. If enough beam angles are used for reconstruction, then the three-dimensional dose distribution can be recovered. This requires finding the electron density and removing the cupping effect caused by additional image attenuation through the centre of the body (Morin, Gillis et al. 2006). In CBCT, MV photons result in lower noise than kV photons, due to the direction of scatter being more forward directed at higher energies. The scatter to primary ratio in kV CBCT is about 4 times greater than MV CBCT (Morin, Gillis et al. 2006). Commercially, the ability to use the therapy beam for imaging provides a fully integrated simple system which is both inexpensive and efficient, requiring only the addition of a detector panel mounted below the patient. The kV commercial solution to this problem is an on-board kV imaging system oriented 90 degrees to the treatment beam (Walter, Boda-Heggemann et al. 2007). While this improves image quality, it comes with the

associated maintenance and quality assurance (QA) costs of an additional system and the additional challenge of aligning the imaging and the treatment isocentres.

For all of the reasons listed above, improvement of MV systems continues to be investigated as a viable alternative to on-board kV imaging. Previous studies have addressed the problem of MV image contrast and dose by altering the linac target to produce more low energy photons. The following sections outline their findings.

For radiation therapy applications, although the dose per MV image is high compared to kV, the dose per image relative to treatment itself is low and the benefits in alignment relative to no imaging are worth the small amount of additional dose. Patient dose for a kV projection image are on the order of 1 mGy, while for MV the same image requires approximately 100 mGy (Walter, Boda-Heggemann et al. 2007). A typical dose per fraction in radiation therapy is 2 Gy to the tumor volume, which in IMRT plans can result in dose delivered to peripheral structures that is on the order of 5% to 10%, or 10 cGy to 20 cGy (Ling, Leibel et al. 2003). The major advantage of MV imaging is that recording during treatment delivery is essentially ‘free’ in terms of patient dose.

1.2 Megavoltage Image Quality

MV image quality is notoriously poor compared to kilovoltage imaging which often translates into uncertainty when MV images are used for patient alignment.

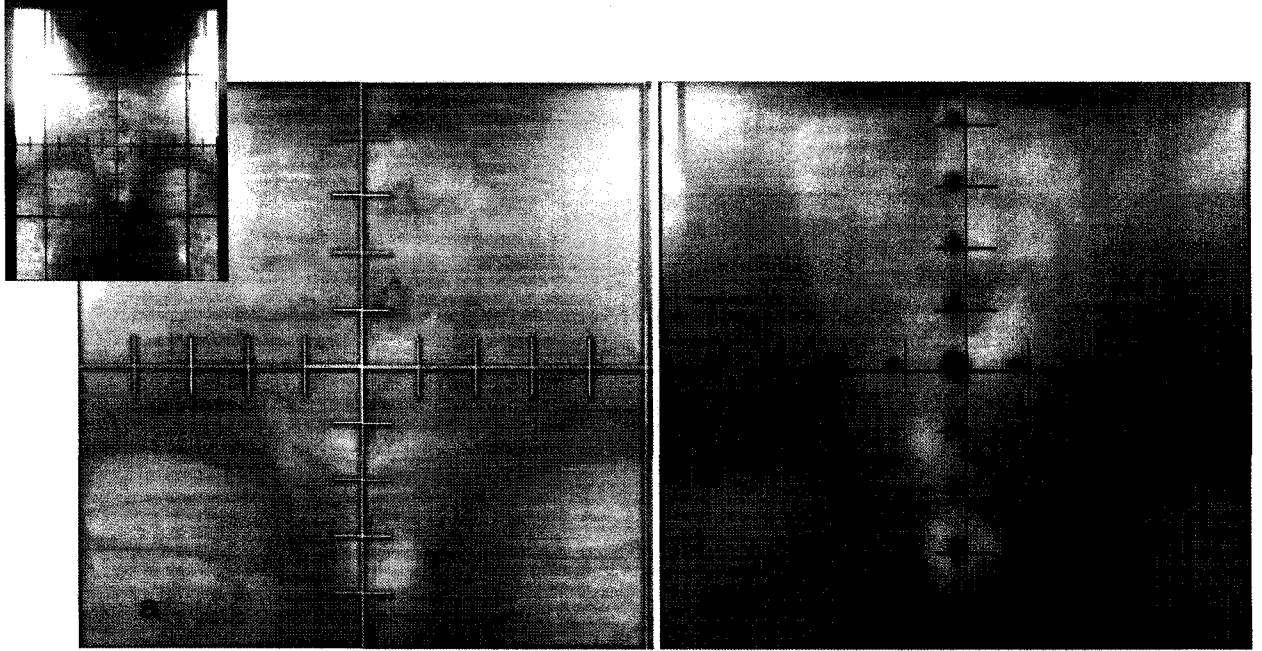


Figure 1.1 Comparison of kV (a) and MV (b) image quality with portal images from a head and neck patient. The dark dots in the MV image are made by a graticule used to aid alignment of patient anatomy.

From a diagnostic imaging standpoint, MV beams are significantly inferior to kV, providing far less contrast (figure 1.1) and for the same fluence at the detector plane, deliver 10-100 times the dose by using MV photons (Walter, Boda-Heggemann et al. 2007). This is compounded by the problem that MV detection systems provide lower detection efficiency than kV systems. Since imaging involves irradiation of a large area, containing healthy structures, it is advantageous to deliver as low a dose per image as possible.

Image contrast is defined as the ratio of the difference in mean signal between two regions of the image versus the mean signal from one of the regions, chosen to be the reference region:

$$Contrast = \frac{(\bar{p}_i - \bar{p}_{ref})}{\bar{p}_{ref}} \quad \text{Eq.1.1}$$

Both MV and diagnostic beams record transmission images; where the detector captures the fraction of the incident signal that is transmitted through the sample object and differences in attenuation between structures in the object cause contrast in the image.

Figure 1.2 shows the ratio of the mass attenuation coefficient of bone versus that of muscle, as a function of photon energy. This ratio peaks at a value of 3.8 between 10 and 20 keV and decreases to approximately unity by 200 keV. The diagnostic kV energy range is superimposed (shaded region) along with the spectrum from a 6 MV therapy beam and shows that while a significant portion of the kV range overlaps with non-unity values of the mass attenuation ratio, the MV spectrum has hardly any photons in the range where differential attenuation between bone and muscle exists.

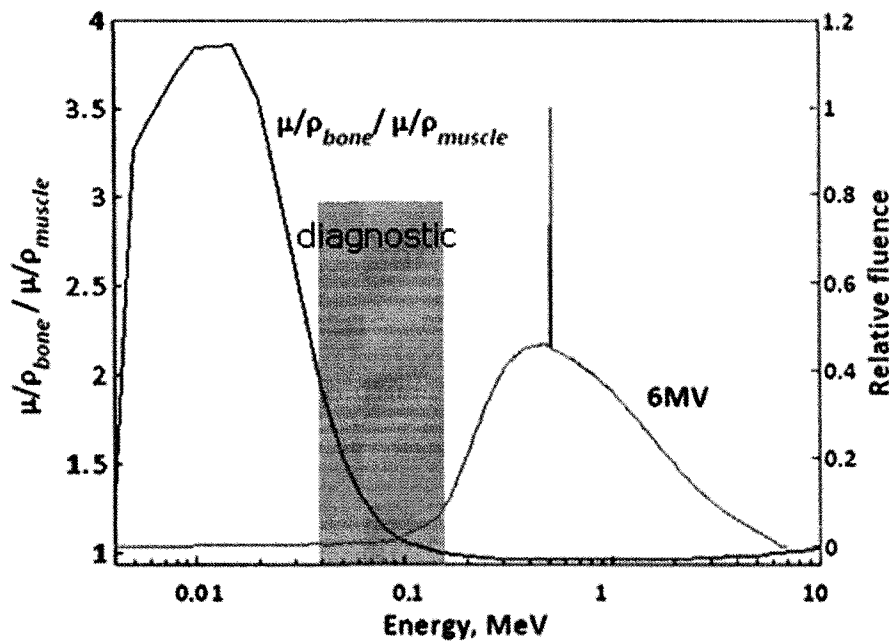


Figure 1.2 Ratio of the mass attenuation coefficient for bone versus muscle as a function of energy with the kV imaging energy range shaded and the spectrum from a 6 MV therapy beam superimposed.

kV x-ray sources generate their low energy spectra by only accelerating electrons to around 100 keV before striking the target. Linear accelerators use high power carrier waves fed into the cavities of a waveguide that accelerate electrons with a sequence of pulses. The electron energy produced by linear accelerators can be adjusted within a certain range by detuning cavities of the waveguide; however, the lower limit of this technique is a few MeV before the beam destabilizes (Karzmark, Nunan et al. 1993). An alternate method for gaining low energy photons is changing target material.

1.3 Candidate Target Materials

When an accelerated electron beam strikes a linac target, some of the incident electrons interact with the Coulombic field of a target atom's nucleus and are slowed down and redirected. The energy they lose is emitted as bremsstrahlung, or 'braking radiation' (Attix 2004). This is the primary method producing the linac photon beam.

Bremsstrahlung is created at all energies up to the incident electron energy; however, the target itself may act as a filter, preferentially absorbing some photon energies. MV therapy targets are generally thick disks of high atomic number materials, such as tungsten (W), lead (Pb), that are often combined with a copper (Cu) layer. The problem with using a standard therapy target for imaging is that while photons are produced at all energies up to the incident electron energy, the majority of low energy photons generated are absorbed in the target itself. This selective absorption results from the high photoelectric cross section for low energy photons in high-Z material (Attix 2004).

Photoelectric interaction cross section per atom is proportional to the fourth power of the atomic number, indicating that reducing target Z could significantly impact low energy absorption in the target (Attix 2004).

Other important target material properties to consider include: high melting point, good thermal conductivity, high threshold for neutron production, electron density and low cost. For the electron energy range associated with a linac, energy loss to radiation can be up to 95% (Johns and Cunningham 1983) and is proportional to the target's atomic number up to electron energies of 100 MeV.

Previous groups have investigated multiple low-Z materials for improved MV imaging, as well as for other applications where a low energy photon population is desired (Robar 2006). The spectra from beryllium (Be), aluminum (Al), carbon (C, graphite and diamond), and copper targets have all been evaluated and show significant low energy photon populations compared to therapy beams. Table 1.1 compares the values of important target properties for these low-Z materials and tungsten. Be has the lowest Z of the materials listed ($Z_{\text{Be}} = 4$) and one of the highest melting points of light metals but is a class 1 carcinogen and particularly toxic if inhaled as a dust during machining. Al has an atomic number of 13 and is of low cost, non toxic and a good thermal conductor, with a

melting point about half that of Be but, like Be, has a relatively low density. The advantages of C, in diamond form, are a relatively low Z and very high thermal conductivity. The rate of energy loss to bremsstrahlung is proportional to the product of the atomic number and electron density (Attix 2004).

Element	Atomic number, Z	Melting point, K	Thermal conductivity, W/mK	Cost	Z*Electron density, g/cm ³
W	74	3695	173	Medium	1.80×10^{25}
Al	13	933.5	235	Low	3.77×10^{24}
C (diamond)	6	3800	900–2320	High	1.81×10^{24}
Be	4	1560	190	Medium	1.07×10^{24}

Table 1.1 Summary of important properties for various target materials. Data from (Attix 2004) and (Emsley 1995)

Galbraith (1989) indicates that for thin targets, decreasing the atomic number increases the fractional yield of low energy x-rays, reasoning that reducing Z both decreases internal absorption of low energy photons and increases the relative contribution of electron-electron bremsstrahlung compared to electron-nuclear bremsstrahlung. Electron-electron bremsstrahlung has a similar shaped spectrum to electron-nuclear bremsstrahlung but a lower peak energy (Galbraith 1989). Flampouri *et al* (Flampouri, Evans et al. 2002) also show that as the target atomic number decreases, image contrast increases but that the effect is reduced by increased attenuating thickness of water (or patient). This group reported normalized efficiency versus target atomic number and indicated a local maximum at $Z = 13$; consequently Al is chosen as their target material for further investigation.

1.4 X-Ray Detection Systems

X-ray detection systems are generally based on indirect detection: for example, many use phosphor screens or scintillators to convert high energy x-rays into visible light, which is then detected by either photo-chemical reactions in a film emulsion or by energy-to-charge conversion in a photodiode array.

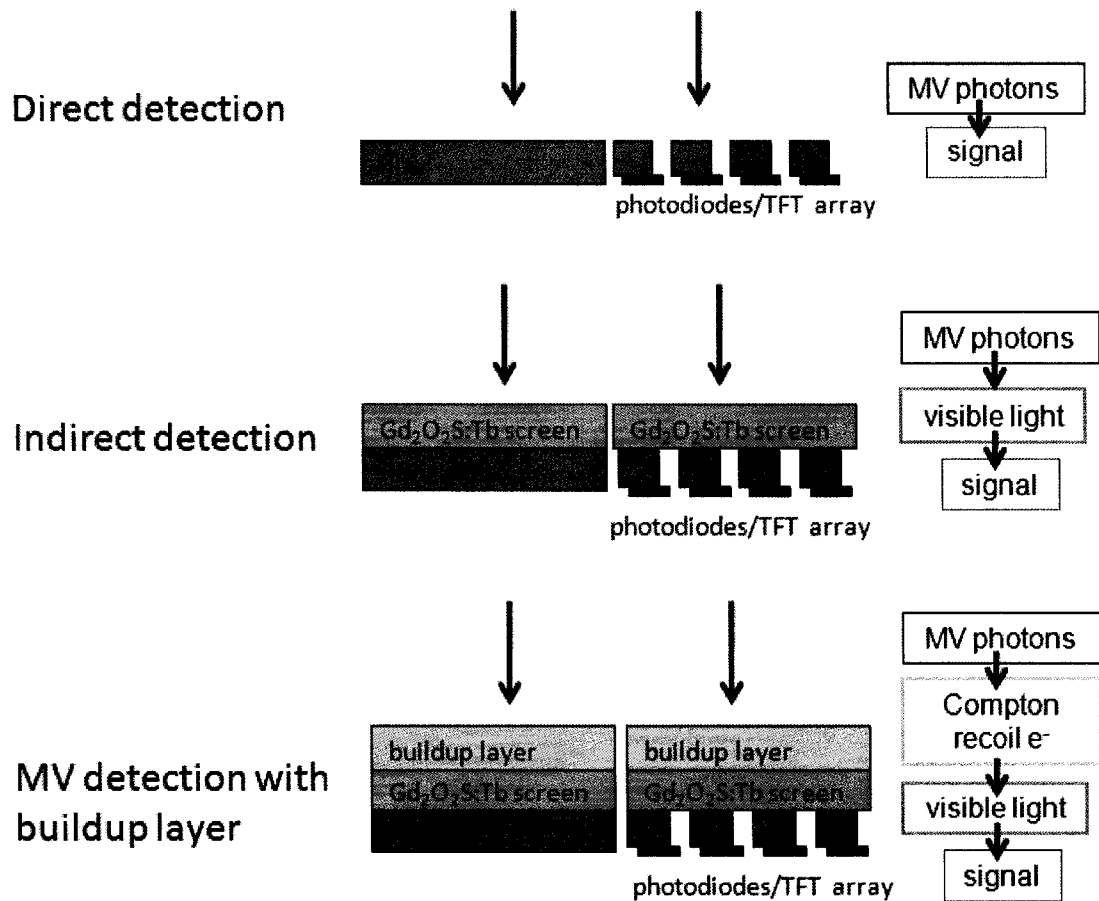


Figure 1.3 Diagram demonstrating direct versus indirect detection systems, and MV indirect detection using a buildup layer. Film based systems are shown alongside a-Si EPID systems and the physical function of each layer is labeled. Standard kV diagnostic systems use the indirect detection configuration with a reduced screen thickness compared to MV systems.

Screen materials typically have high Z to increase photon absorption which is particularly high for diagnostic energy (keV) photons, once again due to photoelectric absorption as described in section 1.2 for low energy bremsstrahlung in high Z targets. Higher attenuation cross sections for lower energy photons mean that diagnostic screens can be thin, while high energy (MV) photons require a thicker screen which is often preceded by a buildup layer of material to convert the incoming photon energy into Compton recoil electrons before it reach the screen. The buildup layer is a thin layer of metal which increases the detection efficiency of MV systems but will decrease contrast due to absorption of low energy photons and lateral scattering during Compton interactions in this layer. Gadolinium oxysulfide doped with terbium ($\text{Gd}_2\text{O}_2\text{S:Tb}$) is a popular screen

material due to high effective atomic number and high x-ray to light conversion efficiency (Flampouri, Evans et al. 2002).

Previously, the standard for MV imaging were radiotherapy verification systems: film-screen cassettes with thicker screens than those used for diagnostic imaging and a 1 - 2 mm metal buildup plate, usually made of Cu, on the upstream face of the screen (Flampouri, Evans et al. 2002). Today amorphous silicon (a-Si) electronic portal imaging devices (EPIDs) are the standard for high resolution imaging, having replaced film-screen systems for most daily applications in both diagnostic and MV imaging. The a-Si EPIDs still use phosphor screens (and buildup layers for MV imaging) but replace film with an array of amorphous silicon photodiodes on a glass substrate that allow the image to be read out electronically, coupling to the photodiodes via thin film transistors (TFTs).

The Varian aS500 MV a-Si EPID used in this work uses a copper buildup layer, a $\text{Gd}_2\text{O}_2\text{S}:\text{Tb}$ screen approximately 0.130 g/cm^2 thick and a 512×384 array of a-Si photodiodes with pitch $0.78 \times 0.78 \text{ mm}^2$ (Siebers, Kim et al. 2004). All further references to a-Si EPIDs should be assumed to be MV imagers.

Flampouri *et al* show the energy response of a radiotherapy verification system is on the order of 100 times less than a mammography film-screen system to 100 keV photons but that above 250 keV both systems exhibit a similar energy response (Flampouri, Evans et al. 2002). This indicates that at low energy the metal buildup layer impairs detection efficiency by fully absorbing a large fraction of the incident fluence. At higher energy, the buildup reduces the energy of photons penetrating to the high Z screen, increasing their chance of absorption. The advantage of the buildup layer in the verification system at high energy over the mammography system without buildup is not substantial, leading to similar energy response.

1.4.1 Screen Thickness

The screens used in the Varian aS500 amorphous silicon EPID and the Kodak Lanex Fine film-screen mammography system, used in previous studies, are both $\text{Gd}_2\text{O}_2\text{S}:\text{Tb}$. The thickness of the mammography screen is 0.034 g/cm^2 (Flampouri, Evans et al. 2002), while that of the aS500 screen is approximately 0.130 g/cm^2 (Siebers, Kim et al. 2004).

Galbraith (Galbraith 1989) compares the depth dose curves for mono-energetic low energy (0.1 MeV) versus high energy (2 MeV) x-ray beams in pure gadolinium (Gd). He shows that the low energy beam deposits more dose than the high energy beam at small detector thickness, but as thickness increases the low energy beam deposits progressively less dose while the high energy beam deposits dose uniformly throughout. Using the ratio of dose absorbed from low energy versus high energy beams as a function of gadolinium thickness, 110 – 130 times more energy is shown to be absorbed from the 0.1 MeV beam than the 2 MeV beam for Gd thicknesses up to 0.1 g/cm²; this advantage then drops rapidly as thickness increases. For 6 MeV electrons on a 3.2 g/cm² graphite target, an estimate of the ‘soft’ (low energy) fraction of the spectrum is multiplied by the ratio of dose required for high energy versus low energy x-rays to produce equal film optical density in an effort to estimate the low energy signal gain of using the low-Z target. Galbraith estimates this to be 20:1 without attenuation, 6:1 for 10 cm water attenuation and 1.6:1 for 20 cm water attenuation.

Ostapiak *et al* (Ostapiak, O'Brien et al. 1998) demonstrate selective low energy sensitivity in a Kodak Lanex Fine screen system combined with low-Z beams by plotting the Monte Carlo calculated product of low-Z target spectra and screen energy response as a function of energy. Screen energy response is the fraction of incident energy absorbed per particle by the screen. With 10 cm of water attenuation, Be, C and Al beams all show peak energy fluence times screen response at approximately 70 keV.

Flampouri *et al* (Flampouri, Evans et al. 2002) evaluated energy response curves for 0.034 g/cm², 0.150g/cm² and 0.450 g/cm² gadolinium oxysulfide screens. The ratio of the energy response at 70 keV to 1 MeV for 0.034 g/cm² was 1100, for 0.150g/cm² was 150 and for 0.450 g/cm² was 90. The ratio of response at 250 keV to 2 MeV for 0.34 g/cm² was 125, which supports the results of Galbraith. For 4.75 MeV electrons on Al, a 0.050 g/cm² thick gadolinium oxysulfide screen was calculated to give 3% better contrast for a 1.4 cm bone insert in 5 cm water compared to the thickest (0.450 g/cm²) screen. It is noted that the thinner the screen, the more dose required to take an image: a 0.050 g/cm² thick screen requires twice the dose of a 0.150g/cm² screen; however, the dose required using a low-Z target and thin film screen was still small compared to that required with the therapy beam and validation system, (0.2 cGy for low-Z beam with the

mammography film-screen detector versus 2 cGy for the therapy beam and verification system).

1.5 Previous Imaging with Low Atomic Number (Z) Targets

Many groups have quantified increases in MV image contrast used low-Z targets; however, they have all used film-screen detection systems. Galbraith (1989) used 6 MeV electrons on C and Be targets with a Kodak Ortho-M/ Lanex Fine film-screen detector, and reported a contrast increase of 1.04 to 1.25 relative to the standard 6MV therapy beam for a 10 cm-thick object. Tsechanski *et al* (1998) used 4 MeV electrons on thin Cu and Al targets and a Kodak Min-R film-screen mammography detector and indicated increased image sharpness and contrast. Ostapiak *et al* (1998) used 6 MeV electrons on C and Be targets and observed a contrast increase relative to the standard 6 MV therapy beam by a factor of 2, also with a Kodak Min-R E/Lanex Fine ($\text{Gd}_2\text{O}_2\text{S}$) film-screen mammography detector. Flampouri *et al* (2002), using 4.75 MeV electrons also on Cu and Al targets, report contrast increasing from 2% to 19% for the low-Z beams over the standard 6 MV beam. This group also employed a full Monte Carlo model of the imaging system to calculate contrast and found agreement within 2.5% of measured values.

1.6 Factors Shown To Affect Energy Spectrum and Contrast

1.6.1 Target Thickness

By comparing the results from previous studies, Galbraith (Galbraith 1989) shows that increasing target thickness will increase the fractional photon yield below 150 keV and reasons that this is due to the contribution of energy degraded electrons to low energy photon production. At incident electron energies of 4 MeV and 10 MeV, the effect of varying Cu target thickness was examined by Tsechanski *et al* (Tsechanski, Bielajew *et al*. 1998). In contrast to the observations by Galbraith, this group's spectra show hardening of the beam with increasing target thickness.

Potentially there exists an optimal thickness for the target at a given electron energy, where energy degraded electrons have produced photons down to the minimum energy

that can escape the target without being attenuated. Greater target thicknesses would then only serve to attenuate more of the low energy population.

Tsechanski *et al* (Tsechanski, Krutman et al. 2005) and Flampouri *et al* (Flampouri, Evans et al. 2002) chose their target thickness based on maximum total photon fluence. Tsechanski *et al* show maximum fluence is obtained at the lowest examined thickness for 4 MeV, (1.5mm) and a thickness of 4 mm for 10 MeV incident electrons. Flampouri *et al* (Flampouri, Evans et al. 2002) finds maximum efficiency with an Al target of thickness 0.6 cm with 4.75 MeV incident electrons, corresponding to approximately 60% of the electron continuous slowing down approximation (CSDA) range in Al.

1.6.2 Electron Energy

Galbraith (1989) reports an increase in the fractional yield of low energy x-rays with decreasing atomic number of the target but indicates that this gain was most significant for the lowest incident electron energy. Tsechanski *et al* (1998), on the other hand, indicate lowering incident electron energy does not significantly affect the fraction of low energy photons; however this group was using a fixed, non-optimized target thickness. Lowering the energy incident on a fixed thickness target by matching the incident energy and target thickness, it is hoped that an energy spectrum more appropriate for imaging can be produced.

1.6.3 Scatter and Attenuation

Mah *et al* (Mah, Galbraith et al. 1993) calculated primary and scattered photon spectra for 6 MeV electrons on a Be target transported through 20 cm of water. Their results show that the phantom attenuates a significant portion of the contrast-generating low energy primary photons and creates a low energy scatter population in the same energy range as was attenuated from the primary. They reason that this will increase the scatter to primary ratio detected in images and develop an anti-scatter grid for MV low-Z imaging.

In the object being imaged, scattered radiation, redirected by some small angle relative to the primary rays, can potentially reach the detector if insufficient object-to-detector distance is used. By increasing this distance, scattered radiation has a greater chance of falling outside the detection area, figure 1.4.

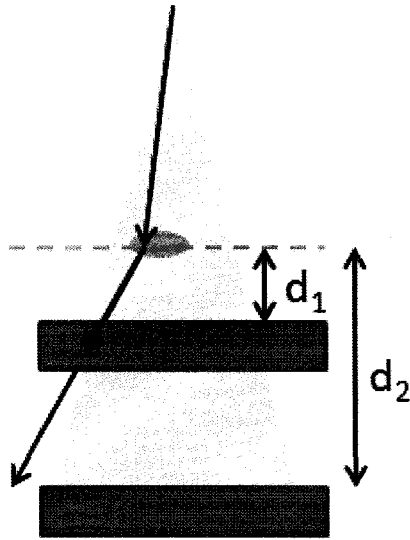


Figure 1.4 The effect of object-to-detector distance on scatter reaching the detector. The scattered photon is detected at object-to-detector distance d_1 but not at d_2 .

Ostapiak *et al* (Ostapiak, O'Brien et al. 1998) examine the effects of phantom-film distance and clearance behind the film plane on film contrast. They use Monte Carlo (MC) simulation to replicate their experimental setup and separate the contrast from the primary component of the beam from that of the total beam. Their Monte Carlo results show that contrast due to primary fluence does not change with phantom-film distances between 0 cm and 60 cm; this demonstrates the theoretical upper limit of the system without scatter. The Monte Carlo contrast from the total fluence showed contrast, at zero phantom-film distance, is approximately 1/3 of the primary contrast value and approaches primary contrast at a distance of 60 cm. The film results show the same trend as the total Monte Carlo fluence, but have values 5-10% lower. Increasing the clearance behind the film plane from 1 m to 2 m increased film contrast but this difference was not significant. These results indicate a phantom-film distance of 60 cm or greater will avoid most scatter to the detector.

Ostapiak *et al* (Ostapiak, O'Brien et al. 1998) also simulate the energy spectra from Be, C and Al targets before and after attenuation by 10 cm of water. They show that a significant photon population below 25 keV exists in the Be and C beams prior to but not after the water attenuation.

As a beam penetrates the medium, lower energy photons are preferentially attenuated, increased the mean energy of the beam, an effect called beam hardening (Johns and Cunningham 1983). Since lower energy photons produce significantly more contrast in biological tissue than at higher energies, increasing the thickness of the object being imaged reduces the low energy photon population, potentially decreasing contrast. The effect of increasing separation on image contrast has been investigated for therapy and low-Z beams by multiple groups using film-screen detectors (Galbraith 1989; Mah, Galbraith et al. 1993; Ostapiak, O'Brien et al. 1998). Decreased contrast is shown with increased separation for therapy and low-Z beams; but that low-Z contrast begins at a higher value and falls more quickly with both beams producing equal contrast at thickness of water around 15 cm.

1.7 Research Goals

In this research, the investigation of low-Z-target MV imaging is extended to address detection by currently-used a-Si detectors. The specific goals of this work are:

- i) Use Monte Carlo (MC) techniques, model the generation of standard 6 MV and experimental Al-target beams, and to validate these models;
- ii) To simulate the detection of these beams using a realistic MC model of the aS500 imaging panel and to validate this model;
- iii) To quantify and compare image contrast produced by both 6 MV therapy and experimental Al-target beams;
- iv) To determine, using the imaging system model validated in step (ii), the effect on contrast of decreasing electron energy, removing Cu detector buildup from the panel, and further lowering target Z; and
- v) To measure, for 6 MV and experimental Al beams, the effect of increasing separation on image contrast.

CHAPTER 2 Radiological Physics

All radiation interactions are stochastic processes: for a known set of initial conditions, the outcome of any individual event cannot be determined with certainty. However, if a group of interactions are observed, the probability of any potential outcome can be evaluated based on the statistics of the group. Although both charged and uncharged radiation interactions are stochastic on a single event basis, the way charged particles interact with the medium over a given range is distinct from that of uncharged radiation, causing different methods to be used when predicting interaction and energy transfer.

2.1 Charged Particle Interactions

Much of the following explanation of radiation interaction applies to all types of charged particles; however, for the purposes of this research, the charged particles we are most interested in are electrons. Electrons have relatively low mass in comparison to most other types of charged particle radiation, with the exception of positrons which have equal mass but occur much less often than electrons. The electron mass is approximately 2000 times smaller than that of protons, which results in two major differences in terms of interaction with the medium. Scattering is far more significant for electrons and results in tortuous paths through the medium. This makes measurements of the electron path length range very difficult. The maximum and minimum potential energy transfer per event is also much different for electrons versus heavy charged particles, governed by conservation of momentum.

The Coulomb electric force field of charged particle radiation causes it to interact almost continuously with the atoms of the surrounding medium that are both close to its path and more distant, and its energy is lost gradually in many small transfer events. Therefore, for charged particles, the location of an interaction is not predicted on a single event basis but instead, all interactions types are assumed to occur within an interval of the charged particle track and the amount of energy transferred via each type is estimated for that interval through their individual rates of energy transfer, or 'stopping powers'.

The types of charged particle interactions are governed by the relative size of the impact parameter, b , and the atomic radius, a . The impact parameter is defined as the distance of the influenced atom in the medium to the charged particle. There are three principle types of charged particle interactions:

1. Soft collisions occur for $b \gg a$
2. Hard collisions occur for $b \approx a$
3. Coulomb force interactions with the external nuclear field occur for $b \ll a$

2.1.1 Soft Collisions

In a soft collision, the charged particle's electric field distorts the field of atoms some distance away, transferring enough energy to excite or sometimes ionize the atoms. This is a distant interaction which can be influenced by the state of intermediate atoms of the medium. It has been found that atoms peripheral to the charged particle track become polarized by the passing electric charge which reduces the amount of energy transferred by soft collisions to more distant atoms. In practice, this effect is incorporated into calculation using a density effect correction factor. The energy transferred per soft collision is much less than that for hard collisions; however, the number of atoms that can experience soft collisions far exceeds those available for hard collisions (figure 2.1) resulting in about half of the total charged particle energy being lost to soft collisions (Attix 2004).

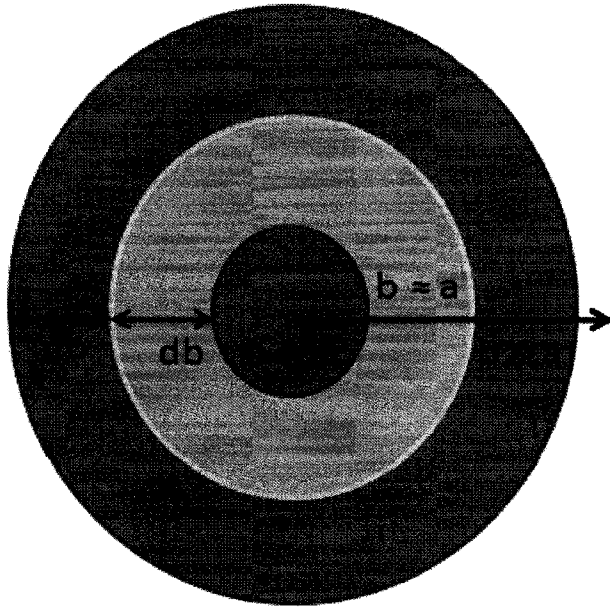


Figure 2.1 Demonstration of the increase in cross sectional area of medium available for soft interactions ($b \gg a$) versus hard interactions ($b \approx a$). Assuming a uniform distribution of atoms in the medium, more atoms will reside in the outer ring than the inner rings, meaning more are available for soft interactions.

2.1.2 Hard Collisions

Hard collisions occur when the charged particle interacts directly with an atomic electron, ejecting it from the atom by transferring enough energy to exceed the electrons binding energy. This electron is then called a delta ray, and often enough energy in excess of the binding energy has been transferred that the ejected electron is scattered along a track of its own, called a spur. Hard collisions transfer more energy per event than soft collisions, but happen less often, as previously demonstrated. The fraction of the total charged particle energy spent in hard collisions is about the same as in soft collisions (Attix 2004).

2.1.2.1 Atomic Relaxation

When an atom is ionized at one of its inner shells by a hard collision or photoelectric event (section 2.2.1), the resulting vacancy is normally filled by an electron donated by the next highest available shell. This occurs most often between the K and L shells. The atom now has excess energy equal to the difference in binding energy between the two shells and a hole in the next highest shell to fill. The excess energy can be dealt with in two ways: a 'characteristic' photon can be emitted with energy equal to the difference in

binding energy, or the atom can eject another of its electrons, termed an Auger electron, whose energy is equal to the difference in binding energies minus the ejecting electrons binding energy. Both these processes leave at least one vacancy in a shell higher than the original vacancy which must then be filled by replicating either one of the two processes, and the cycle repeated until the outer shell is reached and filled with conduction band electrons. In the end, the total binding energy of the electron originally ejected by the hard collision is turned into Auger electron kinetic energy plus the energy radiated as characteristic x-rays.

2.1.3 Coulomb-force Interactions with the External Nuclear Field

Charged particle Coulomb force interactions with the external nuclear field result in elastic scattering of the charged particle or in the charged particle being slowed and redirected by briefly orbiting the nucleus and giving up some energy to produce bremsstrahlung radiation. Bremsstrahlung is a photon produced by slowing a charged particle; it is the German word for 'braking radiation'. Nuclear elastic scattering accounts for the majority of electron scattering events and for the majority of Coulomb force interactions with the external nuclear field. The fraction of total charged particle energy radiated in bremsstrahlung events is inversely proportional to the squared mass of the particle, restricting the majority of bremsstrahlung production to electrons and positrons.

2.1.4 In-flight Annihilation

There is one other type of charged particle interaction, available only to positrons. When a positron has very little kinetic energy remaining (on the order of 10 eV) and encounters an electron, the two can experience in-flight annihilation, where their rest mass energy appears as two 511 keV photons directed at 180 degrees to one another (Johns and Cunningham 1983). If either of the charged particles had some kinetic energy remaining prior to annihilation, this energy will be divided between the emerging photons, not necessarily equally, and result in slight angular deviations from the direct 180 degree split. Energy released in annihilation is dealt with separately from bremsstrahlung and is not included in the mass radiative stopping power.

2.1.5 Mass Stopping Power

The constant interaction and gradual energy loss of charged particles traveling through the medium allow interactions and energy transfer to be modeled as a friction-like process where particles are continuously slowed down. Stopping power is defined as the rate of energy loss per unit path length for a given type of charged particle of kinetic energy T in a given medium Z , usually in units of MeV/cm. Stopping powers are typically divided by density and called mass stopping power, expressed in units of MeVcm²/g.

The total mass stopping power can be divided into two components that indicate the fate of the energy transferred to the medium: mass collisional and mass radiative stopping powers.

The mass collisional stopping power for electrons and positrons includes contributions from interactions where energy transferred is absorbed and results in direct excitation and ionization of the medium. For electrons and positrons, soft and hard collision terms are combined and can be expressed as (Attix 2004):

$$\left(\frac{dT}{\rho dx} \right)_c = k \left[\ln \left(\frac{\tau^2(\tau+2)}{2 \left(\frac{I}{m_o c^2} \right)^2} \right) + F^{+/-}(\tau) - \delta - 2C/Z \right] \quad \text{Eq. 2.1}$$

where:

$$k \equiv 0.1535 \frac{Zz^2}{A\beta}, \quad z \text{ being the charged particle number of elementary charges and } Z \text{ and } A$$

the atomic number and weight of the medium, respectively and β as defined below,

$$\tau \equiv T / m_o c^2,$$

I is the mean excitation potential of an atom in the absorbing medium,

$$F^-(\tau) \equiv 1 - \beta^2 + \frac{\frac{\tau^2}{8} - (2r+1)\ln 2}{(\tau+1)^2}, \quad \text{for electrons based on Moller cross sections for}$$

hard collisions and,

$$F^+(\tau) \equiv 2 \ln 2 - \frac{\beta^2}{12} \left\{ 23 + \frac{14}{(\tau + 2)} + \frac{10}{(\tau + 2)^2} + \frac{24}{(\tau + 2)^3} \right\}, \text{ for positrons based on}$$

Bhabha cross sections for hard collisions,

$\beta = v/c$, the charged particle velocity in units of c , (c = the speed for light in vacuum),

δ is the density or polarization effect correction for soft collisions and

C/Z is the shell correction which originates from the fact that when a charged particle passes atomic electrons with velocity not much greater than the atomic electron, the value of I is overestimated.

$$C \equiv \pi \left(\frac{N_A Z}{A} \right) r_o^2, \text{ where the number of electrons per gram of the medium is } N_A Z/A$$

and the classical electron radius is r_o .

The mass radiative stopping power expresses charged particle interactions that result in photon production, but in practice only includes bremsstrahlung from electrons and positrons. The mass radiative stopping power for electrons and positrons can be expressed as (Attix 2004):

$$\left(\frac{dT}{\rho dx} \right)_r = \sigma_o \frac{N_A Z^2}{A} (T + m_o c^2) \bar{B}_r \quad \text{Eq. 2.2}$$

where:

$$\sigma = \frac{1}{137} \left(\frac{e^2}{m_o c^2} \right)^2 \text{ is a constant and}$$

\bar{B}_r is a slowly changing function of Z and T , with a value of $\frac{16}{3}$ for $T \ll 0.5$ MeV, 6

for $T = 1$ MeV, and 12 for $T = 10$ MeV.

The dose deposited by charged particles to the medium is the product of the charged particle fluence and the mass collision stopping power.

The *restricted* mass stopping power is used when delta ray energy will potentially escape the region occupied by the medium of interest, leading to an over estimation of the energy transferred. To account for escaping delta ray energy, the stopping power is

restricted to only include delta ray production with kinetic energy less than a threshold value.

Charged particle radiation is also known as directly ionizing radiation since the majority of its energy is directly deposited in the medium as excitation and ionization events. As such, electron interactions are the main method of depositing energy in the medium.

2.2 Photon Production

The ability of electrons to create photons through bremsstrahlung is exploited by linear accelerators. As seen in equation 2.2, the mass radiative stopping power indicates that the rate of electron energy lost to bremsstrahlung is a function of the electron density and atomic number (Z) of the medium and the incident electron energy. At 100 kVp, <1% of electron energy goes to bremsstrahlung, while at 10 MeV, 20 - 40% of electron energy dissipation can be attributed to bremsstrahlung (Johns and Cunningham 1983). The energy distribution of bremsstrahlung production is uniform up to the incident electron energy in a given layer of target; however, as target thickness increases, the photons produced near the upstream surface must penetrate through subsequent layers in order to exit. This filters the beam that emerges from the target, since lower energy photons produced upstream are selectively filtered out by processes explained in the coming sections, primarily by photoelectric effect (Attix 2004). The direction of bremsstrahlung production is a function of electron energy and target thickness and becomes increasingly forward peaked at higher energy and for thinner targets (Attix 2004).

Characteristic photons are seen superimposed as sharp peaks on the continuous bremsstrahlung spectrum for lower energy beams. The maximum energy of characteristic photons is dictated by the difference in binding energy of the target material's atomic shells. The maximum energy of K-fluorescence in tungsten occurs for transition of an electron in the O_{III} shell to the K-shell, and gives off a 69.489 keV photon; however this transition is not common. 59.321 keV photons are most often observed, produced by transition from L_{III} to the K-shell.

2.3 Photon Interactions

Unlike charged particle radiation, uncharged radiation has a finite probability of passing through a medium without interacting at all. If uncharged radiation does interact, relatively few, large energy transfer events deduct all of its energy. For this reason the location, type of interaction and energy loss of single uncharged particles are all represented by probability distributions, or ‘cross sections’ for interaction and energy transfer.

Attix (Attix 2004) states that in radiological physics there are five types of photon interactions to be concerned with, each of which is important in a given energy range for a given medium and some of which dominate a general energy range, as shown in Table 2.1.

Interaction	Important energy range, MeV	Dominant energy range, MeV
Photoelectric effect	0 – 0.2	< 0.05
Compton scatter	0.09 - 10	0.2 – 2
Pair production	> 5	> 50
Rayleigh scatter	< 1	-
Photonuclear events	> 10	-

Table 2.1 Photon interactions important in radiological physics and their corresponding important and dominant energy ranges.

The first three interaction types are the most important since they result in energy transfer to electrons, which can then deposit it to the medium.

Rayleigh scattering is an elastic process that occurs when the incident photon energy is absorbed by the electrons of an atom causing them to resonate coherently, reemitting energy at the same wavelength as the input. No energy loss occurs in the process, and the redirection of photon energy is mainly in the forward direction, resulting in a slight broadening of the incident photon beam. The magnitude of angular deflection only becomes important for very low energy photons in high atomic number media.

Photonuclear interactions result in proton and neutron production. Their cross sections are relatively very small, only exist at high energies and the main cause for attention to

photonuclear interactions is neutron production at energies above 10 MeV that can lead to radio-activation and radiation safety and protection issues. Neutrons have the ability to penetrate photon mazes and can cause radio-activation of components peripheral to the target in linacs, requiring lag time between beam on and servicing these components (Attix 2004).

The kinematics and cross section for photoelectric, Compton and pair production will be examined here, as they provide the information required for simulation of these events. The relative contributions of photoelectric, Compton and pair production to the total interaction cross section are shown over a range of energies and atomic numbers in figure 2.2. The divisions indicate where the interactions to either side are equally probable, and the relative importance of these effects can be seen to correspond to the energy ranges in Table 2.1.

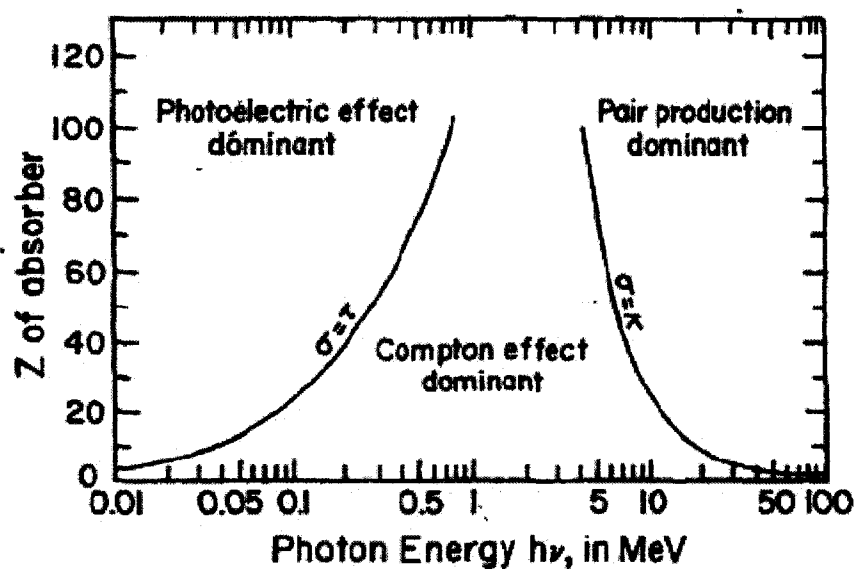


Figure 2.2 Relative contribution of photoelectric (τ), Compton (σ) and pair production (κ) to the total attenuation cross section as a function of photon energy and atomic number (Z) of the medium. Figure from (Attix 2004).

2.3.1 Photoelectric Effect

A photoelectric interaction occurs when an incident photon ejects a tightly bound atomic electron and in the process transfers all of its energy and is therefore totally absorbed. For this interaction to take place the photon must have energy greater than or equal to the binding energy of the electron. To conserve momentum, the atom absorbs a negligible

amount of energy and the ejected electron moves off with kinetic energy equal to the photon energy minus the electron binding energy. This process is shown in figure 2.3.

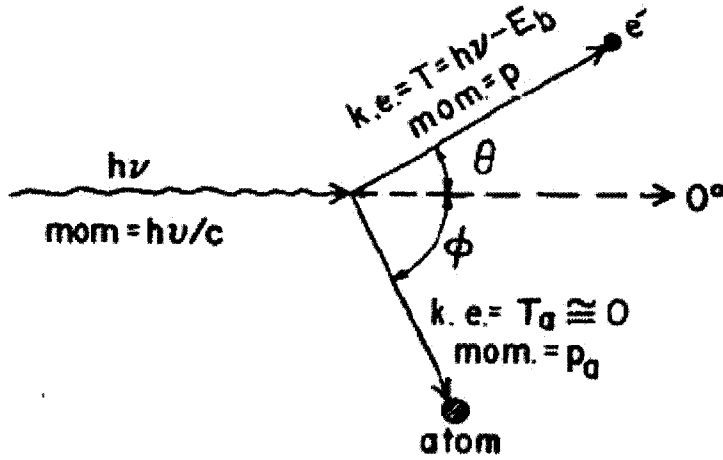


Figure 2.3 Photoelectric interaction of a photon $h\nu$ with an atomic electron. Energy and momentum are shown for all particles involved. Figure from (Attix 2004).

The electron scattering angle is independent of the kinetic energy given to it and the highest probability of photoelectric effect occurs when the incident photon energy is just greater than the electron binding energy. Photoelectric interactions increase with atomic number of the surrounding medium, and with *decreasing* photon energy, figure 2.3.

The probability of photoelectric effect is not easily quantified in an equation, like the Klein-Nishina formula for Compton scattering cross section (section 2.2.2), due to the involvement of bound electrons. The rule of thumb for the photoelectric interaction cross section per atom $_a\tau$ is:

$$_a\tau \cong k \frac{Z^n}{(h\nu)^m} \text{ (cm}^2\text{/atom)} \quad \text{Eq. 2.3}$$

where k is a constant and:

$n \cong 4$ at $h\nu = 0.1$ MeV, rising to 4.6 at $h\nu = 3$ MeV *

$m \cong 3$ at $h\nu = 0.1$ MeV, falling to approximately 1 at $h\nu = 5$ MeV

* n is also a weak function of atomic number, having higher values for low Z and lower values for high Z materials.

In the energy range below 0.1 MeV, where photoelectric effect becomes most important, the photoelectric interaction cross section per atom can be expressed as:

$${}_a\tau \approx \infty \frac{Z^4}{(h\nu)^3} \text{ (cm}^2\text{/atom)} \quad \text{Eq. 2.4}$$

or, the mass interaction cross section:

$$\frac{{}_a\tau}{\rho} \approx \infty \left(\frac{Z}{h\nu} \right)^3 \text{ (cm}^2\text{/g)} \quad \text{Eq. 2.5}$$

The fraction of the incident photon energy transferred to the ejected electron is:

$$\frac{T}{h\nu} = \frac{h\nu - E_b}{h\nu} \quad \text{Eq. 2.6}$$

where E_b is the binding energy of the electron.

Photoelectric effect leaves the atom in the same state as a charged particle hard collision resulting in delta ray emission; both events leave a vacancy in a lower electron shell. It is instructive to find the total energy transfer cross section for the photoelectric event: the amount of energy transferred to the medium that is not then lost back to radiative energy as the atom relaxes back to a stable state.

To evaluate the fraction of the original photon energy transferred in a photoelectric event, the fraction of all photoelectric interactions that occur in a given atomic shell is found first, (P_k) . Multiplying by the fractional characteristic x-ray yield for that shell (Y_k) and the mean energy per x-ray $(\overline{h\nu})_k$ gives the mean energy radiated from the given shell per photoelectric interaction. The energy per x-ray can vary since any higher shell can donate electrons to lower shells, even though transitions from the adjacent shells are most common. The subscript K was used in the nomenclature above to denote the shell of the original vacancy; this could be any atomic shell but contributions from the K shell are most significant, with the L shell sometimes evaluated as well. Some shells are excluded by quantum limited transitions.

As a result the energy transfer cross section for photoelectric effect can be expressed as:

$$\frac{\tau_{tr}}{\rho} = \frac{\tau}{\rho} \left[\frac{h\nu - P_K Y_K (\overline{h\nu})_K - P_L Y_L (\overline{h\nu})_L}{h\nu} \right] \text{ (cm}^2\text{/g)} \quad \text{Eq. 2.7}$$

for photon energies exceeding the K-shell binding energy and:

$$\frac{\tau_{tr}}{\rho} = \frac{\tau}{\rho} \left[\frac{h\nu - P_L Y_L(\overline{h\nu})_L}{h\nu} \right] \text{ (cm}^2\text{/g)} \quad \text{Eq. 2.8}$$

for photon energies between the L and K-shell binding energies.

To simulate a photoelectric interaction, the incident photon energy and the atomic number of the medium must be known, along with the binding shell energies. The total interaction cross section can then be determined and the probability per shell used to find the appropriate binding energy to calculate the ejected electron energy. Fractional yields can then be used to find the energy transferred to the medium per event.

The photoelectric effect is the primary method for internal absorption of low energy bremsstrahlung photons produced in standard linac therapy beam targets, which are made of high Z materials. Increased photoelectric absorption in high Z media is exploited in detector design, using high Z screen materials to increase detection efficiency. The energy of kV imaging photons is low enough that it can take advantage of the Z^4 dependence of photoelectric effect per atom to accentuate contrast between biological tissues, whereas MV photons are outside the energy range where photoelectric interactions contribute significantly to overall attenuation.

2.3.2 Compton Interactions

Thomson first looked at this type of interaction for energy < 0.01 MeV, describing an electron vibrating in the electric field of an incident photon, then reemitting the photon at the same energy but redirected by some angle. As higher energies were observed, Thomson's theory was found to overestimate the scattered photon energy, which begins to diverge from the incident energy at about 0.05 MeV. Compton interactions were then described as a photon scattering off an electron assumed to be unbound and stationary, where some fraction of the incident photon energy is transferred to electron kinetic energy in the process, figure 2.4. At very low incident photon energy, the fraction of energy transferred to the electron is negligible and converges to Thomson's theory. As incident photon energy increases, the more forward directed both the electron and the scattered photon are. The assumption that electrons are unbound and stationary is not generally true since most electrons in a medium are associated with an atom. However,

the difference in energy between the valence and conduction band electrons in the medium and the incident photon energy is large enough that under most conditions this is a good assumption. The conditions under which accounting for electron binding becomes important are low energy photons in high atomic number media – the same conditions where the majority of photon interaction are dominated by the photoelectric effect. This means that correcting the Compton contribution to the total interaction cross section for binding energy results in <1% change in value of the total interaction cross section, μ (Attix 2004).

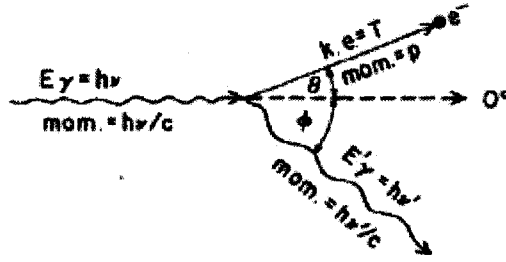


Figure 2.4 Compton interaction of a photon $h\nu$ with electron, assumed unbound and stationary. Energy and momentum are shown for all particles involved. Figure from (Attix 2004).

Thomson had developed an equation for the interaction cross section based on the classical electromagnetic model of the electron. When Klein and Nishina (K-N) adapted Thomson's cross section equation to Dirac's relativistic theory of the electron, agreement with measured cross sections was achieved at high energy (Attix 2004). For an incident photon of energy $h\nu$, that scatters at an angle ϕ relative to its original path with energy $h\nu'$, the differential K-N cross section per unit solid angle per electron, is represented by equation 2.9:

$$\frac{d_e\sigma}{d\Omega_\phi} = \frac{r_o^2}{2} \left(\frac{h\nu'}{h\nu} \right)^2 \left(\frac{h\nu}{h\nu'} + \frac{h\nu'}{h\nu} - \sin^2 \phi \right) \quad \text{Eq. 2.9}$$

which, when integrated over all angles, becomes the total interaction cross section for the Compton effect per electron:

$$_e\sigma = 2\pi r_o^2 \left\{ \frac{1+\alpha}{\alpha^2} \left[\frac{2(1+\alpha)}{1+2\alpha} - \frac{\ln(1+2\alpha)}{\alpha} \right] + \frac{\ln(1+2\alpha)}{2\alpha} - \frac{1+3\alpha}{(1+2\alpha)^2} \right\} (\text{cm}^2/e) \quad \text{Eq. 2.10}$$

where, for an incident photon energy of $h\nu$, $\alpha = h\nu/m_0c^2$.

The fraction of the incident photon energy transferred to the electron is: $T = \frac{h\nu - h\nu'}{h\nu}$.

Multiplication of the differential K-N cross section per unit solid angle per electron with the fraction of the incident photon energy transferred to the electron and then integrating over all angles yields the mass energy transfer cross section per electron:

$${}_e\sigma_{tr} = 2\pi r_o^2 \left[\frac{2(1+\alpha)^2}{\alpha^2(1+2\alpha)} - \frac{1+3\alpha}{(1+2\alpha)^2} - \frac{(1+\alpha)(2\alpha^2-2\alpha-1)}{\alpha^2(1+2\alpha)^2} - \frac{4\alpha^2}{3(1+2\alpha)^3} - \dots \right. \\ \left. \left(\frac{1+\alpha}{\alpha^3} - \frac{1}{2\alpha} + \frac{1}{2\alpha^3} \right) \ln(1+2\alpha) \right] \text{ (cm}^2/\text{e)} \quad \text{Eq. 2.11}$$

To simulate the Compton effect the initial conditions required are: the electron density of the medium and the energy and direction of the incident photon. From these inputs, the total interaction cross section per electron gives the probability distribution for a Compton event to occur and the energy transfer cross section will give the resulting electron energy, T . From this, the angle of scatter of both the photon (φ), and the electron (ϑ), relative to the incident photon direction can be found via the following relationships, derived from energy and momentum conservation in relativistic Compton kinematics:

$$T = h\nu - h\nu' \quad \text{Eq. 2.12a}$$

$$h\nu' = \frac{h\nu}{1 + \left(\frac{h\nu}{m_o c^2} \right) (1 - \cos \varphi)} \quad \text{Eq. 2.12b}$$

$$\cot \vartheta = 1 + \left(\frac{h\nu}{m_o c^2} \right) \tan \left(\frac{\varphi}{2} \right) \quad \text{Eq. 2.12c}$$

where $m_o c^2$ is the rest mass of the electron, equal to 511 keV.

The Compton effect is the main mechanism of photon attenuation in the MV energy range used for radiation therapy, and due to similar electron density between biological tissues, results in fairly uniform energy transfer to all structures. The directly-proportional relationship between electron density of the medium and the Compton interaction cross section means that MV image contrast is effectively an electron density

map of the materials in the field of view. In addition, the metallic buildup layer preceding the screen in MV image detectors uses Compton interactions to produce Compton recoil electrons that can then be more efficiently absorbed in the screen.

2.3.3 Pair Production

Pair production is the dominant method of photon interaction in tissue above 50 MeV, and is possible for photon energy greater than 1.022 MeV. When a photon interacts with the electric field of an atomic nucleus, the photon can be converted to an electron-positron pair, each with rest mass energy of 511 keV, figure 2.5. The lower energy limit for this interaction is the combined rest mass energy. Any additional energy is carried away as positron/electron kinetic energy. There are no specific rules for division of extra energy between the positron/electron pair; however, the positron normally emerges with slightly greater energy than the electron due to the atom's Coulombic force on the oppositely charged particles. The positron proceeds in the same manner as an electron; losing energy in multiple small ionization/excitation interactions, until it approaches rest when it can annihilate with a free electron, creating two 511 keV, gamma rays which are emitted on average at 180° to one another, conserving momentum.

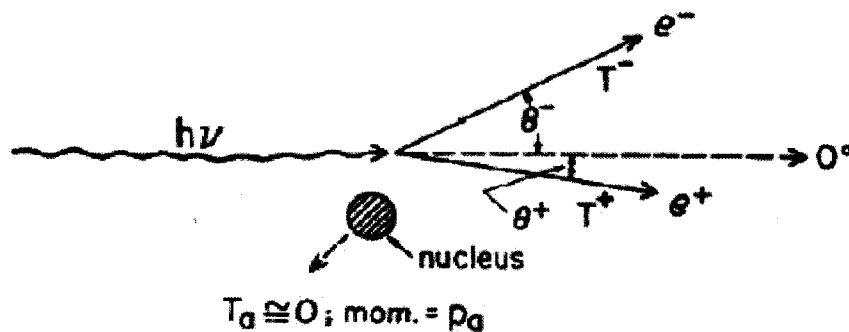


Figure 2.5 Pair production interaction of a photon $h\nu$ with the field of an atomic nucleus, producing an electron e^- and a positron, e^+ . Any photon energy, in addition to the rest mass energy of the charged pair created, goes into kinetic energy of charged particle, scattering them at angles $\neq 180^\circ$ relative to one another. Figure from (Attix 2004).

For energies substantially above the threshold for pair production, an electron and positron with average kinetic energy \bar{T} are forward directed with an approximate mean angle $\bar{\theta}$ of:

$$\bar{\theta} \cong \frac{m_o c^2}{\bar{T}} \text{ radians} \quad \text{Eq. 2.13}$$

The pair production interaction cross section per atom is:

$$_a\kappa = \frac{r_o^2}{137} Z^2 \bar{P} \text{ (cm}^2\text{/atom)} \quad \text{Eq.2.14}$$

or

$$\frac{\kappa}{\rho} = \frac{r_o^2}{137} Z \bar{P} \text{ (cm}^2\text{/g)} \quad \text{Eq.2.15}$$

Where P is a function of both $h\nu$ and Z, arrived at analytically (Attix 2004).

The mass energy-transfer cross section for pair production is:

$$\frac{\kappa_{tr}}{\rho} = \frac{\kappa}{\rho} \left(\frac{h\nu - 2m_o c^2}{h\nu} \right) \text{ (cm}^2\text{/g)} \quad \text{Eq. 2.16}$$

For simulation, the incident photon energy and the atomic number of the medium are required. The total pair production interaction cross section can then be used to find the probability of pair production occurring and the cross section per unit positron energy to find the kinetic energy of the resultant charged particles. At high enough energy, the mean scattering angle can be estimated from the mean charged particle kinetic energy. The mean energy of a 6 MeV beam is approximately 1/3 of the maximum, therefore, 2 MeV (Johns and Cunningham 1983). At this energy in tungsten, a small but significant fraction of photon interactions are pair production (figure 2.2) resulting in a spectral peak in the 6 MV therapy beam at 511 keV due to positron annihilation, as shown in figure 1.2.

2.3.4 Triplet Production

If the incident photon has sufficient energy, (≥ 2.04 MeV), it can interact with the Coulomb field of an electron instead of that belonging to the nucleus and produce the electron/positron pair as well as ejecting the electron from the atom, thus ‘triplet

production'. Triplet production is a small fraction of pair production, and therefore their effects are combined (Attix 2004).

2.4 Photon Beam Measurements and Characteristics

The total mass interaction cross section can be found by summing the effects of photoelectric, Compton and pair production interactions:

$$\frac{\mu}{\rho} = \frac{\tau}{\rho} + \frac{\sigma}{\rho} + \frac{\kappa}{\rho} \quad \text{Eq.2.17}$$

This can also be done to find the total mass energy transfer cross section. The product of the total mass interaction cross section with density is referred to as the linear attenuation coefficient (μ) and has units of photons/cm.

Photons and other uncharged radiation are considered *indirectly ionizing* radiation: the energy they transfer to the medium is not directly absorbed, but instead produces energetic electrons which then deposit the energy in direct excitation and ionization interactions to the medium. This suggests that, if the charged particles depositing dose have significant range, the energy absorbed by the medium will lag the energy transferred to the medium as a function of depth.

Extensive characterization is required for all beams used in radiation therapy to ensure accurate prediction of dose at all locations within the beam. To measure the photon beam characteristics, ion chambers are typically used to quantify dose to water.

Ion Chambers

The basic design of an ion chamber consists of a charge collecting cavity containing an ion-collecting gas and a set of electrodes is surrounding by the cavity wall. When placed within a medium and irradiated, the gas in the cavity is ionized by interactions within its volume and the resulting ions collected on the electrodes, giving a measurement of charge density, in C/m³. Using the energy required to produce the ion pair, and knowing the volume and density of gas, charge density can be converted into dose (J/kg) to the gas. To convert this to dose to water, the Bragg-Gray cavity theory can be used.

Dose from charged particles interactions can be evaluated as the product of charged particle fluence and the mass collision stopping power. Assuming that the charged

particle fluence is not changed when passing from one medium to the other, i.e. particle are not backscattered at the interface, the Bragg-Gray cavity theory can be written:

$$\frac{D_w}{D_g} = \frac{{}_m\bar{S}_w}{{}_m\bar{S}_g} \quad \text{Eq. 2.18}$$

Where:

$D_{w(g)}$ is the dose to the chamber wall (gas)

${}_m\bar{S}_{w(g)}$ is the average mass collision stopping power for the wall (gas) evaluated as:

$${}_m\bar{S}_{w(g)} \equiv \frac{\int_0^{T_{\max}} \Phi_T \left(\frac{dT}{\rho dx} \right)_{c,w(g)} dT}{\int_0^{T_{\max}} \Phi_T dT} \quad \text{Eq. 2.19}$$

where Φ_T is the energy spectrum of the beam and $\left(\frac{dT}{\rho dx} \right)_{c,w(g)}$ is the mass collisional

stopping power of the wall (gas).

This theory states that the ratio of the dose absorbed in the wall of the chamber to that absorbed in the gas is equal to the ratio of the mean mass collision stopping power for the wall material to that for the gas. As long as the thickness of gas is insufficient to disturb the charged particle field, a chamber with walls made of water equivalent plastic, can then be used to calculate dose to water from the dose to gas (Attix 2004). Typically the gas used is air.

When using gas filled chambers, the difference in density between the gas and the wall causes a shift in the effective measurement location. The relative density of the gas to wall material means the same interactions that would occur in a thin layer of wall are spread over a larger range in the less-dense gas. To correct for this, measurements are shifted upstream by a fraction of the ion chamber diameter corresponding to the relative densities (Almond, Biggs et al. 1999).

Water is used as the measurement medium for two main reasons: it is easily available and the radiological properties of tissue are similar to those of water (Johns and Cunningham 1983). Percent depth dose (PDD) curves measure the dose to water as a function of depth

for a specific field size, beam energy and source to surface distance (SSD). A typical PDD for a 6 MV therapy beam is shown in figure 2.6a. At shallow depths, the dose builds up rapidly to a maximum value, at depth specified as d_{\max} , then gradually decreases with increasing depth. The initial rapid increase is caused by the building number of secondary charged particles passing through a given depth. Although the number of energetic charged particles set in motion decreases with depth as the photon fluence is attenuated, the secondary electrons produced in photon interactions upstream continue to deposit dose downstream. The fluence of secondary charged particles passing through a given depth thus increases to a maximum value, at d_{\max} , then gradually falls off, lagging the fall off in energy transfer caused by attenuation of the photon beam.

Standard therapy beams pass through flattening filtration before exiting the linac. The flattening filter spatially modulates the photon fluence so that, under a predefined set of conditions downstream, a uniform radiation field will be produced. Filter thickness decreases radially to compensate for the forward peaked bremsstrahlung beam. This results in a lower mean photon energy at the perimeter compared to central axis since the larger on-axis filter thickness absorbs a larger fraction of the low energy photon population. When examining radial dose profiles downstream in water, this results in higher dose at the periphery of fields at shallower depths (figure 2.6b) than filter flatness conditions and lower peripheral dose at depths greater (figure 2.6c) than the flatness conditions. The raised peripheral dose at shallow depth is often referred to as ‘beam horns’, while the decreased peripheral dose at increased depth is referred to as a ‘shoulder’.

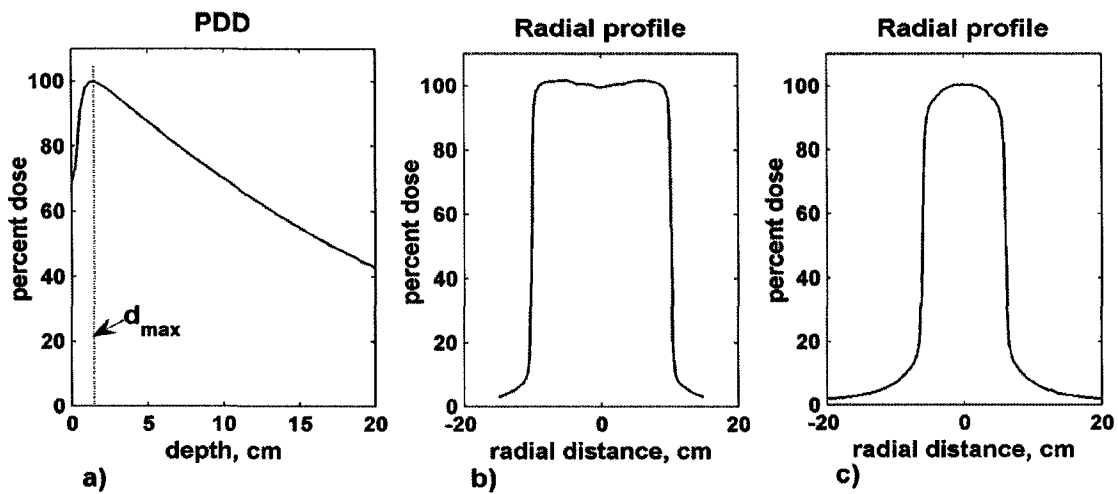


Figure 2.6 Photon beam characteristic curves. (a) PDD, (b) beam horns and (c) shoulder in radial profiles.

2.5 Radiographical Imaging

Figure 1.2 demonstrated that the ratio of mass attenuation coefficients of bone versus muscle is only non-unity at energies less than approximately 200 keV. By examining the effective atomic numbers and electron densities of these two biological materials, along with the cross section for photon interactions as a function of energy, it is possible to explain why differential attenuation exists only at low energy. Table 2.2 shows the effective Z and electron density of bone and muscle. In equations 2.4 and 2.10, the photoelectric and Compton cross sections per electron can be shown to be proportional to Z^3 and electron density, respectively. Table 2.3 shows a comparison of the ratio of attenuation per electron in bone versus tissue for both photoelectric and Compton interactions. If we turn to figure 2.2, it is seen that the proportion of photons interacting via photoelectric effect at energies less than 200 keV is greater than that at higher MV energies.

Material	Z_{eff}	$\rho_e, 10^{23} \text{ electrons/g}$
Tissue	~ 7.6	3.312
Bone	~ 12.3	3.192

Table 2.2 Effective atomic number and electron density for bone and tissue. Data from (Johns and Cunningham 1983)

	τ_e	σ_e
Bone vs. Tissue	$(Z_{\text{BONE}})^3 / (Z_{\text{TISSUE}})^3$	$(\sigma_{e,\text{BONE}}) / (\sigma_{e,\text{TISSUE}})$
	= 4.2	= 0.96

Table 2.3 Comparison of the ratio of attenuation in bone versus tissue for both photoelectric and Compton interactions.

2.6 Monte Carlo Radiation Transport

Monte Carlo calculations are a class of computational algorithms that use continual random sampling of probability distributions to arrive at a result. They are useful for simulation of stochastic events, where the outcome of any single event cannot be calculated from the initial conditions; however, if a group of interactions occur they will have a known probability distribution. Complex systems are another appropriate application for Monte Carlo techniques, where the sum of interactions between variables is difficult to characterize analytically. These features make coupled electron-photon radiation transport an ideal candidate for Monte Carlo simulation by sampling of interaction cross sections and stopping powers.

2.6.1 Probability Distributions and Random Sampling

Pseudo random number generators can produce uniform distributions of random numbers. To apply these to Monte Carlo simulation, the uniform distribution must be redistributed so that it corresponds to the probability distribution of the parameter one wishes to sample.

For example, the first step in propagating a photon through a modeled medium is determining the distance to interaction. Attenuation of uncharged radiation in a medium is an exponential function of distance and follows:

$$N = N_0 e^{-\mu x} \quad \text{Eq. 2.20}$$

Where N is the number of photons left at depth x in a medium with linear attenuation coefficient μ , from N_0 incident photons (Attix 2004).

By using the cumulative distribution of interactions over all x as the probability distribution for random sampling, the range of random numbers assigned to the

probability of interaction at location x yields an accurate result for the location of uncharged radiation interactions can be obtained over a large number of events.

2.6.2 EGSnrc

The Electron Gamma Shower (EGS) Monte Carlo code for coupled electron-photon transport was originally developed to predict experimental outcomes and to design shielding for high energy particle accelerators at the Stanford Linear Accelerator Center (SLAC) (Bielajew, Hirayama et al. 1994 ; Rogers 2006). It is presently maintained by the Ionizing Radiation Standards (IRS) group at the National Research Council (NRC) of Canada (Rogers, Walters et al. 2006).

EGSnrc user codes BEAMnrc and DOSXYZnrc are used to select initial conditions and to specify geometry and composition for the transport environment, and the attenuation cross sections and stopping powers are precalculated and stored using the Preprocessing for EGS program (PEGS). EGSnrc then follows each particle/photon track through the simulation media, following the chain shown in figure 2.7 for the primary particles and their progeny. Approximate efficiency-improving techniques and variance reduction techniques described in section 3.1.7 are used to reduce calculation time.

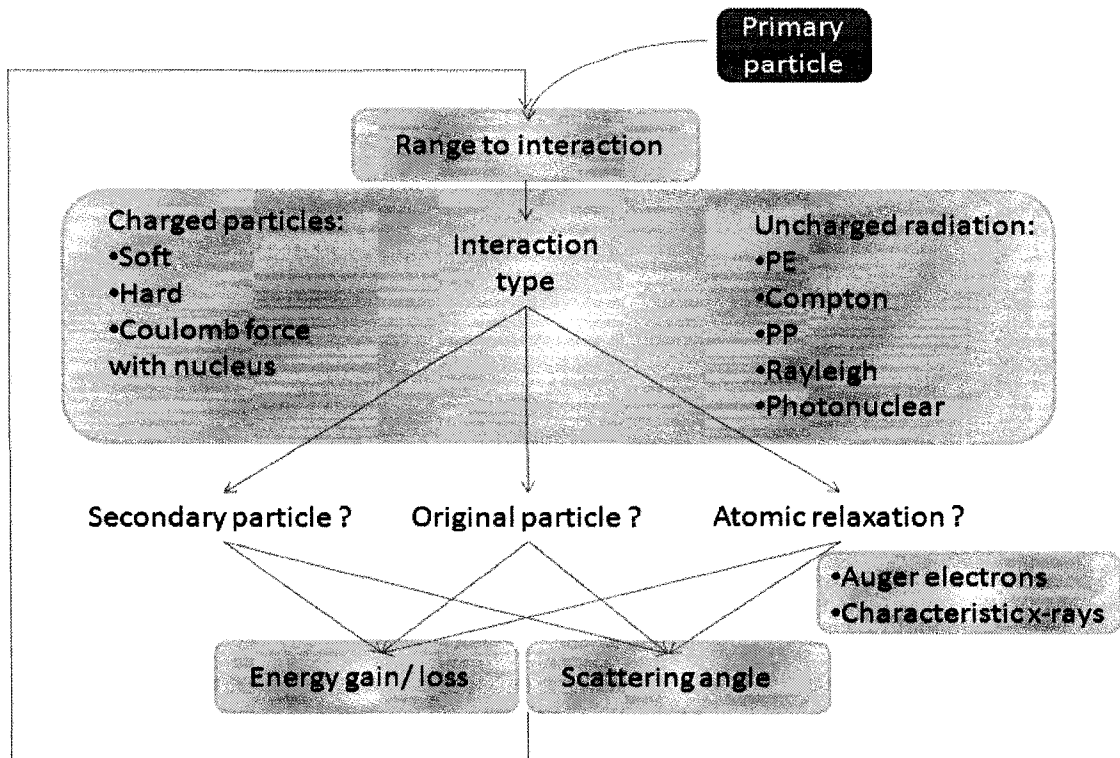


Figure 2.7 The basic chain of steps for radiation transport. The light blue boxes signify where stochastic events take place, requiring random probability distribution sampling in Monte Carlo simulation.

CHAPTER 3 Materials and Methods

3.1 6 MV and Experimental Low-Z Beams

3.1.1 Clinical Linear Accelerators

Clinical linear accelerators (linacs) are used to produce high energy electrons and photons for external beam radiation therapy. The linac used for this work was a Varian 2100EX (Varian Medical, Palo Alto, CA). The following paragraph gives a general overview of linac components and the production of high energy photon beams.

The clinical linear accelerator produces high energy photon beams by accelerating electrons to high energy, in vacuum with a high power carrier wave from a Klystron or magnetron, and allowing them to strike a high atomic number transmission target. The electron energies used in therapy begin at 4 MeV and typically range up to about 20 MeV, although higher energies are possible. In the target, bremsstrahlung and characteristic processes generate a photon population, whose energy ranges from zero up to the incident energy of the source electrons. Typical therapy targets are made of tungsten, copper or lead, all relatively high atomic number materials, which results in internal absorption of a large fraction of the low energy photon population via photoelectric effect (Galbraith 1989; Mah, Galbraith et al. 1993; Ostapiak, O'Brien et al. 1998; Tsechanski, Bielajew et al. 1998; Flampouri, Evans et al. 2002). The forward directed portion of the photon beam exits the target and passes through primary collimation. Up to this point all components have been in vacuum. At the exit of the primary collimation, the beam passes into air through a thin, Be exit window. Due to the forward peaked nature of bremsstrahlung production, the beam next passes through the flattening filter, a component whose purpose it is to attenuate the photon beam in such a way that under certain conditions downstream a uniform dose will be deposited across the field. The standard conditions under which flattening filtration is designed to produce a flat response, within the central 80% of the field, are: a 10 x 10 cm² field at depth 10 cm in water, located at 100 cm source to surface distance (SSD). The composition of the filter is chosen to minimize attenuation of photons in the desired energy range, for example at lower energies (4 MeV) a higher Z material is chosen and at higher electron

energies (18 MeV) a medium Z material such as Cu is used, both combinations keeping the dominant form of photon interaction in the Compton range. The thickness of the filter is spatially modulated to give a distribution of photons whose combined spatial fluence and energy satisfy the pre-defined set of conditions. The target and flattening filtration are specific for each photon energy. Electron modes have scattering foils at the same position in the beam line as the flattening filters. The flattening filters and electron scattering foils are set into a rotating carousel, which can place the correct component into the beam line, for the desired beam. The monitor chambers are a set of two parallel plate ion chambers that monitor the output, flatness and symmetry of the beam. Their measurements are part of a feed-back loop to the electron gun current that ensures a constant dose rate, within a preset tolerance. Their output is translated to monitor units (MU), a measure corresponding to a dose of 1 cGy under pre-defined calibration conditions. A thin mirror next allows a light source, placed outside the beam-line, to be reflected through the remaining downstream components providing a visual representation of the radiation field. The components below the mirror are field specific – for a given electron/photon beam they define the beam limits, and are called secondary /tertiary collimation. Secondary collimation normally refers to two sets of orthogonally oriented blocks of high atomic number material called jaws. Their inner faces are angled, aligning parallel to the beam line, and they are thick enough to block radiation outside their aperture. Multiple types of tertiary collimation and beam defining accessories can be chosen to further define the beam shape, and can be attached to the outside of the linac head using accessory mounts. Upon leaving the accelerator head, the beam passes through a thin Mylar window, the goal of which is mainly for visualization, since it has a set of crosshairs that with the light field from the mirror upstream delineate where the central axis of the beam and the in-plane and cross-plane axes occur. The main components of the accelerator in 6 MV photon mode are shown in Part 1 of figure 3.1.

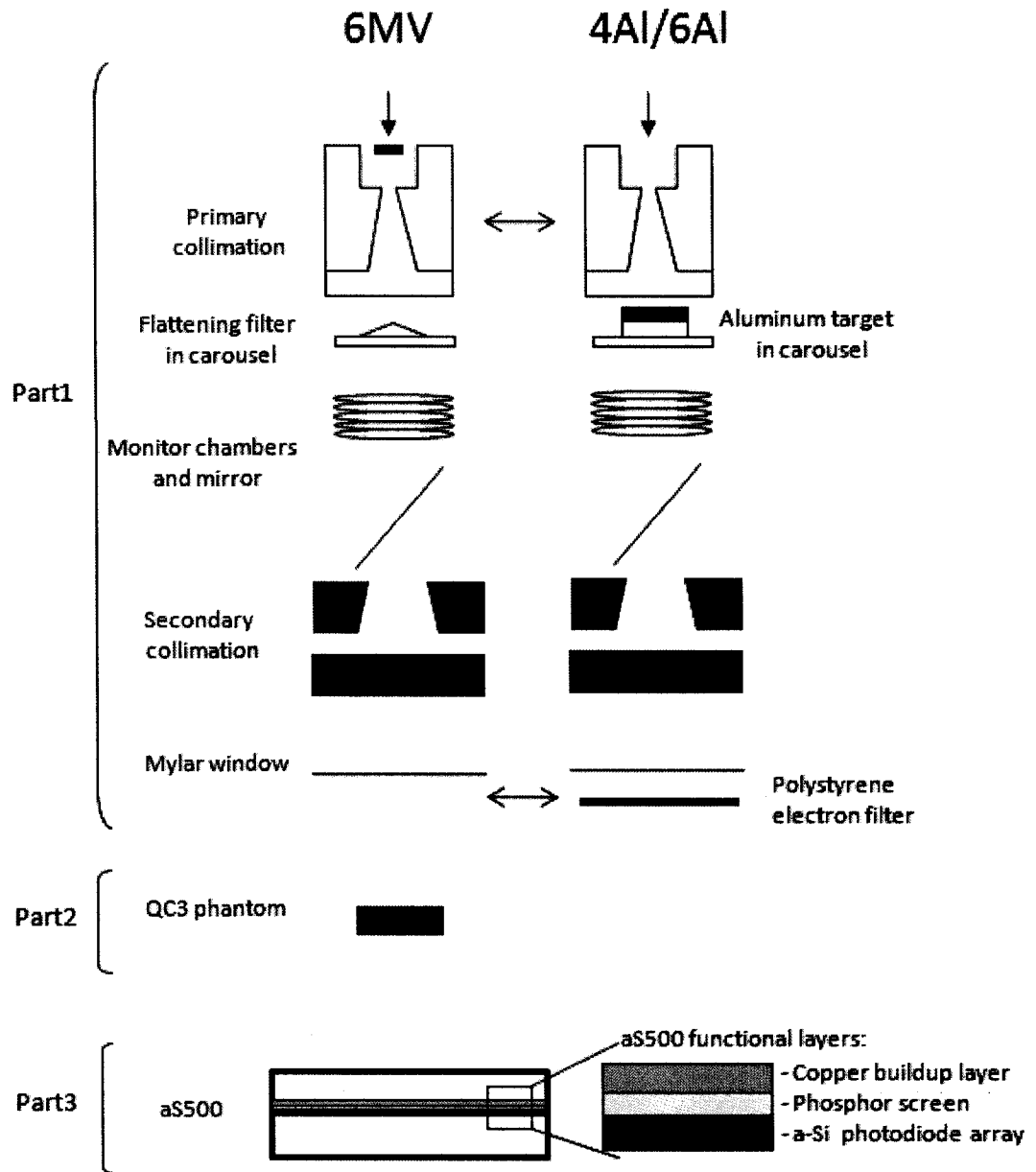


Figure 3.1 Diagram of the linac, contrast phantom and image detector. Part 1: major components of the linear accelerator head in both standard 6 MV mode (target above primary collimation, flattening filter aligned with beam in carousel) and in the experimental aluminum configuration (electron mode, aluminum target aligned with beam in carousel and electron filter in upper wedge mount). Part 2: QC3 phantom, surface located at approximately 99.1 cm SSD. Part 3: aS500 EPID with an expanded view of the main functional layers.

3.1.2 Experimental Low-Z Target Beam

A low-Z target is incorporated in the linac by installing it in an otherwise unused port of the carousel, figure 3.2a. The linac is run in electron mode and manual selection of the carousel position is performed by accessing the carousel-mode/BMAG board in the linac stand. Since the target is not sufficiently thick to stop all incident electrons, a 0.9 cm-thick polystyrene filter is inserted into the upper accessory mount to remove electron contamination. These modifications are compared to the standard 6 MV beam configuration in Part 1 of figure 3.1.

Low-Z-target beams had been produced previously in our clinic for investigating potential dose enhancement in tumors injected with an iodinated contrast medium to raise their effective atomic number (Robar 2006). Previous work was performed on a Varian 2100C linac that does not have an amorphous silicon detector and targets were housed in collars that positioned their surface flush with the carousel surface, figure 3.2b, leaving a 2.47 cm air gap between exiting vacuum and the target surface, allowing the electron beam to scatter significantly prior to impinging on the target. The 1.0 cm Al target was relocated to the 2100EX (with a-Si detector) and the target location was improved, from an imaging standpoint, by extending the collar shaft towards the exit of the primary collimation, figure 3.2b.

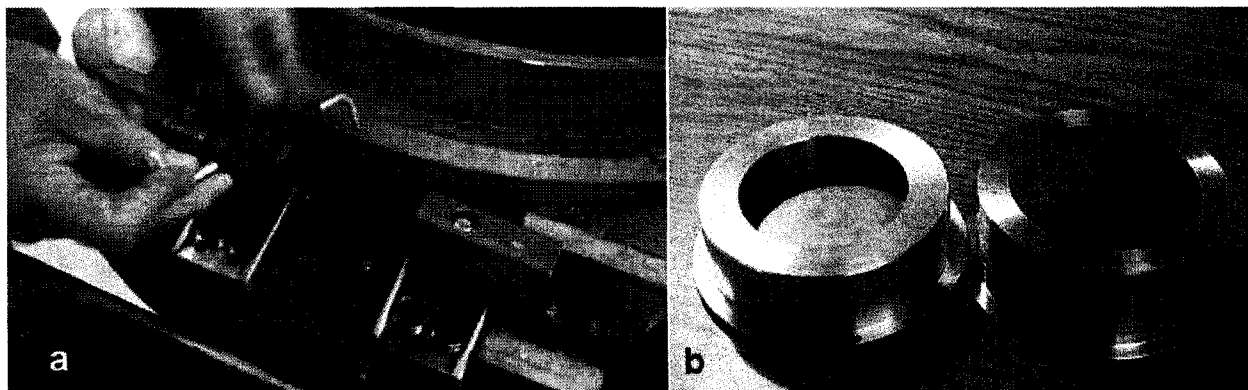


Figure 3.2 Low-Z targets. a) inserting low-Z custom target into linac carousel, b) the custom targets in their original and elevated style collars

3.1.3 Low-Z Target Position

To determine the maximum potential elevation of the target, a nylon target collar, with height equal to the distance between the carousel and the Be window, was manufactured. The collar was inserted in one of the carousel ports and manually rotated towards the beam line. This procedure was performed very carefully since this is a clinical machine and is required daily for treatment – breaking the thin Be window holding vacuum would be both expensive and time consuming to fix. The collar height was gradually decreased until, when inserted in the carousel, it could make a full rotation without obstruction. The final height was found to be less than the distance between the Be window and the carousel in the manufacturer's specifications.

The elevated collar brings the proximal target surface to within 9.0 mm of the Be exit window, reducing scattering of the electron beam in air prior to incidence on the target, compared to previous work (which would increase focal spot size and degrade image resolution). Figure 3.2b shows the custom targets in their original and elevated style holders. The target is an aluminum disk 5 cm diameter and 1 cm thick, corresponding to approximately 60% of the CSDA range of 6 MeV electrons, following the work of Flampouri *et al* (Flampouri, Evans et al. 2002) who showed maximum efficiency at this thickness Al target.

3.1.4 Linac Head Modeling in Beamnrc

The first course on the EGS4 Monte Carlo code was offered in 1986 and it was observed over the first four course offerings, that more than half of the EGS4 users were applying the code to clinical accelerators using simplistic models. In response to interest in highly detailed modeling of radiation therapy sources, BEAMnrc (Rogers, Faddegon et al. 1995) was created by Canada's National Research Council as a general purpose EGS user code for this expressed purpose (Rogers 2006).

BEAMnrc provides a platform for definition of each basic component of the clinical accelerator treatment head within a generic set of component modules (CMs), the source characteristics and the parameters controlling simulation efficiency. In the main inputs section, planes can be specified where all information about particles passing through that plane is recorded in a file, known as a phase space. The phase space file can then be used

as a source for sequential BEAMnrc simulations or for scoring dose using DOSXYZnrc, (section 3.2.2). Two seeds are also specified in the main inputs section to serve as a starting point for pseudo-random number generation of particle transport in EGSnrc.

3.1.5 Component Modules

Each element of the linear accelerator head exists as a generic component module (CM) in BEAMnrc. To begin building an accelerator model in BEAMnrc, the component modules are selected in order and named. The geometry, composition and location are then specified for each component module. In addition, a ‘latch’ can be assigned to each piece of the CM, allowing particles which interact in that region, and their progeny, to be identified in subsequent phase space files. Once the accelerator geometry is complete and saved, the accelerator must be compiled before a simulation can be run. If a change is made to the component modules, the accelerator must be recompiled.

3.1.6 Source Parameters

BEAMnrc has multiple source routine options. In general, the incident particle type, energy and spatial extent must be defined. The source routines used here are parallel circular beam (ISOIRC = 0) and full phase space source (i.e. the phase space output from a prior BEAMnrc simulation, ISOIRC = 21). A parallel circular-shaped beam with Gaussian distribution is an alternate option for modeling the initial electron beam, (ISOIRC = 19).

3.1.7 Parameters for Increasing Efficiency

In EGSnrc there are two groups of methods for increasing efficiency:

- Approximate efficiency improving techniques (AEITs)
- Variance reduction techniques (VRTs)

While VRTs do not alter the physics involved, AEITs make approximations that can compromise the accuracy of results if improper control parameters are chosen.

AEITs include:

Global cut-off energies – once the particle energy reaches a threshold value, (the parameter ECUT for electrons, PCUT for photons), it is assumed that any further

interaction will produce the same result as terminating the particle and depositing its energy locally. Careful selection of these energies is important to preserve calculation accuracy. Typical values used for radiation therapy simulation, where the initial energy range (including rest mass energy) is on the order of 1-10 MeV, are $ECUT = 0.7$ MeV and $PCUT = 0.01$ MeV, or $ECUT = 0.521$ MeV / $PCUT = 0.01$ MeV if low energy electron interactions are important (Rogers, Faddegon et al. 1995). The simulation efficiency is highly dependent on the value of $ECUT$, since the majority of calculation time is spent on electron transport.

Range rejection – if an electron's energy is not sufficient to reach the next material boundary the electron is terminated and its energy deposited locally. This introduces an approximation by assuming the bremsstrahlung photons produced by additional electron interactions will not escape the current region and can introduce inaccuracy particularly when large regions are used. The maximum electron energy considered for range rejection is $ESAVE_GLOBAL$, which can be used to minimize inaccuracies when using this technique (Rogers, Walters et al. 2006).

Condensed history technique – is the most important method for increasing the efficiency of electron transport. By recognizing that many electron interactions involve small angle scatter and small energy losses, interactions can be grouped into steps; this is known as the condensed history technique (Rogers, Walters et al. 2006). Results can vary significantly depending on the step size chosen; therefore CHT is an AEIT. The default value for the maximum fractional energy loss per electron step is ($ESTEPE$) 0.25 and should not be changed unless using the older version electron transport algorithm, $PRESTA-I$ (Rogers, Walters et al. 2006).

Based on the energy required to produce an ion pair in air, $W = 33.85$ eV (Attix 2004), an electron with energy in the range used for radiation therapy (4-20 MeV) will undergo on the order of 300,000 interactions before coming to rest. Compared to the relative number of events per photon, electron transport is far more computationally demanding. All of the above AEITs involve electron tracking which, in the target especially, is the most computationally intensive part of Monte Carlo photon beam simulation since only 2-3% of electron interactions result in photon production and the rest of the electron trajectory

is of little interest. The following VRT is aimed to increase photons statistics without making approximations.

Bremsstrahlung splitting - is a method for increasing the efficiency of photon production, where each primary bremsstrahlung event results in NBRSP photons which are each assigned a weight of $1/\text{NBRSP}$ to preserve dose scoring statistics downstream. The algorithms associated with Bremsstrahlung splitting have progressed through three stages, becoming increasingly efficient. First generation splitting, Uniform Bremsstrahlung Splitting (UBS), amplifies photon production but does not impose any restriction on the angle at which split photons are emitted and while the number of photons produced increases, time is wasted following photons that have little probability of reaching the phase space plane (i.e. those photons traveling backwards towards the electron source). The next generation, Selective Bremsstrahlung splitting (SBS), uses the incident electron energy and direction to determine the probability of the resultant photons reaching a user-defined field downstream (specified at some distance downstream by a splitting field radius and splitting field distance) and then chooses the a splitting number within a user-defined range based on the probability of the resultant photons reaching the field. This reduces the number of extraneous histories, but the third generation splitting algorithm, Directional Bremsstrahlung Splitting (DBS), removes tracking of split-weight photons that likely won't make it to the field. DBS results in efficiencies up to 8 times that of SBS and 20 times UBS and results in a large number of low-weight photons inside and a few high-weight photons outside the field (Rogers, Walters et al. 2006). Similar to SBS, a user defined field allows selective Bremsstrahlung production into the field of view. The DBS algorithm then projects photons produced in splitting events toward the pre-selected field of view. If the photon trajectory places it within this field, the photon is kept and assigned a weight equal to $1/\text{the splitting number}$. If the trajectory places the photon outside the field, Russian Roulette (RR) is played, where the probability of keeping the photon is $1/\text{the splitting number}$. If this photon survives, it is assigned a greater weight to represent all photons outside the desired field that are eliminated by this procedure. DBS is not limited to bremsstrahlung events and Compton and annihilation events can also produce multiple photons; however, to avoid production of charged particles, RR is played with low-weight photons before they can

undergo a Compton event and if successful, charged particles must survive an additional round of RR to be kept.

Both elimination procedures result in high weight or ‘fat’ particles being produced. If charged particles are of interest in dose deposition, as is the case normally, addition of electron splitting is required so that fat charged particles do not influence statistics downstream due to their high weight. To use electron splitting two planes are defined: a RR plane and an electron splitting plane. The RR plane specifies the plane below which RR conditions for charged particle elimination are relaxed—thus, below this plane, the number of charged particles increases. The electron splitting plane is positioned a few mm downstream of the RR plane and all fat charged particles passing through this plane are split and reassigned low weight. Electron splitting is only enabled in the FLATFILT component module, and BEAMnrc User Manual (Rogers, Walters et al. 2006) suggests that for optimum efficiency, the RR plane be placed a few mm above the downstream face, inside the flattening filter, and electron splitting occur on the downstream surface of this component module (Rogers, Walters et al. 2006). The splitting field radius (FS) for DBS should be about 10 cm greater than the maximum field size radius to be used at the specified distance from the source, (DBSSSD), i.e. if a 20 x20 cm² was the greatest field size used; this yields an effective field radius of approximately 10 cm and a 20 cm splitting field radius should be used. This is to avoid fat photons occurring in the field of interest.

Monte Carlo is considered the *de facto* standard in radiation dose calculation; however, its computationally intensive nature has to date prevented implementation of full Monte Carlo treatment planning. While standard computing power is continually increasing, use of distributed processing can greatly reduce calculation times. For this work a cluster of 8-17 PCs (3.4 GHz/ PC) was used with parallel processing controlled by the Sun Grid Engine (Sun Microsystems, Santa Clara, USA).

3.1.8 PEGS4

Preprocessor for EGS4 (PEGS4) data files contain interaction cross sections for broad lists of materials to facilitate radiation transport in EGSnrc. The two standard PEGS files used with BEAMnrc and DOSXYZnrc are 700icru.pegs4dat and 521icru.pegs4dat;

however, the pegs executable allows creation of cross section data for new materials (section 3.4.4).

3.1.9 Phase Spaces

Phase space files contain the x, y, and z position and direction, energy, charge, weighting and potentially latch number (denoting regions through which particles passed or in which they interacted) of all of the phase space particles. These particles result from the propagation of the requested number of incident particles through the accelerator geometry to the pre-defined phase space plane. Since typical phase spaces contain a few million particles, files on the order of gigabytes in size can be produced. Due to the statistical fluctuations in particle propagation, some uncertainty is inherent in the phase space file but is typically less than the statistical uncertainty associated with dose scoring simulations, i.e. section 3.1.1 (Walters, Kawrakow et al. 2002). It is fairly common when scoring dose that the requested number of incident particles exceeds the number of particles in the phase space and the phase space particles are recycled.

3.1.10 6 MV Beam Model

A Varian 2100EX linear accelerator in 6 MV mode was modeled using the EGSnrc/BEAMnrc Monte Carlo package (Rogers *et al.* 1995). The BEAMnrc model began with the electron beam at the level of the 6 MV target surface. The parallel circular beam source routine (ISOURC = 0) was used to model the incident electron beam as mono-energetic with a radius of 1.0 mm (Keall, Siebers et al. 2003). The incident electron energy for simulation was taken from the calibration curve relating the bending magnet current at the nominal energy for 6 MV (supplied as part of manufacturer specifications, confidential).

A series of component modules were selected to best correspond with the linac components and CM parameters were defined according to the dimensional and material specifications provided by the manufacturer (Varian Medical Incorporated). When accessing the linac carousel, to insert the low-Z targets, an additional 0.47 cm aluminum cover was found on the downstream face of the 6 MV flattening filter and was consequently added to the model.

The simulation of the linac head was separated into two steps. Initially, photon generation and propagation was simulated down to the level above the jaws CM and a phase space captured. This phase space was then used as a source to produce multiple field sizes with the jaws CM with progressively larger openings. The simulation was separated since time consuming electron transport occurs mainly in the target and flattening filtration and this enabled it to only be done once.

Initially 14 runs of 2×10^7 electrons were used to capture a phase space above the jaws using directional bremsstrahlung splitting (DBS) with a splitting field radius of 20 cm and splitting number of 1000. Electron splitting was turned on with the electron splitting and Russian Roulette planes placed as recommended in the BEAMnrc Users Manual (Rogers, Walters et al. 2006). Figure 3.3 shows the main inputs for the initial step of the 6 MV beam simulation. The pegs file 700icru and the PRESTA-II electron step algorithm were used for the 6 MV beam simulation.

Main Inputs	
1) Title	Top6MV
1) Medium	AIR700ICRU
1) WATCH Output	none
1) RNG Seed Options	store RNG at start of each batch
1) Run option	first time
1) Output Options	phase space at each scoring plane
1) Store Data Arrays	no
1) LATCH option	non-inherited latch
1) Score Last Z	no
1) Number of histories	20000000
1) Initial RNG seed 1	58
1) Initial RNG seed 2	74
1) Maximum CPU hours allowed	168
1) Bremsstrahlung Splitting	directional
1) Split electrons or photons at CM	none
1) Incident particle	electron
1) Source number	0 - Parallel beam from the front
1) Global electron cutoff energy - ECUT (MeV)	0.7
1) Global photon cutoff energy - PCUT (MeV)	0.01
1) Electron range rejection	off
1) Global electron cutoff (ESAVE GLOBAL, range rejection, MeV)	
1) Photon forcing	off
1) Number of scoring planes	1
1) Dose calculation	Only total dose
1) Z of front of 1st CM to reference plane (cm)	0.0

Buttons: Edit EGSnrc Parameters, Close

Figure 3.3 The main inputs for the first step of 6 MV beam simulation.

Unique random number seeds were used on each run to avoid potential correlations in pseudo-random sampling. The number of electrons simulated per run was 2×10^7 , yielding partial phase space file sizes around 1 GB, when the run was split into 16 jobs. The LINUX system used for BEAMnrc/EGSnrc is run on 32-bit CPUs, which limit the

maximum file size to $2^{32} - 1 = 2\text{GB}$ (Jaeger 2005). If the maximum file size is reached during a BEAMnrc simulation, the phase space will begin overwriting previously-generated histories. While this does not introduce error, since each particle is an independent history, it does not improve statistics. The batch size was chosen so that two jobs could be summed to produce a maximum size phase space for propagation through the jaws. In all, twenty-two 2 GB field-size independent phase spaces were generated and run sequentially through the jaws at multiple field sizes, ranging from $5 \times 5 \text{ cm}^2$ to $20 \times 20 \text{ cm}^2$, as specified at 100 cm source to surface distance (SSD). At this stage no splitting was used and the input number of particles set to the number of particles in the field-size independent phase space. For a given field size, the phase spaces captured at the exit of the linac head (below the Mylar window) were summed to the maximum file size, and resulted in between 1 and 7 phase spaces per field size, containing 30M to 480M particles (i.e., for $5 \times 5 \text{ cm}^2$ to $20 \times 20 \text{ cm}^2$ field sizes, respectively).

3.1.11 Experimental Beam Models

The experimental 6 MeV/Al configuration is readily replicated in BEAMnrc from the 6 MV beam model by replacing the standard target materials with air, the flattening filter module with a 1.0 cm slab of Al at the correct position and adding a 0.9 cm layer of polystyrene 0.5 cm below the Mylar window at the exit of the linac head, as shown in Part 1 of figure 3.1. The incident electron energy for the nominal 6 MeV mode of a Varian high energy linac was determined by Robar to be 7.0 MeV (Robar 2006). This was used as the modeled 6 MeV/Al incident energy. A phase space file was scored at the downstream surface of the polystyrene filter instead of the Mylar window. Typical phase spaces contained 150 M particles (i.e. 2 2GB files, for a $10 \times 10 \text{ cm}^2$ field.) SBS splitting was used instead of DBS due to uncertainty in the origin of the majority of charged particle contamination for electron splitting. 6 MeV/Al beam simulations were performed in a single step, scoring the phase space below the polystyrene filter. The computing power available had increased by this stage of the project and together with the absence of a flattening filter effectively eliminated the advantage of the two-step simulation. The pgs file 700icru and PRESTA-II electron transport algorithm were used for the low-Z

beam simulations. The lists of component modules used for the 6 MV and low-Z beams are defined in the beam spec module files, Appendix A.

3.1.12 BEAMdp

BEAMdp is a general purpose utility that facilitates analysis of BEAMnrc-generated phase space files. It produces a graphical output, using the GRACE plotting package and a text file. BEAMdp can extract a number of phase space characteristics including: spatial and spectral distributions, fluence and energy fluence distributions, as well as angular and mean energy distributions, all within user-defined field limits; also the ‘list parameters for a number of ph-sp particles’ option lists all phase space information for a number of particles as well as a summary of the total phase space particle and photon count which is useful when assigning the recycling number in DOSXYZnrc simulations, (section 3.2.2). The characteristics of the entire phase space population can be examined at once, or the electron and photon populations can be considered individually. BEAMdp can also combine two phase space files, which is useful when adding two files that are not sequential. Otherwise, combining two or more phase space files can be done in the terminal command line using the ‘addphsp’ command, (Rogers, Walters et al. 2006). BEAMdp was used to extract the radial electron distribution for three source planes to examine the effect of electron beam scattering in air, thus increasing effective focal spot size. Figure 3.4 shows calculated radial electron fluence at the downstream surface of the vacuum exit window, the new target location (0.9 cm air gap) and the previous target position (2.47 cm air gap) used by Robar (Robar 2006). The full width half maximum (FWHM) demonstrates that, in the new target position, the electron beam, although Gaussian in shape, has similar effective focal spot size to that at the exit window, while the previous target position increased the effective focal diameter by approximately 0.4 mm.

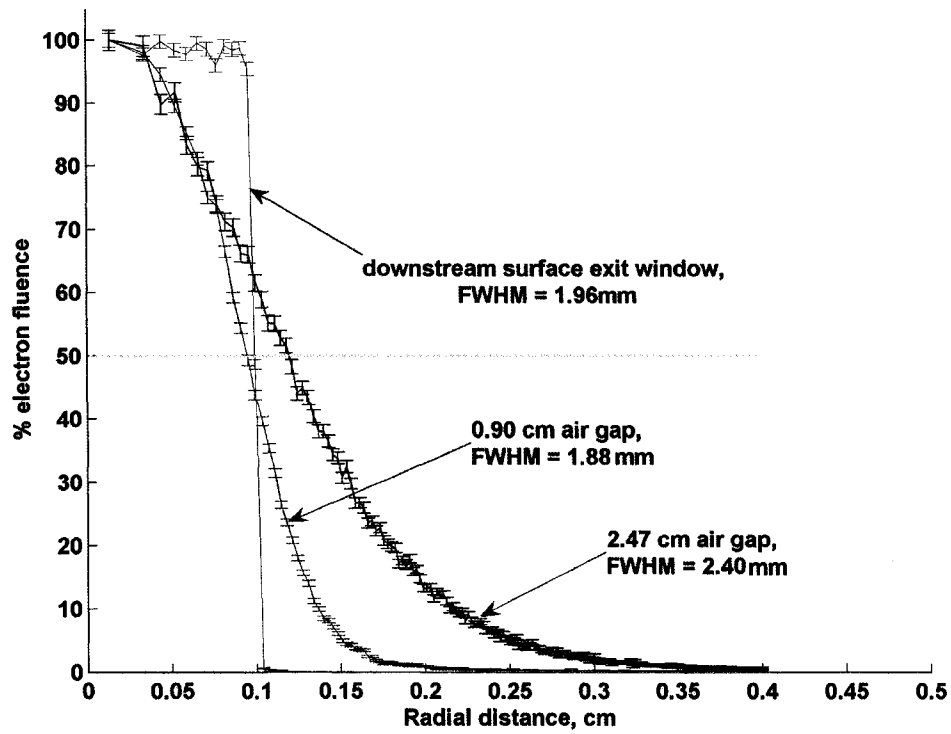


Figure 3.4 Monte Carlo calculated electron fluence versus radial position for three planes corresponding to the downstream surface of the Be vacuum window, the improved target position (0.9 cm air gap), and the old target position (2.47 cm air gap). FWHM = full width half maximum.

After each phase space was produced, BEAMdp was used to find the total particle number either for input into the phase space source routine or to determine the recycling number for DOSXYZnrc simulations (section 3.2.3)

Spectral distributions at the exit of the linac head for the 6 MV therapy beam versus low-Z beams were extracted using BEAMdp -these spectra provide insight into the potential effect on image contrast of the different beams, knowing that a larger fractional fluence at low energy should produce better contrast due to the Z dependence of photoelectric effect at these energies. The phase spaces for 10 x 10 cm² field size were used to produce photon-only spectra for each beam; the minimum and maximum X and Y dimensions set to +/- 5 cm with no latch selected. The spectra were produced with an energy range of 0.01 MeV (PCUT) to 7.0 MeV, the maximum potential energy, using 400 energy bins.

Table 3.1 provides a summary of the electron beam energy and target composition and thicknesses for which spectra were simulated.

Target thickness, cm	Target composition	Incident electron energy, MeV
*As listed in manufacturers' specifications	W/Cu	6.4 (6 MV mode)
1.0	Al	7.0 (6 MeV electron mode)
0.67	Al	4.5 (4 MeV electron mode)
1.5	Be	7.0 (6 MeV electron mode)
1.0	Be	4.5 (4 MeV electron mode)

Table 3.1 Target thickness and composition along with the incident electron energy for all beams modeled by Monte Carlo (MC). The first two beams were also produced experimentally to compare with their MC models.

In addition, the fluence versus position option in BEAMdp was used to extract radial profiles of the 6 MV and 6 MeV/Al beams. The 10 x 10 cm² field size phase spaces were propagated to 100 cm SSD in air. For the 6 MV beam the square field option was applied with +/- 7 cm limits, and 100 bins. For the 6 MeV/Al beam the rectangular field option was used and X (cross-plane) and Y (in-plane) fluence profiles evaluated separately within +/- 8 cm of central axis, with 100 bins.

Estimated real fluence and no latch were used for all BEAMdp actions.

3.1.13 Egswin

Egswin is another accessory program associated with BEAMnrc. It allows visualization of the input geometry and tracking of a sample of simulated particle tracks within the geometric limits of the model (Rogers, Walters et al. 2006).

Figure 3.5 shows an egswin output of the full 6 MV linac geometry alone (a) and with particle histories (b). Figure 3.6 shows the linac target and primary collimation region for 6 MV and the low-Z configuration.

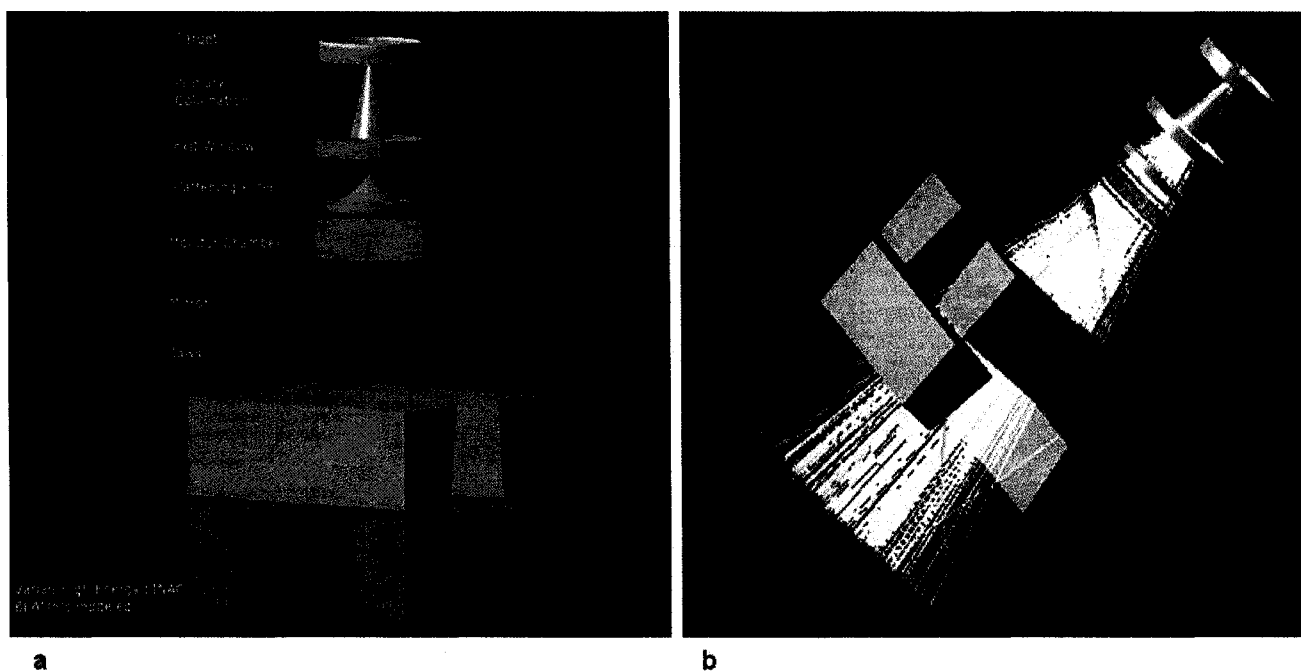


Figure 3.5 The egswin output for a Varian high energy linac model without (a) and with (b) particle history tracks. Photon tracks are shown in yellow, and electrons, in blue.

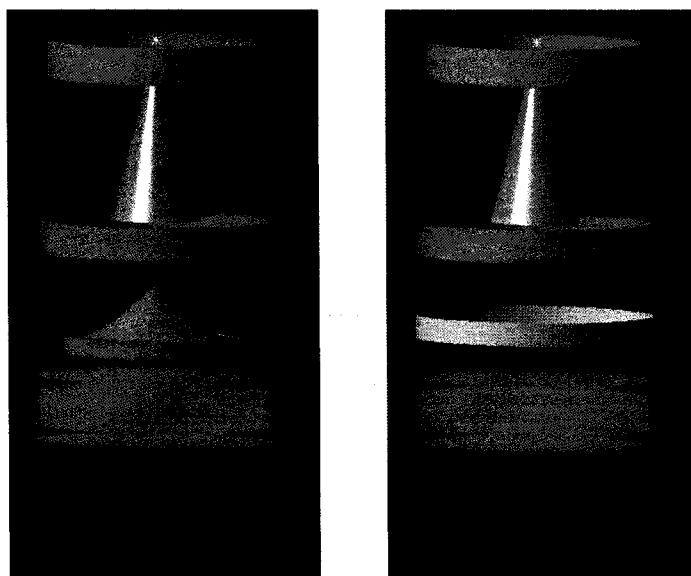


Figure 3.6 The initial components of the 6 MV (a) and 6 MeV/Al (b) linac heads, as output by EGS_windows. The target for the 6 MV beam is not shown, but is part of the first layer of primary collimation. The location of the incident electron beam is shown by the small yellow star at the entrance to the primary collimation.

3.2 6 MV Beam Validation

The standard method for validating Monte Carlo generated photon beam models is comparison of dose to water at multiple field sizes and depths (Rogers, Faddegon et al. 1995). The 6 MV beam model produced here was validated by comparison of calculated percent depth dose and radial dose profiles, scored in water using Monte Carlo DOSXYZnrc, with the same profiles measured by an ion chamber in water, for the clinical 6 MV therapy beam from the 2100EX.

3.2.1 Dose to Water with Ion Chamber Measurements

Profiles were measured in the clinic's 50 x 50 x 50 cm³ water tank with a waterproof RK ion chamber (Scandtronix, Uppsala, Sweden). The following paragraph outlines the procedure for these measurements.

The water reservoir was brought into the bunker 12 hours prior to measurement, allowing the water to come to equilibrium at room temperature. At the time of measurement, the water tank was positioned under the linac head and the amplifier box connected to the control box on the side of the water tank. The connection was fed through the conduit and, via a USB converter, to the laptop outside. The waterproof ion chamber was placed in the holder of the water tank's translation system. The chamber was oriented with the small white dot, denoting its center, facing upwards towards the linac head and no buildup cap was used. An additional RK chamber was attached to the linac accessory mount to serve as a reference chamber, correcting measurements for the short term variations in beam output. The reference chamber was positioned with its tip inside the smallest field to be measured along a diagonal from the corner of the field towards the center, ensuring that it did not obstruct measurement along the principle axes, as in figure 3.7. Both ion chambers were connected to the control box on the side of the water tank.

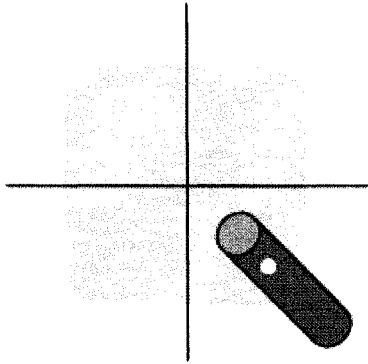


Figure 3.7 Location of the reference ion chamber relative to smallest field and principle in-plane and cross-plane axes, during water tank setup.

The tank was then filled from the reservoir, ensuring that all valves were open when turning on the pump motor. The tank was filled to approximately 2/3 full, aligned in the in-plane dimension and leveled using a precision level on the tank walls, ensuring motion of the detector chamber was accurately parallel/perpendicular to the water surface. The hydraulic lift in the water tank stand was used to align the water surface with the wall lasers (at 100 cm SSD). The zero depth was set by positioning the detector chamber half-in, half-out of the water.

The Omnipro software package (Scandtronix/Wellhofer, Uppsala, Sweden) was used to control the translation system, to collect reading from the ion chambers and to apply corrections. Both ion chambers were set to a -300 volt bias and the gain adjusted using the AUTO GAIN function, running a steady beam and moving the detector chamber to the d_{\max} to maximize signal. A background measurement was then taken for calibration and the detector moved, under video supervision, to the maximum measured depth, ensuring it did not collide with the bottom of the tank. Dose rate mode was used with 10 samples and no offsets. The speed was set to medium for all scans and step size was 3 mm for PDDs and 5 mm for radial profiles, with the exception of within ± 15 mm of the field edge where step size was 1 mm. All scans can be setup prior to measurement by using ADD. Profiles were renormalized and shifted towards the surface of the tank by $0.6 \times$ the ion chamber radius in Omnipro before being exported as text files. The profile shift accounts for the effective point of measurement of the ionization chamber (Almond, Biggs et al. 1999).

3.2.2 Dose to Water with Dosxyznrc

DOSXYZnrc is another EGSnrc user code whose purpose is to facilitate evaluation of dose distributions in a three-dimensional Cartesian geometry. A three-dimensional space is divided up into volume elements, or voxels, and composition and density assigned to each voxel. DOSXYZnrc can also import a CT data set and will assign composition based on Hounsfield units (HU) to allow calculation of patient dose distributions. DOSXYZnrc uses global electron and photon cutoff energies, ECUT and PCUT, whose recommended values are dependent on the simulation; however the conservative default estimates for these parameters are the same as those in BEAMnrc (section 3.1.3). The maximum number of histories DOSXYZnrc can run in a single simulation is 999,999,999. Since the maximum phase space size is about 76 M, particles from this phase space will need to be recycled 14 times if the maximum history number is used in DOSXYZnrc.

3.2.3 Phase Space Recycling

Often, scoring dose in DOSXYZ models requires greater incident history number than the number of particles in the phase space being used, in order to obtain acceptable statistical uncertainty, (Rogers, Faddegon et al. 1995). For this purpose, it is possible to recycle phase space particles.

Variance reduction techniques, such as bremsstrahlung splitting, introduce correlations between phase space particles. Recycling these particles transfers this correlation to the DOSXYZ simulation. While this can be problematic for electrons, especially at the surface of materials where there is a large chance of the same phase space particle interacting in the same voxel twice; for photons, recycling has little effect since chances of the same phase space photon interacting in the same voxel is relatively small, except when recycled many times (Walters, Kawrakow et al. 2002). Recycling photons 27 times was shown by Walters *et al* (Walters, Kawrakow et al. 2002) to increase uncertainty by only 0.4%, versus a factor of 5 increase for recycling electrons an equal number of times. Photon recycling 60 times shows increased fractional uncertainty of 1.2%.

3.2.4 Geometry and Scoring Dose

In DOSXYZnrc, voxel size is entered for each dimension, either as voxel groups or individually. It is useful to minimize the number of extraneous voxels to increase efficiency, (e.g., if calculating a PDD on central axis, all of the volume surrounding the central column can be grouped into a few large voxels). Voxel dimensions can be decreased to achieve more fine spatial resolution; however, by decreasing voxel size, the number of histories required to achieve acceptable statistics increases. It is therefore useful to have an idea of the three dimensional spatial variation in dose and to set voxel size accordingly.

3.2.5 Analysis of Scored Dose

The program statdose can be used to extract profiles from DOSXYZnrc's 3ddose files. The maximum array size for statdose is 128 x 128 x 150 but a new version was compiled that increased this to 325 x 325 x 150 (statdose_new). The profiles selected in statdose are plotted using the GRACE plotting package and an output file with the extension .xvgr is produced. The .xvgr file have a header and 3 columns containing: the voxel coordinates, values and uncertainties. Initially statdose was used to produce xvgr files that were then read into MATLAB for further analysis and comparison to measured data; however, when it became necessary to combine multiple 3ddose files, a MATLAB m-file was written to read in 3ddose files directly.

The DOSXYZnrc Users Manual explains the 3ddose file format (Walters, Kawrakow et al. 2006) and the MATLAB code used to read and add 3ddose files is given in Appendix B.

3.2.6 MC Dose to Water

For the purposes of validation, in DOSXYZnrc, a 30 x 30 x 30 cm³ water block was subdivided into voxels whose dimensions were assigned according to the expected dose gradient, ranging from a minimum of 2 mm at field edges and in the PDD buildup region to 5 mm in low gradient regions. The voxel dimension orthogonal to the axis of interest was set to 1 cm since dose was considered relatively uniform over this region and increasing the voxel volume reduces the required number of histories. The phase space

particles were recycled 14-28 times to achieve uncertainty on the order of +/- 1%. The 700icru pegs file was used and 3ddose files exported to MATLAB where they were read, summed and linearly interpolated for comparison to measured data.

3.3 aS500 Detector Model Validation

3.3.1 aS500 Detector

Varian's aS500 is an amorphous silicon (a-Si) electronic portal imaging detector (EPID). a-Si EPIDs are the present standard in high resolution megavoltage imaging in radiation therapy. The three main functional layers of the detector are (Part 3, figure 3.1).

- A copper buildup layer, to improve detection efficiency of MV beams through generation of Compton recoil electrons;
- A Kodak Lanex Fast Back phosphor screen composed of $\text{Gd}_2\text{O}_2\text{S:Tb}$, which converts high energy radiation into visible light; and
- An a-Si diode array on a glass substrate, with pixel pitch 0.078 cm x 0.078 cm.

3.3.2 6 MV Open Field Imaging

Images were acquired using the Varian image acquisition software AM Maintenance (Varian Medical Incorporated). The Service Monitor mode was used with the 6 MV/ 300 MU/min IMRT mode for 6 MV imaging. 50 MU were delivered per image at a dose rate of 300 MU/min, with the frames averages set to 9996 – the number denoting continual charge integration. Image acquisition was terminated by allowing the MUs to expire. Figure 3.8 shows the parameters used during image capture. For calibration, the number of frame averages for the dark field was set to 60, and during flood field, set to 30 with a large number of MUs. These frames average values were taken from the calibration procedure used for clinical imaging modes.

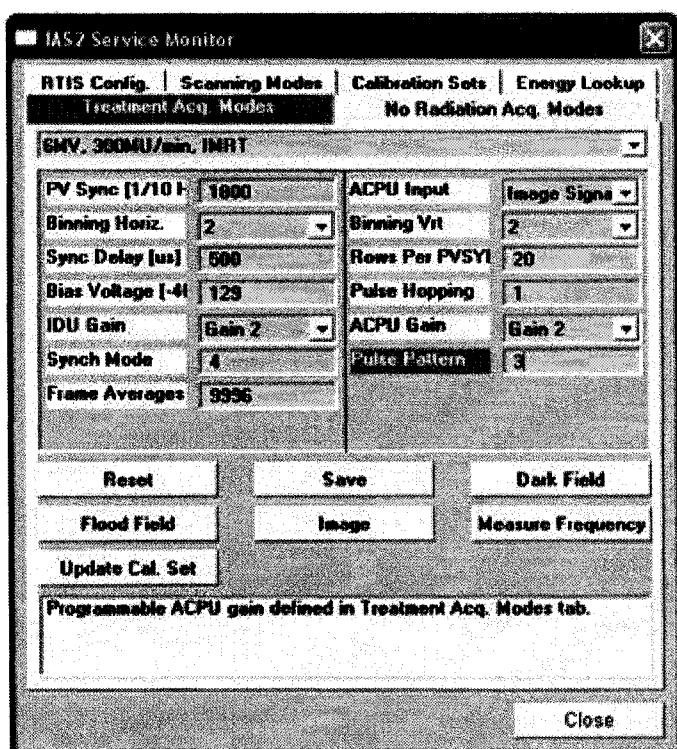


Figure 3.8 AM Maintenance imaging parameters for 6 MV.

3.3.3 Detector Calibration

Using the Varian image acquisition software, detector calibration includes uniformity and dark-current correction across the diode array. Siebers *et al* (2004) encountered a challenge during image calibration because the calibration software divides raw images by a flood-field image, whereby the flood field image is simply the image generated by an open beam irradiating the full panel. This process removes inherent and expected non-uniformity in imaged open beams, including for example, the beam horns. In contrast, these details will be present in the present in the MC scored dose profiles. To remedy this, a flood-field can be created that is truly uniform such that this correction will preserve the true beam profile, while still including all detector element gain corrections. In an approach similar to that taken by Siebers *et al* (2004) during flood field capture, we used an extended source to imager distance (SID = 180 cm) and introduced scattering material (20 cm Solid Water at 90 cm SSD and 1.5 cm Solid Water on the imager surface) to achieve a uniform flood field. Film measurement was used to confirm

the uniformity of the flood field and showed 7.6% flatness across the full detector and 3.5% across the detector's central 20 x 20 cm² region.

3.3.4 Solid Water

Tissue mimicking substances are normally composite plastic solids whose absorption and scattering properties are designed to radiologically match the tissues in the body for a given energy range. Their main use is in quality assurance phantoms for imaging and dose evaluation. Although not directly tissue mimicking, Solid Water is by far the most used surrogate partly due to the fact that most radiation dose calibration and commissioning protocols are in terms of dose to water, (i.e. TG-51, (Almond, Biggs et al. 1999)), and partly since water is considered, dosimetrically, a fairly close match to soft tissue, (Attix 2004). The Solid Water (Gammex, Inc. WI, USA) used in this work has a linear attenuation coefficient relative to pure water is 1.030 +/- 0.01 for photon energies from 100 kV to 24 MV.

3.3.5 Film Measurements

Large format Kodak EDR2 extended dose range radiographic film (Kodak, Carestream Health Inc., NY, USA) was used to verify flood field flatness. The film was calibrated using an in-house MATLAB program which creates a look-up table (LUT) of optical density versus dose, using low (30MU), medium (100MU) and high (300MU) dose films exposed down the central axis for a 5 x 5 cm² field size in water. The calibration films were taken using a Solid Water film cassette. The film was positioned inside the cassette with its edge aligned flush to the opening of the cassette. The cassette seal was tightened and sealed with electrical tape. This was performed in a dark room to prevent film exposure. The cassette was placed at the center of a 30 x 30 x 30 cm³ block of Solid Water, and the linac gantry rotated to face the taped side of the cassette. The film was aligned with central axis and the surface of the Solid water was set to 100 cm SSD. The set number of MU was delivered and the film extracted from the cassette in the dark room. The film processor auto-replenish function was turned off to avoid variation in chemistry during a single processing session. This was repeated for the two remaining dose levels.

The flood field film was exposed with the modified calibration setup, placing the film between the 1.0 cm and 0.5 cm layers of Solid water on the detector surface and delivering 200 MU. Once developed, the film was digitized using a VXR-12 plus film digitizer (VIDAR Systems Corporation, Herndon VA) with 74 pixels per inch, 12-bit depth producing non-lossy tif files. The PDD tif files are read into MATLAB and IMRT film calibration program, IMRTdosim, used to produce a LUT. From this the flood field film was calibrated. The following steps are performed in MATLAB code to determine the flatness of the film.

Using marks made in one corner of the film prior to development, the film orientation during exposure is determined and spatial axes are created. The exposed area of the film is selected with a margin and the image boundaries found by first taking profiles along the cross-plane and in-planes axes, midway across the selected image area. The gradient of these profiles was then computed and to give a well defined maximum and minimum peak at the image boundaries, where exposure rises and falls off rapidly in the profiles. The location of central axis is then taken as the center of the exposed field. This assumes the field is not significantly rotated relative to the edge of the film and that central axis (CAX) is actually in the center of the field. The flood field image was cropped to 80% of the field size and since we know that the radiation field should not vary sharply on a sub mm basis, outliers removed with the following process: if a pixel value fell outside 5% of the mean pixel value of its next-but-two corner neighbors, (i.e. for pixel (i,j) , the mean of neighbors $(i\pm 3, j\pm 3)$), the pixel value was replaced by the mean. Directly neighboring pixels were not used since groups of 2-3 outlying pixels occurred. The 5% threshold was varied to ensure that large regions of the field were not being averaged. Flatness was then evaluated over the central 80% of the field (Khan 2003).

3.3.6 aS500 Model

A highly detailed MC model of Varian's aS500 a-Si EPID was created in DOSXYZnrc by Siebers *et al* (2004) for the purpose of validating portal dosimetry use in IMRT plan verification. The 26 layer model includes all structural and detector components, with material thicknesses specified to a fraction of a millimeter; the only approximation made is substitution of a 1 cm equivalent backscatter layer at the downstream end of the imager

accounting for the back cover and mounting bracket. The model was obtained from Siebers *et al* following the signing of a non-disclosure agreement with Varian (Varian Medical Incorporated). A peps4dat file containing cross sections and compositions for the 16 materials in the detector was also supplied by Siebers *et al* (Siebers, Kim et al. 2004), EPIDdata.pegs4dat.

By scoring dose in the phosphor layer, MC-simulated portal images can be generated. Munro and Bouius (1998) have shown that 99.5% of the detector response originates from dose to the phosphor screen and Siebers *et al* (2004) used 6 MV open field profiles scored in the phosphor screen versus measured images to validate their model, finding that they could reproduce measured image profiles within +/- 1% for all points with the exception of the area where the support arm bracket and electronics produce non-homogeneous backscatter. This group also demonstrated the accuracy of the model by predicting the plan verification image for a large IMRT patient field, and found 99.7% of points had a gamma (Low and Dempsey 2003) less than 1 for the 2% / 2 mm gamma-analysis criteria compared to standard film-method verification, yielding 99.2% points under the same criteria.

All MC simulated images in this study are scored as dose to the phosphor screen layer of the detector; 6 MV open field profiles were scored in the detector, using beam phase space files validated in the previous step. The SID of the detector was set to 130 cm. Dose was scored along the in-plane (y) and cross-plane (x) dimensions, corresponding to axes parallel and perpendicular to the linac waveguide, respectively. 1 mm x 5 mm voxels were used, to obtain adequate positional precision along the dimension of the profile (1 mm) and to cover enough area to reduce the number of histories required to achieve acceptable statistical uncertainty.

3.3.7 Latent Phase Space Variance

The statistical fluctuation in phase space files has been termed “latent phase-space variance” by Sempau *et al* (Sempau, Sanchez-Reyes et al. 2001). This latent variance can be compared to the uncertainty in dose calculation due to the random nature of particle transport in the phantom. In general, uncertainty in dose calculation is far greater than latent phase space variance; however, phantom particle transport error will approach zero

if a sufficient number of histories is run, with only the latent phase-space variance remaining. When calculating open field profiles for detector model validation, the original phase space files were recycled 115 times at which point the latent phase space variance was observed: increasing the recycling number would no longer reduce the uncertainty in dose. As a result the number of particles in the phase space was increased and further reduction in uncertainty was observed.

3.3.8 Validation

Monte Carlo generated open field profiles for field sizes from $5 \times 5 \text{ cm}^2$ to $15 \times 15 \text{ cm}^2$ were plotted with measured image profiles calibrated using the corrected method for flood field capture. The profiles were compared within their combined uncertainty and $\pm 2 \text{ mm}$ for high gradient regions.

3.4 Quantifying and Validating Contrast

3.4.1 Simple 6 MV Contrast Evaluation

Before introducing the QC3 model, the contrast of a 5 cm block of solid water covering half of a $15 \times 15 \text{ cm}^2$ field was evaluated for the 6 MV beam. In BEAMnrc, the $15 \times 15 \text{ cm}^2$ 6 MV phase space was propagated down to 100 cm SSD, where an additional component module was introduced to model a 5 cm block of water covering half of the field. A phase space was scored below the water block and then directed onto the detector model to score dose in DOSXYZnrc. The same setup was used for measured images and MATLAB code was written to evaluate contrast by taking symmetric sample areas under the water and in the open beam section of the field, on the detector.

3.4.2 QC3 MV Imaging Phantom

The MV QC3 imaging phantom (Rajapakshe, Radcliffe et al. 1993) was used to quantify image contrast. The phantom includes 6 contrast regions composed of polyvinyl-chloride (PVC), aluminum or lead. The remaining thickness of all regions $< 1.5 \text{ cm}$ is filled with PVC. Each region is $2.0 \times 2.8 \text{ cm}^2$ and is encased by the front and back covers which have uniform composition. The composition of the contrast regions (Rajapakshe, Radcliffe et al. 1993) are shown in figure 3.9.

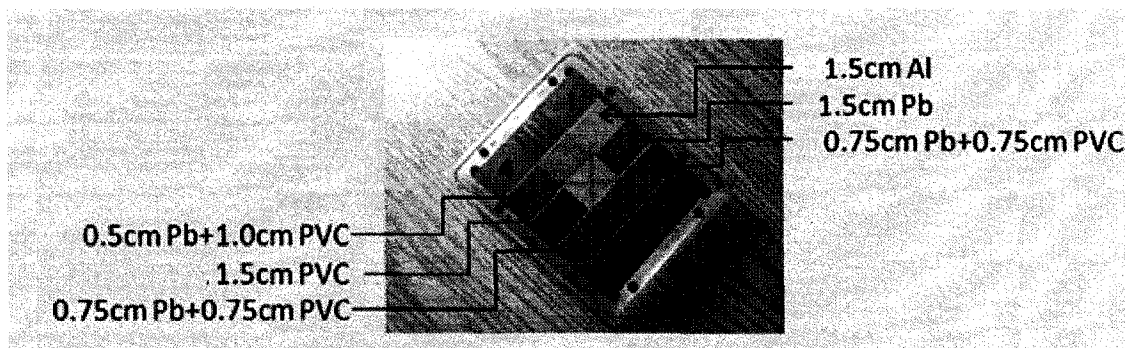


Figure 3.9 The QC3 MV imaging phantom with labels indicating contrast region composition.

The QC3 was positioned as in Part 2 of figure 3.1, with the front surface at approximately 99.1 cm SSD, rotated by 45 degrees in the axial plane relative to the imager. A 10 x 10 cm² field size was used, with an SID of 130 cm. The Service Monitor in AM Maintenance was used with the 6 MV/ 600 MU/min IMRT mode, with calibration frames averages equal to those at 6 MV. 50 MU were delivered per image at a dose rate of 600 MU/min with the frames averages set to 9996 – the number denoting continual charge integration. Image acquisition was terminated by allowing the MUs to expire. Figure 3.10 shows the parameters used in the 6 MV/ 600 MU/min IMRT mode.

IAS2 Service Monitor

RTIS Config | **Scanning Modes** | Calibration Sets | Energy Lookup

Treatment Acq. Modes | No Radiation Acq. Modes

6MV, 600MU/min, IMRT

PV Sync [1/10]	1800	ACPU Input	Image Signal
Binning Horiz.	2	Binning Vrt	2
Sync Delay [us]	350	Rows Per PVSyl	1
Bias Voltage [-4]	129	Pulse Hopping	1
IDU Gain	Gain 2	ACPU Gain	Gain 4
Synch Mode	12	Pulse Pattern	1
Frame Averages	9996		

Reset Save Dark Field

Flood Field Image Measure Frequency

Update Cal. Set

Frequency generated by the trigger board based on therapy machine pulses. Used for row synchronization.

Close

Figure 3.10 AM Maintenance imaging parameters for 6 MeV/Al.

3.4.3 QC3 Contrast Model in DOSXYZnrc

The QC3 phantom was integrated into the DOSXYZnrc model of the aS500 detector by adding additional layers above the panel, along with a layer modeling the phantom-detector air gap. Simulated imaging was achieved by propagating BEAMnrc-generated phase space through the phantom and detector in one step. In the dimensions perpendicular to the beam axis, the voxel boundaries in the QC3 phantom were dictated by the pixel pitch of the detector below. Thus, compared to the actual phantom, contrast regions were defined within 0.078 cm and 0.156 cm of their dimensions in the in-plane and cross-plane dimensions, respectively. The QC3 model of the detector was aligned to be square with the detector, in contrast to its orientation at 45 degrees to the detector orientation in measured images. This choice was made to simplify the inputs in

DOSXYZnrc and is based on the fact that radial beam profiles are symmetric about CAX. The QC3 contrast regions contain PVC, a material not in the standard PEGS 700ICRU or 521ICRU datasets. The atomic composition and density of PVC was taken from Attix (2004) and interaction data for this material was generated using the PEGS.exe utility. Once the cross section data is produced it can be appended to any other peps data file. The peps input file for PVC is shown in Appendix C.

Measured images of the QC3 were acquired and corresponding simulated images were generated with the full MC imaging system model (linac head, QC3 phantom and aS500 detector, figure 3.1) for both the standard 6 MV therapy mode and for the experimental beam generated by 6 MeV electrons incident upon the 1.0 cm Al target. Figure 3.11 shows a measured image and a calculated virtual image of the QC3, using the 6 MV beam.

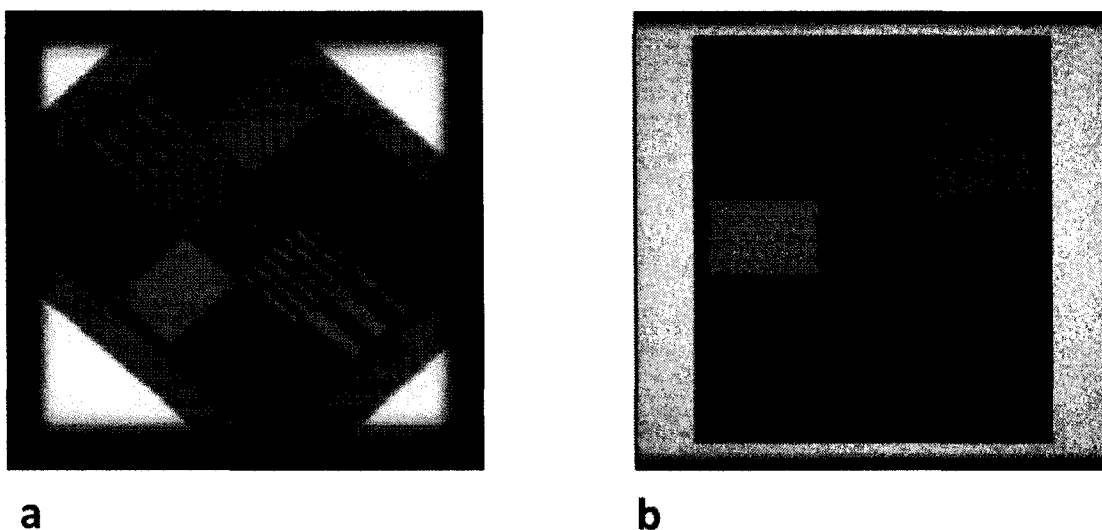


Figure 3.11 Measured (a) and calculated (b) images of the QC3 contrast phantom using the aS500 detector. Images have been leveled at the mean of the 1.5 cm Al region, and window width selected to encompass the full range of both images.

3.4.4 Effect of Field Size on Contrast

Initially, QC3 images were measured and calculated using a 32 x 24 cm² field size that resulted in full coverage of the imaging panel at SID 130 cm for both 6 MV and 6 MeV/Al beams. Poor agreement between measured and calculated absolute contrast was observed with the 6 MeV/Al beam. Subsequently, the field size was systematically varied

to study the effect on contrast. Both measured and modeling contrast for both beams at 15 x 15 cm² and 10 x 10 cm² field sizes was evaluated.

3.5 The Effect of Further Image System Alterations on Contrast

Once the MC imaging system model has been validated, it can be used to predict the effect of altering parameters that may further improve contrast from the experimental low-Z beams. Three main parameters have been investigated: lowering incident electron energy to 4 MeV, removing the detector's copper buildup layer, and reducing target Z from Al (Z = 13) to beryllium, Be (Z = 4) at 4 MeV.

3.5.1 Incident Electron Energy

With comparison of MC simulation and measurement Robar (2006) showed that the incident electron energy for the nominal 4 MeV electron mode is 4.5 MeV for the same high energy Varian linac used in this study. Additional phase space files were generated and dose scored with the incident electron energy set to this value, and the target thickness reduced to 0.67 cm (4 MeV/Al) as used previously (Robar 2006).

3.5.2 Copper Buildup Layer of Detector

The Cu layer of the detector was replaced with air and contrast was reevaluated as described above for both 6 MeV/Al and 4 MeV/Al.

3.5.3 Target Atomic Number

For the modeled 4 MeV electron beam, the Al target was replaced with a 1.0 cm slab of Be. Additional phase space files were generated and contrast reevaluated. The combination of this lower beam energy and lower-Z target material should yield the highest contrast ratio investigated in this work (Flampouri, Evans et al. 2002).

3.6 The Effect of Separation on Contrast

After quantifying superior contrast relative to the standard therapy beam (section 4.4), we were interested in measuring a possible loss of this advantage due to beam hardening, for a more realistic phantom geometry. A Solid Water (Gammex, Inc. WI, USA) phantom

containing a 1 cm-thick synthetic Cortical Bone (Gammex 450) insert was used, such that the bone region covered one half of the area of the detector panel during imaging. The total thickness of the phantom was varied from 1 cm to 16 cm while maintaining a constant distance of 100 cm from the source to the top of the bone region, figure 3.12. Images were taken using both the standard 6 MV beam and the experimental 6 MeV/Al beam. A $15 \times 15 \text{ cm}^2$ field size was used and SID was fixed at 130 cm. Three images were taken to evaluate standard deviation, and MATLAB code was generated to select symmetric sample areas from which the mean values were used to compute contrast.

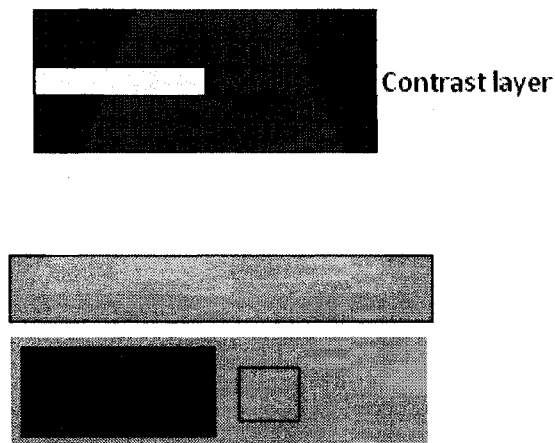


Figure 3.12 Experimental setup for measuring contrast versus separation. Symmetric layers of Solid Water were added to increase separation, while the contrast layer was held at a constant distance from the source and from the detector.

CHAPTER 4 Results and Discussion

4.1 6 MV and Experimental Low-Z Beams

Monte Carlo calculated spectra are shown in figure 4.1 for a standard 6 MV therapy beam, and 6 MeV and 4 MeV electron modes with Al and Be targets of thickness approximately 60% of the respective CSDA range of the energy and material. The fractional fluence between 25keV and 150keV is noted. The upper bound of this range was chosen as the energy limit considered to be diagnostic while the lower bound comes from the results of Ostapiak *et al* (1998) who show that attenuation of Be, C and Al target beams by 10 cm of water results in full attenuation of *all* photons below 25 keV. The majority of patient separations for MV imaging applications represent a minimum of 10 cm water-equivalent separation. Figure 4.1 shows peak fluence shifting from approximately 500 keV with 6 MV, having only 0.3% photons in the 25-150keV range, to a peak at 50 keV for 6 MeV on Al, 40 keV for 4 MeV/Al and approximately 20 keV peak for the beams from the Be targets. The fractional fluence between 25 keV and 150 keV increases with decreasing electron energy for the Al and Be targets, from 31.4% at 6 MeV/Al to 47.6% at 4 MeV/Be. At 6 MeV, the fractional fluence from the Be target is greater than that of the Al target by approximately 10% in the above-noted range, while at 4 MeV this difference is slightly less, 7.6%. Tsechanski *et al* (1998) report that the spectrum produced by 4 MeV electrons on Be has greater fractional fluence below 30keV, compared to beams from Al targets, while the fractional fluence between 25keV and 150keV is comparable to 4 MeV on Al. Both electron energies on Be targets have approximately 40% of their population below 25keV; this very low energy range is most susceptible to selective attenuation at increasing separation, and will potentially contribute to patient dose but not image contrast.

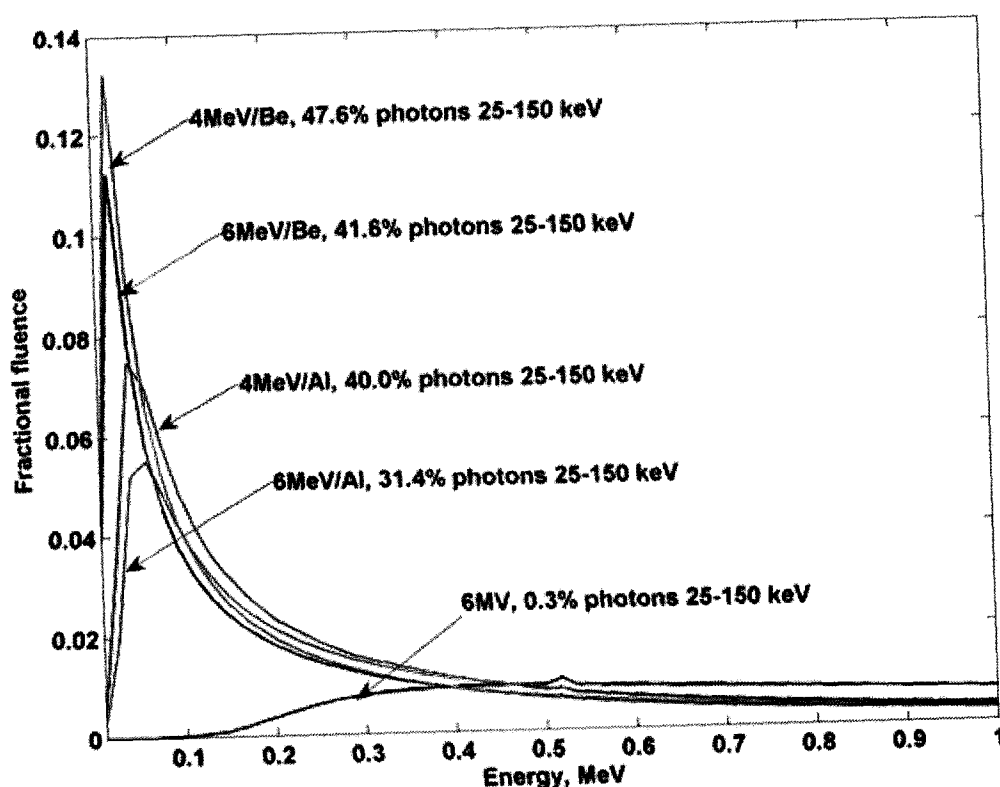


Figure 4.1 Calculated photon spectra for a standard 6 MV therapy beam, 6 MeV/Al, 4 MeV/Al, 6 MeV/Be and 4 MeV/Be beams. Spectra are captured as they exit the accelerator head, for experimental beams this is below the 0.9 cm thick polystyrene electron filter. Each spectral distribution was normalized by its own area.

Figure 4.2 shows the Monte Carlo calculated fluence profiles across the central 16 cm of the 6 MeV/Al and 6 MV beams, of field size $10 \times 10 \text{ cm}^2$, at 100 cm downstream of the electron source from a phase space scored in air. The forward nature of bremsstrahlung at 6 MeV results in a forward peaked beam and, for the low-Z beam, there is no flattening filter to correct this. The resulting fluence is 8% greater at central axis than 3 cm off axis, and 11% greater than 3.5 cm off-axis for 6 MeV/Al. Ostapiak *et al* (1998) measured forward peaked low-Z beams, for nominally 6 MeV electrons on C and Be targets of thickness approximately 1.5 times their corresponding CSDA range, using an ion chamber in water. Ostapiak's results indicate a similar drop in fluence of approximately 10% at 3 cm from central axis. Tsechanski (Tsechanski A 1998) notes that, since the low-Z targets are located below the standard target position, field magnification will result,

along with an increased penumbra since the beam line is no longer tangential to the collimating jaws. Comparison of the 6 MeV/Al beam profile with 6 MV in figure 4.2 demonstrates both of these features and shows a rectangular field for 6 MeV/Al due to the fact that the Y (in-plane) collimating jaws are positioned above the X (cross-plane) jaws and jaw geometry has not been adjusted to account for the altered source position.

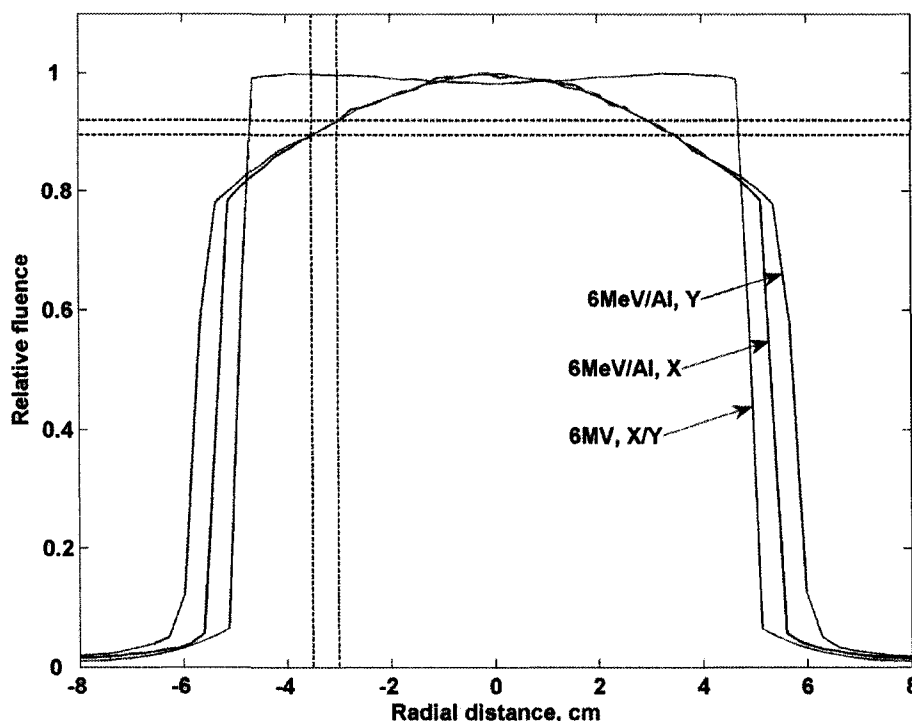


Figure 4.2 Calculated radial fluence profiles for the 6 MeV/Al and 6 MV beams, in air at 100 cm downstream of the electron source. The dotted lines mark -3.0 cm and -3.5 cm off axis, and the corresponding relative fluence, 0.92 and 0.89 respectively.

Contrast is generated by the difference in attenuation of incident fluence between two regions. If the incident fluence itself is non-uniform initially, decreasing with radial distance then the contrast detected between regions at different radial distances will be affected.

4.2 6 MV Beam Validation

PDD curves for field sizes from $5 \times 5 \text{ cm}^2$ to $20 \times 20 \text{ cm}^2$ were calculated using MC by scoring dose in a 1 cm^2 column along CAX, with voxels ranging from 2 mm in the

buildup region to 2.5 cm along the z-dimension, to a maximum depth of 30 cm. The average uncertainty in calculated dose was $\pm 1\%$. Ion chamber measurements in water for equivalent field sizes had an average uncertainty of $<1\%$ and comparison of the two methods showed 97% of points agreed within the combined uncertainty or 2 mm in high gradient regions. Radial profiles were calculated for corresponding field sizes and evaluated at depths of 1.5, 5, 7, 10, 15 and 20 cm, using 2 mm voxels perpendicular to the beam axis. The voxel dimension perpendicular to the profile was set to 1 cm. Comparison to equivalent ion chamber measurements also show agreement within the combined uncertainty for 96% of points or 2 mm in high gradient regions. To compare calculated profiles to measured, the calculated data was linearly interpolated at the location of measurements using nearest neighbor interpolation in MATLAB. Results of beam validation for $5 \times 5 \text{ cm}^2$ and $20 \times 20 \text{ cm}^2$ fields are shown in figure 4.3. The uncertainty in the field size produced during measurement is $\pm 2 \text{ mm}$, equal to the quality assurance (QA) tolerance which is checked daily for $10 \times 10 \text{ cm}^2$ and monthly for $20 \times 20 \text{ cm}^2$ field sizes. The calculated radial profile penumbra all fall within the 2 mm tolerance set for measured jaw position QA; however, ion chamber measurements were slightly lower than calculated values just inside the field and slightly higher just outside the field, indicative of a volume averaging effect.

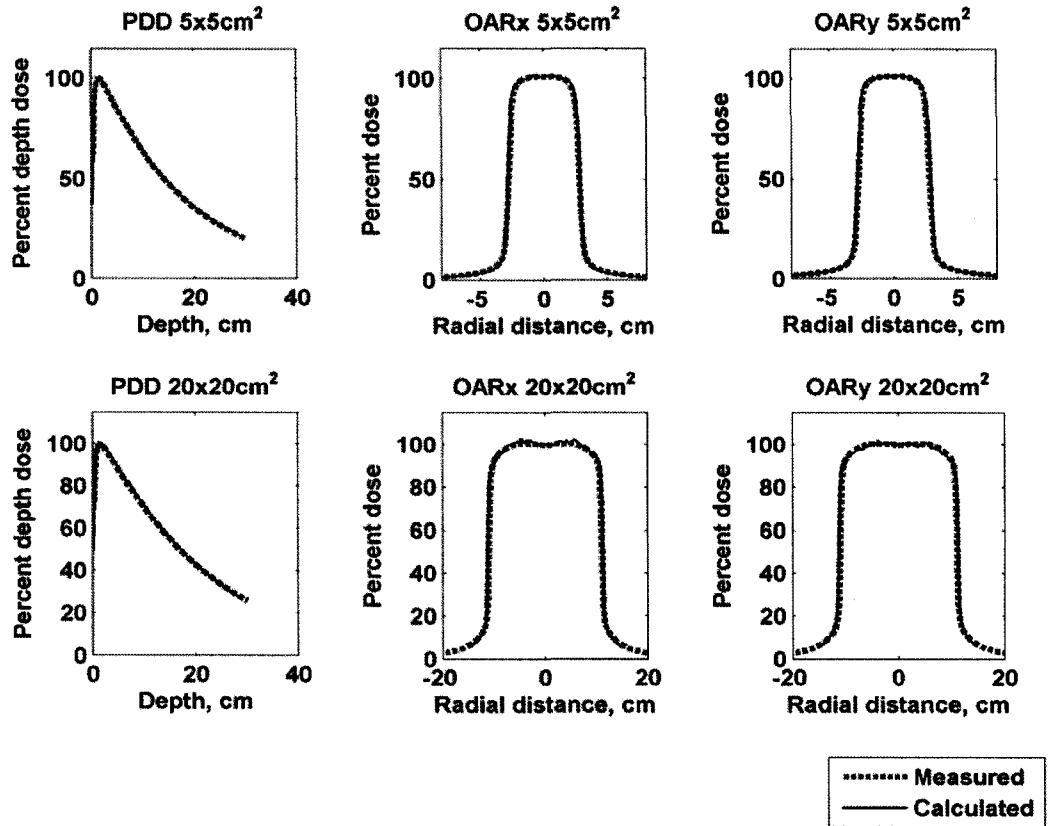


Figure 4.3 Depth dose and radial profiles for $5 \times 5 \text{ cm}^2$ and $20 \times 20 \text{ cm}^2$ fields for the 6 MV beam, comparing ion chamber (Measured) with Monte Carlo (Calculated). Radial profiles are taken at 10 cm depth.

4.3 aS500 Detector Model Validation

Figure 4.4 shows open field profiles from the detector at an SID of 130 cm, comparing measured and MC calculated images. As field size increases, the characteristic beam horns are visible. Profiles were normalized by rescaling the average value over the central 3 cm of the field to 100%. Each 5 neighboring pixels were averaged in the calculated data in order to smooth statistical noise, facilitating comparison to the measured profiles. 98% of calculated points agree with measured to within their combined uncertainty or ± 2 mm, within the field and at the field edges. The average measured and calculated uncertainties were 1 % and 2%, respectively. Outside the field, a discrepancy is seen where measured data exceeds that calculated. The magnitude of the discrepancy increases with field size; 5 mm outside the field edge of the $5 \times 5 \text{ cm}^2$ field the measured signal is

3.2% greater than that calculated, while 5mm outside the 20 x 20 cm² field this difference is 5.0%. There are a number of potential causes for this disagreement including: falloff of the flood field calibration image at the detector periphery, lack of lateral scatter equilibrium since the detector model extended only 2.5 cm beyond the imaging panel and failure in detector gain correction for low energy scatter present in these regions.

To look at the potential effect of non-uniform irradiation during flood field image capture the film-measured field flatness was examined. The total active area of the detector panel is 40 x 30 cm². Within the central 20 x 20 cm² (radius of +/- 10 cm) of the detector, the film-measured field flatness is 3.5 %; however, outside this range, dose falls off more rapidly, giving 8% flatness over the central 32 x 24 cm² of the detector. Flatness is defined as:

$$\text{Flatness} = (D_{\max} - D_{\min}) / (D_{\max} + D_{\min}) \quad \text{in the central 80\% of field, (Khan 2003)}$$

A reduction in the flood field signal towards the edges of the panel, relative to the panel center, results from using a field size equal to the extent of the panel; the penumbra region encroaches on the edges of the detector. Setting this field size is necessary to avoid irradiation of panel electronics. The result of a flood field with lower signal at the field edges manifests as amplification of the calibrated measured image in this region. This cannot be the sole cause of the discrepancy since all fields should then show equal increase in measured signal outside the field, and the amplification should be greatest farthest outside the field, which is not seen. Lack of lateral electronic equilibrium is a relative local effect and therefore should not cause discrepancy in regions which are not close to the edge of the detector panel, such as just outside the 5 x 5 cm² field; however, missing photon scatter can have farther reaching effects, up to 10 cm, and it is more prevalent for larger fields. The scatter conditions for larger fields may be compromised in the detector model since the imaging panel materials are extended 2.5 cm beyond their lateral physical dimensions but the peripheral electronics present in the physical detector are not modeled. Failure in detector gain correction for low energy scatter is supported by the increase in discrepancy with field size, since the larger the field, the more low energy scatter at the field edge.

Despite discrepancy outside the field, the maximum value of which is 5.0%, the model corresponds well within the central 20 x 20 cm² of the detector, corresponding to the

central $15 \times 15 \text{ cm}^2$ field at 100 cm SSD when the detector is at 130 cm SID. This gives ample coverage of the QC3 contrast phantom region for the setup described in section 3.4.2. If we consider evaluating the impact of the discrepancy on contrast by evaluating contrast between inside and outside the field, the maximum error incurred will be at the edge of the $15 \times 15 \text{ cm}^2$ field and result in calculated contrast 4% greater than measured.

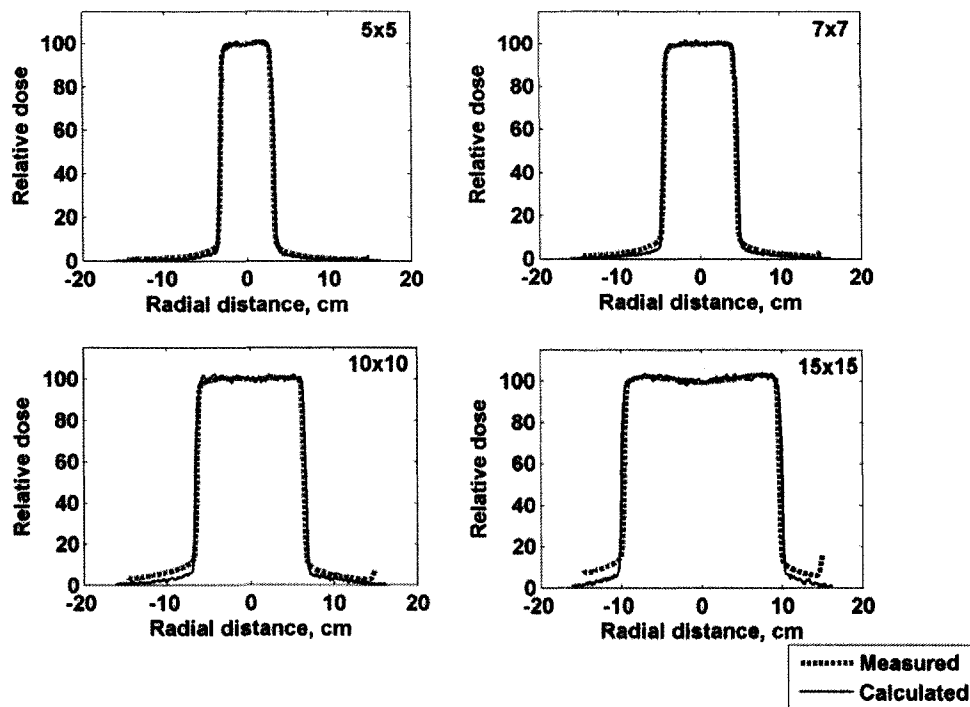


Figure 4.4 Relative dose versus radial distance along the in-plane axis (parallel to the linac waveguide), comparing calculated versus measured profiles for 6 MV images from the aS500 EPID at 130 cm SID for field sizes $5 \times 5 \text{ cm}^2$ to $15 \times 15 \text{ cm}^2$.

When validating the same model, Siebers *et al* (2004) report agreement within 1% for all points; however, both their method of calibration and method of scoring in the detector model were different. The first step of image calibration was identical for both studies, using the modified method for capturing the flood field. Siebers then multiplies by a calibration matrix, which effectively equates the calculated and measured flood fields at the SID of the image – this correction should bring the MC and measured curves closer together by adding modulation present in the measured image to the MC profile before

comparison. Siebers noted disagreement only in the area of the detector where the support arm and associated electronics would have introduced asymmetry in the measured image, a feature that is not present in the symmetric MC model. The rapid increase at approximately +15 cm the measured data in this study is also attributed to increased backscatter from the support arm assembly.

El-Mohri *et al* (1999), using an active matrix flat-panel imager, compared radial profiles from open field images to ion chamber measurements and found a similar over-response outside the field for the detector configuration where a phosphor layer preceded the a-Si diode array. He suggests that the disagreement is due to over-response of the high $-Z$ phosphor screen to the low energy scatter component of radiation in that region, versus the ion chamber whose response is relatively energy independent in comparison. This explanation should not apply to our case, assuming the spectrum incident on the screen and the low energy screen response is modeled accurately. Warkentin *et al* (2003) demonstrate the same effect when comparing raw a-Si EPID images with diamond detector measurements and, attributing it to scatter, use a Monte Carlo-generated kernel for dose deposition in the EPID phosphor and an empirically derived kernel for optical photon spreading, report de-convolving high-resolution primary fluence distributions. Siebers claims the precision in his MC model removes the requirement for dose correction kernels. Individual adjustment of detector pixel gain, removing the requirement for general image calibration, would provide valuable information on the origin of the disagreement, but is not within the scope of this work.

4.4 Quantifying and Validating Contrast

Absolute contrast is reported instead of contrast to noise ratio (CNR) since noise cannot be readily equated between Monte Carlo and measurement.

4.4.1 Simple 6 MV Contrast Evaluation

The simple contrast setup, using the 6 MV beam and the detector at 130 cm SID, resulted in calculated contrast within 1.0% of the measured value for 5 cm Solid water versus open field. This demonstrates that the detector model is capable of accurately reproducing contrast measurements.

4.4.2 Effect of Field Size on Contrast

Using modeling and measurement with the 6 MV therapy beam and the 6 MeV/Al beam, reducing field size was shown to increase absolute contrast. For the 6 MeV/Al beam this is demonstrated in figure 4.5. Measured contrast increased more strongly with field size than the Monte Carlo model, the potential explanations for this are listed below.

The 6 MV calculated contrast agreed within 2.5 - 5% of measured values for all regions of the phantom at all field sizes. The same setup was used with the 6 MeV/Al beam, the resulting calculated contrast was 3% higher than measured for all regions. With reference to the measured images, the patient couch rails and supports used to suspend the QC3 were inside the primary field and would produce scatter that is not modeled in the Monte Carlo calculation. The effect of field size on contrast was examined for both 6 MV and 6 MeV/Al beams. The 6 MV contrast agreement remained within 2.5 - 5% for both 32 x 24 cm² and 10 x 10 cm² field sizes, while for 6 MeV/Al agreement is within 5-10% for the 32 x 24 cm² field, but reduces to within 2.5 - 5% for the 10 x 10 cm² field, figure 4.5. The magnification of the low-Z beam means that for equal set field size, more of the un-modeled support apparatus is inside the primary field with the 6 MeV/Al beam, than at the same jaw setting with 6MV, to produce scatter. Also the lower mean energy of the 6 MeV/Al beam, will produce more low energy scatter having greater mean scattering angle than that of higher energy scatter produced by the 6 MV beam. In standard practice, the beam is collimated to just outside the object, eliminating unwanted scattered radiation and, especially in the case of MV imaging, limiting dose to peripheral structures. Imaging with a full field is not a common scenario.

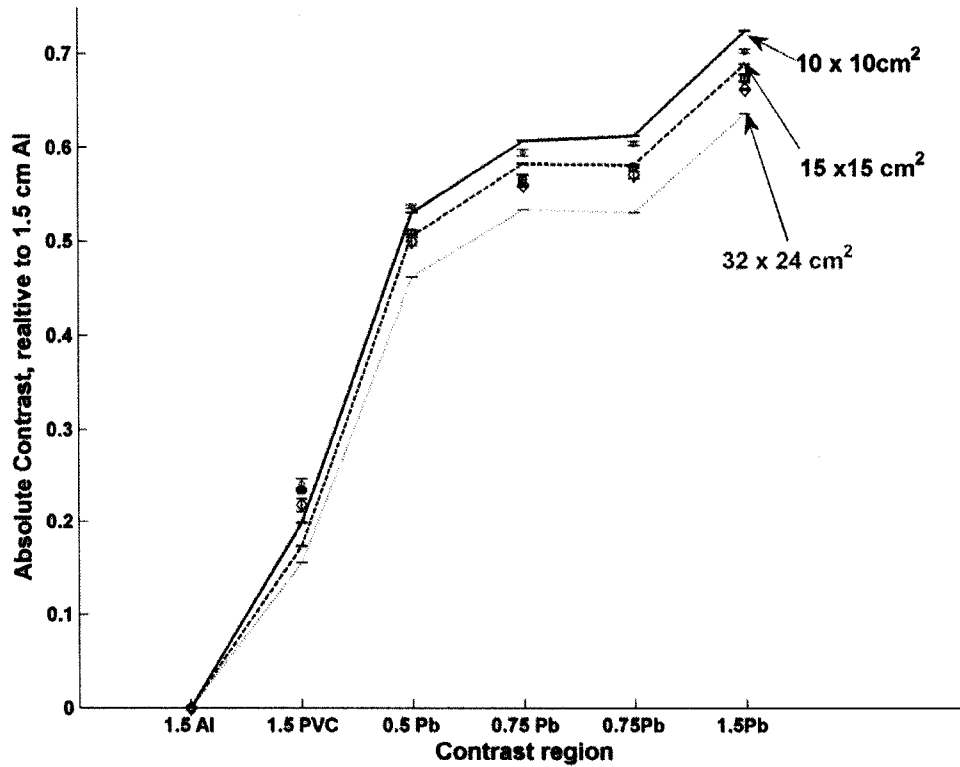


Figure 4.5 Absolute contrast versus contrast region for the QC3 phantom, comparing measured versus calculated results as a function of field size for the 6 MeV/Al beam. Solid lines denote measured contrast and circles, Monte Carlo calculated contrast.

4.4.3 6 MV and 6 MeV/Al Contrast Validation

Figure 4.6 shows absolute contrast from measured and calculated images, for both the standard 6 MV and experimental 6 MeV/Al beams at a 10 x 10 cm² field size, with the detector at 130 cm SID; the conditions under which contrast will be assumed validated. Error bars in QC3 absolute contrast figures show the standard error about the mean pixel value of each sampled region, propagated through the contrast calculation. Absolute contrast values are reported here to avoid a negative contrast value for the 1.5 cm PVC region, which attenuates the beam less than the reference region. Comparison between the measured and calculated values shows that the MC model of the full imaging system predicts contrast accurately, to within 2.5% for most regions, for both 6 MV and 6 MeV/Al.

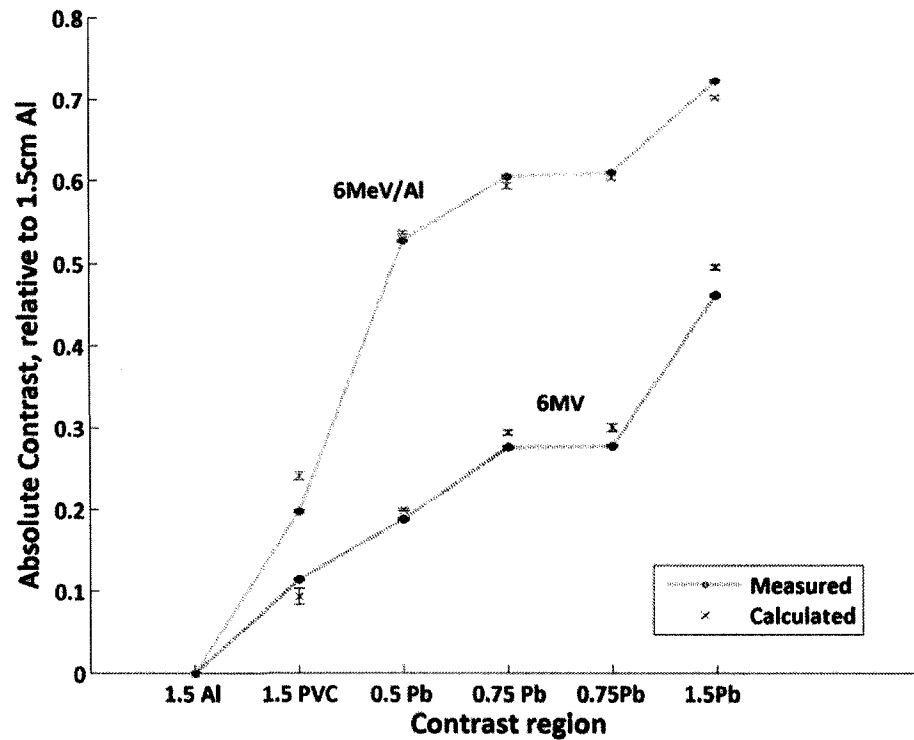


Figure 4.6 Absolute contrast versus contrast region for calculated and measured images with the standard 6 MV beam and 6 MeV/Al beam. Error bars show the standard error about the mean pixel value of each sampled region, propagated through the contrast calculation.

Flampouri *et al* (2002) used an earlier version of the BEAMnrc/ DOSXYZnrc package (EGS4) to model their whole imaging system and reported agreement on the order of 2.5% when modeling 4.75 MeV electrons on a 0.6 cm Al target with bone versus water detected by a simple film-screen mammography system model, with 2-3 MC modeled layers. The complexity of the EPID model used in the present study is much greater than that used by Flampouri, incorporating all 26 layers of detector material present in the physical panel.

Both the calculated and measured results in figure 4.6 demonstrate the advantage of the low-Z, unflattened beams in terms of imaging contrast. By using the 6 MeV/Al beam instead of 6 MV, contrast increases by a factor of 1.57 to 2.81, depending on the phantom region. While Tsechanski *et al.* (1998) only report qualitatively on contrast improvement, noting “improved image sharpness and contrast” using 0.5 cm Al and 1.5 cm Cu targets

with 6 MeV electrons over the standard 6 MV therapy beam, Ostapiak *et al* (1998) see a factor increase of approximately 2 with 6 MeV on 1.4 cm Al versus the standard 6 MV therapy beam also using a 2 g/cm² Al disk on 5 cm of solid water to generate contrast. The above comparisons indicate that the improvement of low-Z over therapy seen here are in the range of previously results with low-Z targets and film-screen detection systems. Larger magnitudes of contrast increase in previous studies may be attributed to screen thickness, which will be discussed further in section 4.6.

4.5 The Effect of Further Image System Alterations on Contrast

Figure 4.7 shows the effect on absolute contrast of alterations to the imaging system parameters, as predicted by the MC model for a 10 x 10 cm² field and 130 cm SID. The 6 MeV/Al curve is shown for reference. By decreasing the incident electron energy to 4 MeV, absolute contrast is increased by a factor as high as 1.21. If the copper layer of the detector is removed, contrast increases by a factor of up to 1.17, for both 6 MeV/Al and 4 MeV/Al. At 4 MeV and 6 MeV, the Be target shows a slight advantage over the Al target for the QC3 phantom used in this study, with either the standard or copper-less detector arrangement. Galbraith (1989) shows that decreasing electron energy increases the diagnostic photon yield below 150 keV at all target thicknesses. Conversely Tsechanski *et al* (1998) show that for a 0.2 cm Cu target *increasing* electron energy increases the photon yield at all energies and preferentially at the lower portion of the spectrum, softening the beam. This group suggests that this is due to photons being produced progressively close to the downstream surface of the target resulting in less attenuation. Our results support Galbraith and indicate that target thickness potentially played a role in the result of Tsechanski *et al*. The increases in contrast produced by the Al and Be targets at 4 MeV can potentially be explained by the beams' spectral distributions. 4 MeV/Be and 4 MeV/Al show increased fractional fluence between 25 keV and 150 keV, relative to the 6 MeV beams (figure 4.1). The results of Ostapiak *et al* (1998) show that for 10 cm of water attenuation, photons below 25 keV are fully attenuated and do not therefore contribute to contrast, only to patient dose.

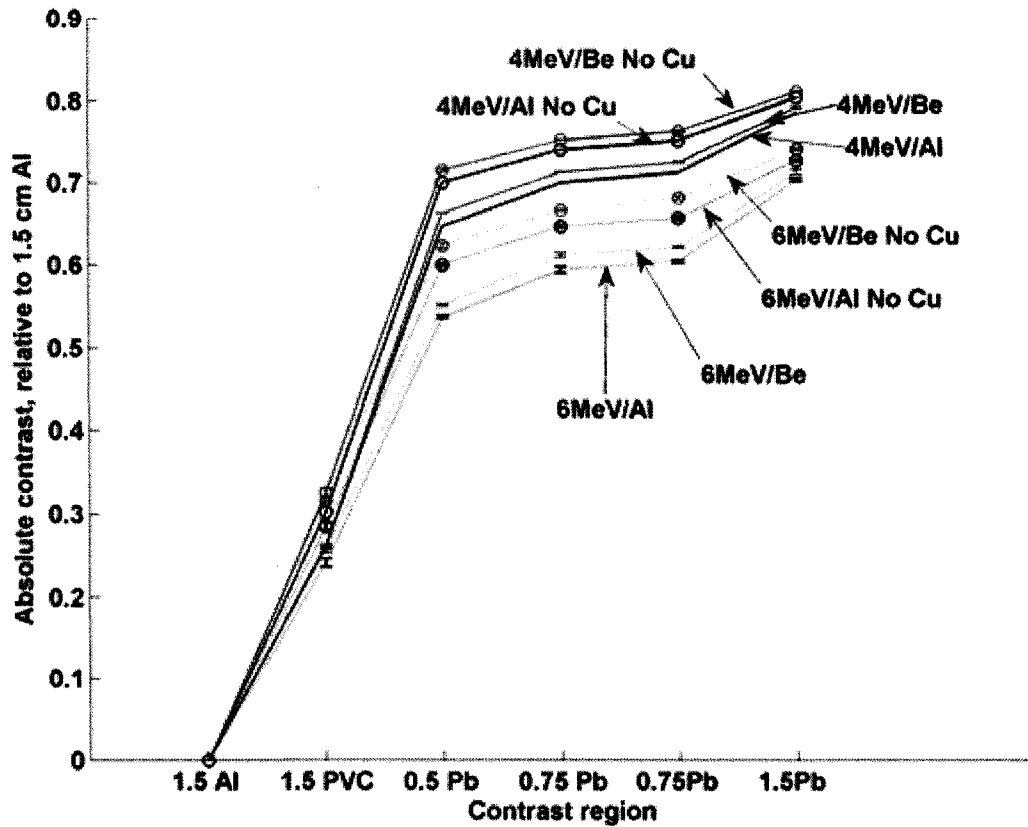


Figure 4.7 Absolute contrast versus contrast region, comparing QC3 calculated contrast on a standard aS500 EPID for 6 MeV and 4 MeV incident electron energies on 1.0 cm and 0.67 cm aluminum (blue) targets, respectively, and 6 MeV and 4 MeV incident electron energies on 1.5 cm and 1.0 cm beryllium (red) targets respectively. Contrast generated on a copper-less imager (No Cu) is shown, (denoted with circles).

4.6 The Effect of Separation on Contrast

The effect of increasing separation on contrast with the standard 6 MV beam and the 6 MeV/Al beam, for the bone/water phantom, is shown in figure 4.8. Contrast was calculated using mean pixel values from symmetric regions-of-interest below each region. At 5 cm separation, the 6 MeV/Al beam yields a contrast = 0.086 while for the therapy beam contrast = 0.036, giving a low-Z contrast advantage factor of approximately 2.4. The contrast drops more rapidly for the 6 MeV/Al beam than the standard 6 MV with increasing separation; however, low-Z contrast remains superior even at 16 cm total separation by a factor of 1.7. For a separation of 16 cm, the 6 MeV/Al contrast is 60 % of that at 5 cm separation while for 6 MV contrast is 83% of that at 5 cm. Galbraith

(1989) and Ostapiak *et al* (1998) show that contrast produced by low-Z beams decreases more quickly than contrast for a therapy beam and that up to head and neck-like separations (15 cm), the contrast advantage of low-Z beams is still present.

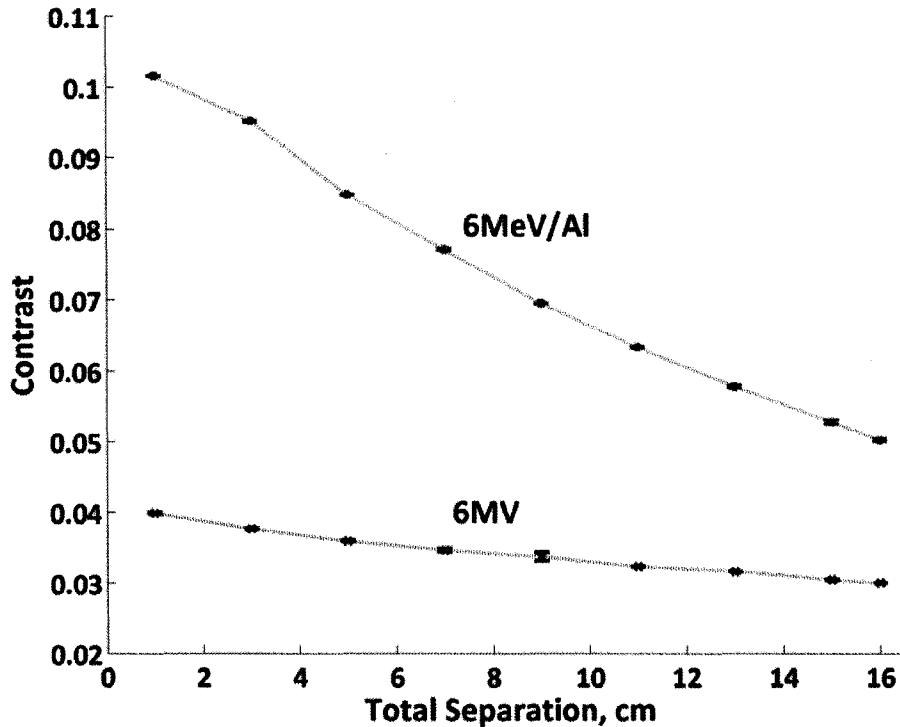


Figure 4.8 Bone to water contrast versus total separation, comparing measured 6 MV and 6 MeV/Al beams.

At 5 cm separation, with 1 cm bone to create contrast, Flampouri *et al* (2002) show that 4.75 MeV electrons on a 6 mm Al target yields a factor increase in contrast over the 6 MV therapy beam of 3.6. If approximately equivalent contrast conditions are taken from figure 4.8, 5 cm separation with 1 cm bone, the factor increase in contrast is 2.4. Using the data from figure 4.7, if this is multiplied by 1.23 to account for the energy difference, and 1.17 for removal of the copper screen, the predicted result is a contrast increase of 3.45, close to that of Flampouri *et al*. Although the factor for decreasing electron energy may be slightly exaggerated (4.5 MeV versus 4.75 MeV); the remaining difference could result from the screen thickness or composition. The screen in the aS500 is Kodak Lanex Fast Back with a thickness of approximately $134 \text{ mg/cm}^2 \text{ Gd}_2\text{O}_2\text{S}:\text{Tb}$ (Siebers, Kim *et al*. 2004), while that of the mammography system is Kodak Lanex Fine, thickness 34 mg/

$\text{cm}^2 \text{Gd}_2\text{O}_2\text{S}$ (Flampouri, Evans et al. 2002). Flampouri *et al* show that decreasing screen thickness increases the selective response to low energy photons.

CHAPTER 5 Conclusion

5.1 Monte Carlo Modeling

The BEAMnrc/EGSnrc package is one of the most used Monte Carlo simulation programs for radiation therapy (Rogers, Walters et al. 2006) and has been used extensively for a wide variety of applications. It has been applied here to develop a realistic model of a full imaging system including the linear accelerator beam, contrast phantom and a-Si detector panel. The detector alone requires 26 material layers with sub-millimeter precision thickness. The model was validated for the standard 6 MV therapy beam and the 6 MeV/Al beam and proved capable of predicting contrast values within 2.5% of measurement for both beams. Although Monte Carlo simulation remains a computationally intensive process, proper selection of efficiency improving techniques can reduce the time required per simulation and simple modifications to the model can predict results that would potentially be both time consuming and expensive to perform physically.

5.2 Contrast in Low-Z-Target MV Imaging: Summary of Results

Lowering the atomic number of the target has been shown previously to shift the resulting photon spectrum to lower energy relative to standard MV therapy beams (Galbraith 1989; Ostapiak, O'Brien et al. 1998; Tsechanski, Bielajew et al. 1998). The energy range useful for radiation therapy imaging was predicted from previous work (Galbraith 1989; Ostapiak, O'Brien et al. 1998) and it was found in this work that at least one third of the fractional fluence for the 6 MeV/Al beam exists in this range. This indicates that lower dose per image should be achievable with low-Z-target beams and increased contrast should also result. The 6 MeV/Al beam was shown to produce a factor increase in contrast over the standard 6 MV beam between 1.57 and 2.81, a significant increase. Using the Monte Carlo model, contrast improvement due to decreasing electron energy from 6 MeV to 4 MeV and removing the Cu layer of the detector was found to further increase contrast by factors of up to 1.21 and 1.17, respectively, relative to 6

MeV/Al. At 4 MeV further decreasing target Z to beryllium did not improve contrast, for the phantom used. Through experimental measurement, the contrast advantage of 6 MeV/Al over 6 MV was shown to decrease with increasing separation, but remain as a 1.7 factor advantage at 16 cm of Solid Water separation. All of the above results are quantified for two dimensional projection images.

5.3 Future Work: Further Optimizations

5.3.1 Screen thickness

Previous studies indicate that the ratio of dose deposited by low energy versus high energy photons decreases with screen thickness; however, decreasing screen thickness also reduces detection efficiency (Flampouri, Evans et al. 2002). Achieving a balance between the two will be important in optimal detector design for the low-Z spectrum.

5.3.2 Target Location

The target location had been improved from previous work (Robar 2006) but, due to practical limitations of experimenting with a clinical linac, is currently still in air, downstream of the Be exit window. Electron beam spreading in air increases focal spot size, indicated here as increased spread in radial electron fluence at the previous and current target surface locations. The optimal position of the target is likely in vacuum and the effect of target location on spatial resolution in low-Z imaging remains to be investigated.

5.3.3 Necessary Level of Contrast

The aim of MV imaging in IGRT and DGRT is patient alignment and anatomical tracking. Ideally, co-registration of two- or three-dimensional MV and planning image sets will allow these aims to be achieved in an accurate, objective and reproducible manner. The contrast necessary to perform this task is then the level that is required for MV imaging. Morin *et al* (Morin, Gillis et al. 2006) report the ability to co-register MV CBCT and planning images, using a standard therapy beam; however, this claim is not widely supported as MV imaging still has a reputation for insufficient contrast (Walter, Boda-Heggemann et al. 2007).

5.3.4 Imaging Dose

Quantifying the dose per image is important in determining the clinical feasibility of the imaging method, but the lower average energy of low-Z target beams suggests they should require less dose per image than standard MV imaging.

5.3.5 Cone Beam CT

MV CBCT has several advantages over kV CBCT that are not significant in two dimensional projection imaging (Morin, Gillis et al. 2006). Our group has already produced a bench-top system for quantifying contrast in low-Z MV CBCT and initial results are promising.

5.4 Application

The changes required to introduce low-Z imaging into a standard radiation therapy would be addition of a low-Z target ideally in the accelerator target arm and a corresponding ‘imaging’ mode, and, if desired, replacement of the MV-optimized a-Si detector with a copper-less panel. Most major vendors already have developed reconstruction software for either kV or MV CBCT, which could be adapted to the new spectrum to allow integration of low-Z MV CBCT. In summary, incorporation of low-Z targets appears to be a simple and cost effective method for improving integrated MV imaging at the treatment unit with the potential to both increase image contrast and decrease dose relative to current MV imaging practices.

Bibliography

- Almond, P. R., P. J. Biggs, et al. (1999). "AAPM's TG-51 protocol for clinical reference dosimetry of high-energy photon and electron beams." Med Phys **26**(9): 1847-70.
- Attix, F. H. (2004). Introduction to Radiological Physics and Radiation Dosimetry. Weinheim, Germany, Wiley-VCH.
- Aubin, M., O. Morin, et al. (2006). "The use of megavoltage cone-beam CT to complement CT for target definition in pelvic radiotherapy in the presence of hip replacement." Br J Radiol **79**(947): 918-21.
- Bielajew, A. F., H. Hirayama, et al. (1994). History, overview and recent improvements of EGS4 Ottawa, Canada, National Research Council of Canada.
- Emsley, J. (1995). The Elements, Oxford Chemistry Guides. New York, NY, USA, Oxford Univ. Press.
- Flampouri, S., P. M. Evans, et al. (2002). "Optimization of accelerator target and detector for portal imaging using Monte Carlo simulation and experiment." Phys Med Biol **47**(18): 3331-49.
- Galbraith, D. M. (1989). "Low-energy imaging with high-energy bremsstrahlung beams." Med Phys **16**(5): 734-46.
- Hall, E. J. and A. J. Giaccia (2006). Radiobiology for the radiologist. Philadelphia, PA, USA, Lippincott Williams and Wilkins.
- Jaeger, A. (2005). "LFS in Linux." http://www.suse.de/~aj/linux_lfs.html Last modified: Feb 15 2005 Retrieved 05/08/08, 2008.
- Johns, H. E. and J. R. Cunningham (1983). The Physics of Radiology. Springfield, Illinois, USA, Charles C Thomas.
- Karzmark, C. J., C. S. Nunan, et al. (1993). Medical Electron Accelerators. New York, USA, McGraw-Hill Inc.
- Keall, P. J., J. V. Siebers, et al. (2003). "Determining the incident electron fluence for Monte Carlo-based photon treatment planning using a standard measured data set." Med Phys **30**(4): 574-82.
- Khan, F. M. (2003). The Physics Of Radiation Therapy, Lippincott Williams & Wilkins.
- Ling, C. C., S. Leibel, et al. (2003). A practical guide to intensity-modulated radiation therapy. Madison, WI, USA, Medical Physics Publishing.

- Low, D. A. and J. F. Dempsey (2003). "Evaluation of the gamma dose distribution comparison method." Med Phys **30**(9): 2455-64.
- Mah, D. W., D. M. Galbraith, et al. (1993). "Low-energy imaging with high-energy bremsstrahlung beams: analysis and scatter reduction." Med Phys **20**(3): 653-65.
- Marrett, L., D. Dryer, et al. (2008). Canadian Cancer Statistics 2008. Toronto, Canada, Canadian Cancer Society/National Cancer Institute of Canada.
- Morin, O., A. Gillis, et al. (2006). "Megavoltage cone-beam CT: system description and clinical applications." Med Dosim **31**(1): 51-61.
- Munro, P. and D. C. Bouius (1998). "X-ray quantum limited portal imaging using amorphous silicon flat-panel arrays." Med Phys **25**(5): 689-702.
- Ostapiak, O. Z., P. F. O'Brien, et al. (1998). "Megavoltage imaging with low Z targets: implementation and characterization of an investigational system." Med Phys **25**(10): 1910-8.
- Pouliot, J., A. Bani-Hashemi, et al. (2005). "Low-dose megavoltage cone-beam CT for radiation therapy." Int J Radiat Oncol Biol Phys **61**(2): 552-60.
- Rajapakshe, R., T. J. Radcliffe, et al. (1993). Quality control for on-line portal imaging systems. Proc. SPIE.
- Robar, J. L. (2006). "Generation and modeling of megavoltage photon beams for contrast-enhanced radiation therapy." Phys. Med. Biol. **51**: 5487-5504.
- Rogers, D. W. (2006). "Fifty years of Monte Carlo simulations for medical physics." Phys Med Biol **51**(13): R287-301.
- Rogers, D. W., B. A. Faddegon, et al. (1995). "BEAM: a Monte Carlo code to simulate radiotherapy treatment units." Med Phys **22**(5): 503-24.
- Rogers, D. W., B. R. Walters, et al. (2006). BEAMnrc Users Manual. Ottawa, Canada, NRCC: 84-85.
- Saint-Jacques, N., R. Dewar, et al. (2006). Understanding Cancer in Nova Scotia:2000-2004. S. a. E. Unit. Halifax, NS, Canada Cancer Care Nova Scotia.
- Sempau, J., A. Sanchez-Reyes, et al. (2001). "Monte Carlo simulation of electron beams from an accelerator head using PENELOPE." Phys Med Biol **46**(4): 1163-86.
- Siebers, J. V., J. O. Kim, et al. (2004). "Monte Carlo computation of dosimetric amorphous silicon electronic portal images." Med Phys **31**(7): 2135-46.
- Tsechanski A, B. A. F., Faermann S and Krutmann Y (1998). "A thin target approach for portal imaging in medical accelerators." Phys. Med. Biol. **43**: 2221-36.

- Tsechanski, A., A. F. Bielajew, et al. (1998). "A thin target approach for portal imaging in medical accelerators." Phys Med Biol **43**(8): 2221-36.
- Tsechanski, A., Y. Krutman, et al. (2005). "On the existence of low-energy photons (<150 keV) in the unflattened x-ray beam from an ordinary radiotherapeutic target in a medical linear accelerator." Phys Med Biol **50**(23): 5629-39.
- Walter, C., J. Boda-Heggemann, et al. (2007). "Phantom and in-vivo measurements of dose exposure by image-guided radiotherapy (IGRT): MV portal images vs. kV portal images vs. cone-beam CT." Radiother Oncol **85**(3): 418-23.
- Walters, B., I. Kawrakow, et al. (2006). DOSXYZnrc Users Manual. Ottawa, Canada, NRCC.
- Walters, B. R., I. Kawrakow, et al. (2002). "History by history statistical estimators in the BEAM code system." Med Phys **29**(12): 2745-52.

Appendix A Component Modules for Linac Modeling

Spec module files for the 6 MV beam, steps one and two, and the low-Z beams (6 MeV/Al) specifying the component modules used to model the linac. These files are found in the `egsnrc_mp->beam ->spec modules` folder.

6 MV, step 1:

Top6MV.module

```
CM names:  FLATFILT FLATFILT SLABS MIRROR
Identifiers:  targpri flatfilt chamber mirror
```

6 MV, step 2:

6MV10x10.module

```
CM names:  JAWS SLABS
Identifiers:  jaws mylar
```

Low-Z beams (6 MeV/Al):

Top6eAlH.module

```
CM names:  FLATFILT FLATFILT SLABS MIRROR JAWS SLABS
Identifiers:  pricol lowztarg chamber mirror jaws mylarsty
```

Appendix B MATLAB Code for Reading and Adding 3ddose Files

MATLAB code to read in 3ddose files (read33dose.m) and add them (add3ddose.m).

read33dose.m

```
%
% read3ddose.m
%
% 18/10/07
%
% EJOrton
%
% last modified: 04/02/08
%
% This function reads in a DOSXYZnrc .3ddose file producing:
% 3 scalars: nx,ny,nz - the number of data points in dimension (not
OUTPUT)
% 3 vectors: x,y,z - the coordinates of the profile axes, output as the
% coordinate of the voxel mid-point.
% 2 3D matrices: datmat and errmat - the data matrix and corresponding
% 'relative' error matrix. errmat may be multiplied, point by point,
% with datmat to get the absolute error by activating line 79.
% Absolute error, as calculated from a .3ddose file, is the standard
% deviation as scored by the history-by-history method for DOSXYZnrc
% generated files, (Walters et al. Med. Phys. 29 (12) Dec. 2002)
%
% INPUTS:
% file = filename, excluding .3ddose extension, [including 'fileloc/']

function[x,y,z,datmat,errmat] = read3ddose(file)

debug = 0;
if debug ==1;
    file = 'Insert filename here';
    % Insert a filename, with .3ddose extension, that exists in the
same
    % folder as read3ddose.m
else
    file = ([file '.3ddose']);
end

fid = fopen(file, 'r');

nx = fscanf(fid,'%d', 1);
ny = fscanf(fid,'%d', 1);
nz = fscanf(fid,'%d', 1);

%filling in an x coordinate vector
coordmat = fscanf(fid,'%f', nx+1);
x = zeros(1,nx);
for i = 1:nx
    x(i) = ((coordmat(i+1))-(coordmat(i)))/2+coordmat(i);
end
```

```

%filling in y coordinate vector
coordmat = fscanf(fid,'%f', ny+1);
y = zeros(1,ny);
for i = 1:ny
    y(i) = ((coordmat(i+1))-(coordmat(i)))/2+coordmat(i);
end

%filling in z coordinate vector
coordmat = fscanf(fid,'%f', nz+1);
z = zeros(1,nz);
for i = 1:nz
    z(i) = ((coordmat(i+1))-(coordmat(i)))/2+coordmat(i);
end

%now for data and error matrices

datmat = zeros(nx,ny,nz);
errmat = zeros(nx,ny,nz);
%make 2 zero matrices

for zi = 1:nz
    for yi = 1:ny
        for xi = 1:nx
            datmat(xi,yi,zi) = fscanf(fid,'%f',1);
        end
    end
end
% filling in the data matrix

for zi = 1:nz
    for yi = 1:ny
        for xi = 1:nx
            errmat(xi,yi,zi) = fscanf(fid,'%f',1);
            % this is the relative error matrix
            %errmat(xi,yi,zi) = errmat(xi,yi,zi).*/datmat(xi,yi,zi);
            % this is the absolute error matrix.
        end
    end
end
% filling in the error matrix

add3ddose.m

%
% add3ddose.m
%
% 18/10/07
%
% EJOrton
%
% last modified: 05/02/08
%
% This function adds the files listed, and assumes they have equal
% partitioning (i.e. equal voxel sizes, distributions and locations).

```

```

% Dose values and error are summed for each location.
% Activate lines 37 & 39 if you want averaged dose and error instead.
% Filenames should follow 'fileloc/filename_#.3ddose', where # is the
filenumber
% Files should be numbered sequentially between firstfile and lastfile

% INPUTS: fileloc = file location of .3ddose file
%          filename = filename
%          firstfile = number of first file to be added
%          lastfile = number of last file to be added

function[data3D,error3D,xvect,yvect,zvect] =
add3ddose(fileloc,filename,firstfile,lastfile)

Cfile = ([fileloc filename '_' num2str(firstfile)]);
[xvect,yvect,zvect,totdatmat,toterrmat] = read3ddose(Cfile);
filenum = lastfile - firstfile +1;

if lastfile>firstfile
    for f = firstfile+1:lastfile
        b = (['_' num2str(f)]);
        Cfile = ([fileloc filename b]);
        [xvect,yvect,zvect,datmatf,errmatf] = read3ddose(Cfile);
        totdatmat = totdatmat+datmatf;
        toterrmat = sqrt(toterrmat.^2+errmatf.^2);
    end
    totdatmat = totdatmat/filenum;
    %averaging the total dose in totdatmat
    toterrmat = toterrmat/filenum;
end
data3D = totdatmat;
error3D = toterrmat;

```

Appendix C PVC PEGS Input File

The input file used to generate cross section data for the PVC regions of the QC3 phantom, using peps.exe. This file can be found in the egsnrc_mp->pegs4 ->inputs folder.

PVC700.pegs4inp

```
>COMP
> &INP NE=3,RHO=1.30,PZ(1)=2,PZ(2)=3,PZ(3)=1 &END
>PVC700
>C H CL
>ENER
> &INP AE=0.7,UE=30.511,AP=0.01,UP=30. &END
>PWLF
> &INP &END
>DECK
> &INP &END
```

PVC is a compound - COMP

The density of PVC is $\text{RHO}=1.30$

The atomic composition of PVC is $\text{C}_2\text{H}_3\text{CL}$:

PZ(i) is the number of atoms of element i in line 4

The name for the output peps4.dat file is PVC700 (line 3)

Line 5 gives the energy range within which the cross sections will be computed.